

Doctoral Thesis

Periodic semiconductor nano-structures for the
enhanced photovoltaic devices

Hyo-Jin Ahn

School of Energy and Chemical Engineering

Graduate School of UNIST

2015

Periodic semiconductor nano-structures for the enhanced photovoltaic devices

Hyo-Jin Ahn

School of Energy and Chemical Engineering

Graduate School of UNIST

Periodic semiconductor nano-structures for the enhanced photovoltaic devices

A dissertation
submitted to the Graduate School of UNIST
in partial fulfillment of the requirements for
the degree of
Doctor of Philosophy

Hyo-Jin Ahn

6. 17. 2015

Approved by



Advisor

Ji-Hyun Jang

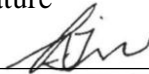
Periodic semiconductor nano-structures for the enhanced photovoltaic devices

Hyo-Jin Ahn

This certifies that the dissertation of Hyo-Jin Ahn is approved.

06/17/2015

Signature



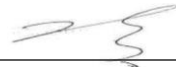
Advisor: Ji-Hyun Jang

signature



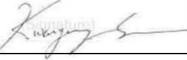
Hyunhyub Ko

Signature



Tae-Hyuk Kwon

signature



Kwanyong Seo

signature



Jong Hyeok Park

Abstract

Periodic semiconductor nano-structures for the enhanced photovoltaic devices

by

Hyo-Jin Ahn

Doctor of Philosophy in Department of Energy/Chemical engineering

Ulsan National Institute of Science and Technology

Professor Ji-Hyun Jang

The photovoltaic devices which convert the solar energy to the electrons or chemical materials become very important clean energy devices due to the environmental pollution from the fossil energy. The Dye-sensitized Solar cell (DSSC) which generates the electron-hole pairs using solar light and photoelectrochemical cell (PEC), one of the promising clean energy solar cells for capturing and storing solar energy by splitting water into a hydrogen and oxygen gas have received extensive attention because of high performance and low price. Enhancing optical property is the one of the fascinate strategy for the increasing the properties of photovoltaic devices.

Interference lithography (IL) is a very convenient and fast method to fabricate the two/three-dimensional polymer template in a submicrometer scale. By combining an IL technique and hydrothermal growth, the high crystalline periodic semiconductor nanowires such as ZnO, TiO₂ and Fe₂O₃ can be fabricated. The 2D patterned semiconductor nanowires can be considered as a diffraction grating layer which can enhance the optical property for increasing the overall performance of photovoltaic devices such as DSSC and PEC.

In this thesis, I studied on the synergetic effects of the IL technique and the hydrothermal growth method for enhancing the optical properties. The patterned nanowires with a subwavelength scale that act as the diffraction grating layer can increase the optical path in the photovoltaic devices. Especially, the absorption of visible wavelength of solar light (400nm ~ 800nm), a major source to generate the electron-hole pairs in the photovoltaic cells can be enhanced by the pattern nanowires. The outstanding properties of the 2D patterned nanowires suggest the great potential in energy-related devices such as DSSCs, PEC cells and sensor devices such as SERS.

Contents

Abstract	1
Contents	2
List of Figures	4
List of Table	10
Chapter 1. Introduction of Periodic Nano-structure for Photovoltaic Device.....	11
1.1 Mie scattering	12
1.2 Photonic crystal.....	13
1.3 Interference Lithography.....	13
1.4 Hydrothermal growth.....	14
1.5 Dye-sensitized solar cell (DSSC).....	14
1.6 Photoelectrochemical cell (PEC)	15
REFERENCES	21
Chapter 2. Power Conversion Efficiency Enhancement Based on the Bio-inspired Hierarchical Antireflection Layer in Dye Sensitized Solar Cell.....	23
1. Introduction.....	23
2. Experimental and characterization.....	25
2.1 Fabrication of 2-dimensional Diffraction Grating layer in Polymer template	25
2.2 Fabrication of DSSC with the photoanode coupled with the hierarchical AR layer.....	25
2.3 Characterization	25
3. Results and Discussion.....	26
4. Conclusion.....	39
5. REFERENCES	40
Chapter 3. Hierarchical Metal/Semiconductor Nanostructure for Efficient Water Splitting	43
1. Introduction.....	43
2. Experimental Procedures	44
2.1 Chemicals used	44
2.2 Fabrication of 2D patterns via interference lithography	44
2.3 ZnO NWs growth via hydrothermal method	44
2.4 Characterization	45
2.5 EF calculations	45
2.6 Photo electrochemical (PEC) Measurement	45
3. Results and Discussion.....	47
4. Conclusion	56

5. REFERENCES	58
Chapter 4. An optimal substrate design for SERS: dual-scale diamond-shaped gold nano-structures fabricated via interference lithography	61
1. Indroduction.....	61
2. Experimental	64
3. Results and Discussion.....	65
4. Conclusion	76
5. REFERENCES	77
Chapter 5. MoS _x /Ti-doped α -Fe ₂ O ₃ Heterojunctions for Enhanced Photoelectrochemical Performance	81
1. Introduction.....	81
2. Experimental section.....	82
2.1 Preparation of Ti-Fe ₂ O ₃ and MoS _x /Ti-Fe ₂ O ₃	82
2.2 Photoelectrochemical measurement	82
3. Results and Discussion.....	85
4. Conclusion	95
5. References.....	96
Chapter 6. Optimization of Quantum Dot-Sensitized Photoelectrode for Realization of visible Light Hydrogen Generation.....	100
1. Introduction.....	100
2. Experimental Procedure.....	101
2.1 Chemicals used	101
2.2 Characterization	101
2.3 Fabrication of p-TiO ₂ NWs and p-PDMS	101
2.4 Fabrication of the lh-P25 electrode.....	102
2.5 Fabrication of CdSe/lh-P25.....	102
2.6 Calculation of effective refractive index of antireflection (AR) layer	102
2.7 Photoelectrochemical (PEC) Measurement	102
2.8 Efficiency calculations	103
3. Result and Discussion	103
4. Conclusion	122
5. REFERENCES	123
Acknowledgement	125

List of Figures

[Chapter 1]

Figure 1. Mechanism of the hydrothermal growth

Figure 2. The mechanism of the interference lithography.

Figure 3. The mechanism of the Dye-sensitized Solar cell.

Figure 4. The energy level diagram of the semiconductors.

Figure 5. The mechanism of photocatalytic water splitting for n-type semiconductor.

[Chapter 2]

Figure 1. Schematic illustration for the fabrication of TiO₂ nanocrystalline electrode with moth-eye motivated anti-reflection layer in DSSC device (a) and SEM images of the TiO₂ nanowires (b, c): (b) The hybrid hierarchically patterned TiO₂ antireflection layer (IV). Inset image shows a cross-sectional image of dual-scale TiO₂ nanowires. (c) Cross-sectional image of the working electrode (V) consisted of a layer of NC-TiO₂ and an underlying patterned anti-reflection layer in TiO₂.

Figure 2: SEM images of a) SU-8 polymer template pattern b) periodic TiO₂ nanowires grown on FTO glass

Figure 3. SEM images of a) TiO₂ nanowires; b) Cross-sectional view image of TiO₂ nanowires

Figure 4. Confirmation of prepared TiO₂ hybrid sample: (a) XRD patterns of TiO₂ nanostructures. (b) HRTEM image of TiO₂ nanostructures.

Figure 5. (a) Reflectivity spectrum measured, within the visible light wavelength range, on the pure TiO₂-NC structure and hybrid structure with an additional AR layer of TiO₂ nanostructure (P-NWs+NC). (b) Diffuse reflectance spectra and (c) UV-vis absorption spectra of the pure TiO₂-NC structure, pure

patterned TiO₂ NWs structure, and hybrid structure composed of pure P25 NC and an additional AR layer of patterned TiO₂ NWs. All the measurements were taken without dye or electrolyte.

Figure 6. The reflectivity of 600 nm TiO₂ NWs

Figure 7. Absorbance spectra of TiO₂ NWs after N-719 dye absorption: a) 5.5 μm hybrid structure; b) 500 nm TiO₂ NWs; c) 5 μm NC-TiO₂ structure

Figure 8. The photo-to-electron conversion efficiency of devices fabricated with and without the TiO₂ scattering and AR layer: (a) The incident photon-to-current collection efficiency (IPCE) spectra. (b) Current-voltage (I-V) curves for DSSCs using the hybrid structure (P-NWs+NC) and P25 NC. A schematic illustration of a DSSC with the hybrid type photoanode is inserted.

[Chapter 3]

Figure 1. Schemes shows the fabrication process of the surface deposited hierarchical SERS substrate. (I) Double exposure through interference lithography (IL). The blue arrows display the direction of the laser beams. (II) IL template synthesized on the ZnO seed layer. (III) ZnO NWs grown in the circular holes of the 2-D square lattice. (IV) Hierarchical Au NPs coated ZnO NWs (Au NPs/ZnO NWs) in SU-8 templates. (V) Hierarchical Au NPs/ZnO NWs.

Figure 2. SEM, TEM and XRD of ZnO NWs and Au NPs/ZnO NWs: (a) SEM images of ZnO NWs growth on FTO glass and (b) Top-view SEM of Au NPs/ZnO NWs. The insets in (a) and (b) are cross sectional images of the ZnO NWs and a macro image of the Au NPs/ZnO NWs, respectively. (c) TEM image of the gold coated ZnO NWs. The inset is the closed-up image of the Au NP/ZnO NW. (d) XRD of ZnO NWs before (lower) and after (upper) Au deposition. The inset is a magnified image of rectangular area of the Au NPs/ZnO NWs.

Figure 3. SEM images of (a) Su-8 polymer template, (b) Su-8/ZnO NW substrate, (c) patterned ZnO NW and (d) hp Au/ZnO nanostructures.

Figure 4. (a) Absorbance of the P-Au/ZnO NW, P-ZnO NW, Au/ZnONW and ZnO. (b) Raman data of the P-Au/ZnO NW and Au/ZnO NW with crystal violet.

Figure 5. (a) I-V curve of the hp-Au NPs/ZnO NWs, Au/ZnO ZnONw and ZnO with optical filter. (b)

I-V curve of hp-Au NPs/ZnO NWs after 30cycles working. (c) I-V curves under both UV and visible illumination. (d) I-t curves of the samples with light-chopping conditions. The insets in a and c are illustrations showing the PEC mechanism of the ZnO NWs photoanodes.

[Chapter 4]

Figure. 1 Schemes for the fabrication procedures of d-DGNs. (I) Interference Lithography technique for fabrication periodic polymer template. (II) O₂ plasma etching of circular SU-8 for making diamond shape. (III) R.IE etching for DGN shape of gold. (IV) Removal of the SU-8 polymer template (V) gold deposition on the DGN.

Figure. 2 SEM images of (a) a square pattern of air cylinders in a SU-8 film after baking and development of the double exposure IL pattern. (b) Sharply pointed diamond shaped posts of SU-8 fabricated via oxygen plasma etching of the photoresist on the gold substrate. (c) 350 nm DGN with 200 nm spacing between edges after metal RIE of the gold film and removal of the remaining SU-8. (d) A dual-scale 350 nm d-DGN after deposition of gold nanoparticles. The inset is a close-up image of the rectangular area showing gold nanoparticle separation. Note that the preferential accumulation of gold nanoparticles is apparent along the edges/tips of the nanoposts.

Figure 3. TEM image of as-prepared Au nanoparticles.

Figure 4. SEM images of low magnification mode: a) 350nm sized SU-8 polymer template with sharp-edges. b) 200nm sized DGN gap between end of edges. c) DGN with Au NPs.

Figure. 5 Reflection spectrums of a pristine Au film, 350 nm of DGN and 500 nm of DGN substrates with a height of 300 nm on the cleaned silicon substrate. The direct camera image of each sample with the size of 1 cm x 1 cm, representing the reflectivity spectra in the visible range, appears at the right.

Figure. 6 SERS spectrum of DGNs with size of 350 nm and 3 different densities of Au NPs by 629.5 nm Raman laser with a power of 0.1mW. (a) The SERS spectrum of DGN-29 vs. pristine Au nanoparticles substrate. (b) The SERS spectrum of DGN-29, d-DGN-44, and d-DGN-78. The SEM images of (c) pristine gold NP, (d) DGN-29, d-DGN-44, and (e) d-DGN-78 substrates. The inset images in the each SEM image are normalized light intensity ($|E|^2$) distribution of electric field distribution of the each morphology on the top view via the height of the 300nm diamondal gold array

Figure 7. Simulated Electric field distribution of (a) circular shape and (b) diamondal shape of gold structure with the 350nm diameter and 500nm periodicity.

Figure. 8 (a) SERS spectrum of DGN taken at 632.5 nm laser excitation with a power of 0.1 mW; (b–d) SEM images of SERS substrates: Au NPs on flat Silicon substrate (b); d-DGN with the diamondal dimension of 350 nm arrays (c); and d-DGN with the diamondal dimension of 500 nm posts (d). The corresponding calculated electric field enhancements are given. The power of the lasers are normalized to the same scale for comparison. The highest plasmonic behavior of the structure in (c) is observed.

[Chapter 5]

Figure 1. Scheme for fabrication of a $\text{MoS}_x/\text{Ti-Fe}_2\text{O}_3$ photoanode for the PEC cell. (I) Hydrothermal growth of FeOOH with TiCl_3 . (II) Annealing of Ti doped FeOOH at 800°C for 20 min in the furnace. (III) Drop-casting of $(\text{NH}_4)_2\text{MoS}_4$ on $\text{Ti-Fe}_2\text{O}_3$. (IV) Annealing of $\text{Ti-Fe}_2\text{O}_3/(\text{NH}_4)_2\text{MoS}_4$ at 700°C for 1 h with sulfur powder sitting aside in the CVD chamber under an Ar gas condition.

Figure 2. TEM images of (a) Ti-doped hematite ($\text{Ti-Fe}_2\text{O}_3$), (b) 10- $\text{MoS}_x/\text{Ti-Fe}_2\text{O}_3$, (c) 100- $\text{MoS}_x/\text{Ti-Fe}_2\text{O}_3$ and (d) 1000- $\text{MoS}_x/\text{Ti-Fe}_2\text{O}_3$. The thickness of the MoS_x layer was controlled by changing the concentration of the $(\text{NH}_4)_2\text{MoS}_4$ solution from 10 $\mu\text{wt}\%$ to 1000 $\mu\text{wt}\%$.

Figure 3. X-Ray photoelectron spectroscopy scans for (a) Mo and (b) S binding energies of amorphous MoS_x .

Figure 4. (a) UV/Vis absorbance of $\text{Ti-Fe}_2\text{O}_3$ and 10- $\text{MoS}_x/\text{Ti-Fe}_2\text{O}_3$. The inset in the Tauc plot $(\alpha h\nu)^2$ as a function of photon energy presents the optical bandgap (E_g) of 2.1 eV and 2.07 eV for $\text{Ti-Fe}_2\text{O}_3$ and $\text{MoS}_x/\text{Ti-Fe}_2\text{O}_3$, respectively. (b) Schematic illustration of band energies and charge transfer process at the p-n junction of $\text{MoS}_x/\text{Ti-Fe}_2\text{O}_3$. (c) The PL spectra of $\text{Ti-Fe}_2\text{O}_3$ and 10- $\text{MoS}_x/\text{Ti-Fe}_2\text{O}_3$. (d) The photodegradation of methylene blue by $\text{Ti-Fe}_2\text{O}_3$ and 10- $\text{MoS}_x/\text{Ti-Fe}_2\text{O}_3$ at $1.5V_{\text{RHE}}$.

Figure 5. (a) I-V curve of $\text{Ti-Fe}_2\text{O}_3$, 10- $\text{MoS}_x/\text{Ti-Fe}_2\text{O}_3$, 100- $\text{MoS}_x/\text{Ti-Fe}_2\text{O}_3$ and 1000- $\text{MoS}_x/\text{Ti-Fe}_2\text{O}_3$, respectively. (b) Nyquist plots measured under illumination of $\text{Ti-Fe}_2\text{O}_3$, 10- $\text{MoS}_x/\text{Ti-Fe}_2\text{O}_3$, 100- $\text{MoS}_x/\text{Ti-Fe}_2\text{O}_3$ and 1000- $\text{MoS}_x/\text{Ti-Fe}_2\text{O}_3$ measured at 1.50 V vs REH. The inset is an equivalent circuit model for fitting the experimental data. (c) IPCE curve of $\text{Ti-Fe}_2\text{O}_3$ and 10- $\text{MoS}_x/\text{Ti-Fe}_2\text{O}_3$. (d) Dark current of $\text{Ti-Fe}_2\text{O}_3$ and $\text{MoS}_x/\text{Ti-Fe}_2\text{O}_3$ by the O_2 reduction reaction with O_2 bubbling in 1M NaOH.

Figure 6. (a) I-V curve of Ti-Fe₂O₃, 10-MoS_x/Ti-Fe₂O₃, Co-Pi/10-MoS_x/Ti-Fe₂O₃, respectively. (b) I-t curve of Co-Pi/10-MoS_x/Ti-Fe₂O₃.

[Chapter 6]

Figure 1. a) Scheme of the fabrication procedures of lh-P25. A SEM image of lh-P25. b) Top view SEM image of patterned TiO₂-NWs (the bottom layer of lh-P25). The inset shows a TEM image of the rutile phase TiO₂ NWs with the lattice constant of 0.326 nm. c) Top view SEM image of the patterned nanocrystalline TiO₂ layer for anti-reflection (the top layer of lh-P25). The inset shows a TEM image of the anatase phase TiO₂ nanoparticles with the lattice constant of 0.352 nm.

Figure 2. SEM image of bottom layer (a, p-TiO₂ NWs), top layer of antireflection layer (b, p-P25) of lh-P25.

Figure 3. BET of lh-P25 (a) and P25 (b). The inset is pore-size distribution. The surface area are summarized in the table.

Figure 4. X-ray diffraction (XRD) patterns of as-prepared TiO₂ NWs and p-P25.

Figure 5. Optical features of P25 and lh-P25 (p-P25/p-NWs). (a) Reflectivity, (b) Diffuse reflectivity, and (c) UV-visible spectrum of P25 and lh-P25 under UV-visible light irradiation. (d) UV-visible absorbance spectrum of P25 and lh-P25 before and after the deposition of CdSe. The inset image shows the TEM image of CdSe QD with lattice spacing of 0.31nm decorated on TiO₂.

Figure 6. Optical features of P25 P25/p-NWs, p-P25, and lh-P25 (p-P25/p-NWs). (a) Reflectivity, (b) Diffuse reflector spectrum of the samples under UV-visible irradiation.

Figure 7. TEM images of (a) CdSe and (b) CdSe/lh-P25.

Figure 8. Transmittance spectra of the UV-cutoff filter

Figure 9. Experimental setup for PEC measurements.

Figure 10. PEC performance of P25, lh-P25, CdSe/P25, and CdSe/lh-P25 under 1 sun irradiation (100 mW/cm^2). (a) J-V curve of P25 control and lh-P25 under UV-visible and dark conditions. (b) Schematic diagram showing hydrogen generating mechanism of CdSe/lh-P25. (c) J-V curve of CdSe/P25 and CdSe/lh-P25 under UV-visible, visible light irradiation, and dark conditions. (d) Measurement of the IPCE (incident photon-to-electron conversion efficiency).

Figure 11. (a) The chronoamperometry curve of CdSe/lh-P25 at a bias of 0.5 V under UV-visible and visible light irradiation. (b) Nyquist plots of CdSe/P25 and CdSe/lh-P25. The inset shows an equivalent circuit used for fitting data. (c) V_{oc} vs. time profile of CdSe/P25 and CdSe/lh-P25. (d) The electron lifetime calculated from the V_{oc} decay.

Figure 12. J-t curve of CdSe/lh-P25 under UV-visible illumination at a fixed bias of 0.5 V vs. Ag/AgCl, showing reasonable stability of the QD-sensitized PEC device.

Figure 13. Photoconversion efficiency of the PEC cell with CdSe/lh-P25 electrode as a function of applied potential.

Figure 14. Nyquist plots of P25, lh-P25, CdSe/lh-P25, and CdSe/lh-P25. The inset shows an equivalent circuit used for fitting data.

List of Table

[Chapter 2]

Table 1 Photovoltaic characteristics of the hybrid structure and conventional TiO₂ anode

[Chapter 6]

Table 1. EIS responses of CdSe/P25 and CdSe/lh-P25.

Chapter 1. Introduction of Periodic Nano-structure for Photovoltaic Device.

The demands for the clean energy is successively increased as time goes by due to the environmental pollution and lack of the fossil energy materials. The photovoltaic devices which can convert photon energy into the electron or chemical energy have been received extensive focus since solar light is almost unlimited energy source and they do not make any environmental pollution when they fabricate the electron or chemical materials.¹⁻³ However, the efficiency of the photovoltaic devices are still low to use it as real energy source due to low absorption, high recombination and poor surface are for energy materials. To address these problems, the size control is very efficient. We can manipulate the optical properties of the materials with the periodicity which has several hundred nanometer to increase the light absorption of the photovoltaic devices and extremely increase surface area of the energy materials with the tens of nm scale size.⁴⁻⁶ The periodic structures of subwavelength size materials can be used as the special optical layer such as antireflection layer, diffraction grating and light trapping layer.⁷ The Moth-eye which composed of very fine periodic protuberances is the representative antireflection layer from the nature. The working of a moth eye surface can be understood in terms of a gradually changing refractive index variation of the surface layer from unity to that of the bulk material. If without a periodic protuberance layer the Fresnel reflection coefficient at an interface of two media is equal to $[(n_1 - n_2)/(n_1 + n_2)]^2$,⁸ where n_1 and n_2 are the refractive indices of the media. However, we can consider the net reflectance as the resultant of an infinite series of reflections at each incremental change in index. Because each reflection is attributed to a different depth from the surface, each will have a different phase. When the transition occurred over an optical distance of $\lambda/2$, there will be destructive interface and the reflectance will fall to zero. The spacing d of the protuberances should be sufficiently small that periodic structure cannot be resolved by the incident light. If spacing d is increased, the array will become the diffraction grating.⁹⁻¹¹

Because most of photovoltaic devices do not absorb the 100% of solar light to generating the photo-excited electron-hole pairs, the scattering or light trapping layers were adopted to increase the light absorption. Although large sized TiO_2 particles were widely used for the efficient Mie scattering on the 20 nm sized TiO_2 paste, large particles reduces the surface area for the dye absorption. The other way to increase the light absorption is using anti-reflection layer under the TiO_2 nanoparticle film. They reduce the reflection by acting similar to the diffraction grating layer. To fabricate the periodic structures for anti-reflection layer, photolithography process was widely used such as X-ray lithography, UV lithography. The X-ray lithography and UV lithography have been used to fabricate the 10~100nm of periodicity and several micrometer sized periodicity, respectively. These dimensions have the disadvantages for the increasing light scattering or anti-reflection since the visible light do not effectively react with the higher and lower dimensions than its wavelength (400nm~800nm).¹² To

address improper dimension match to visible wave length, we used the interference lithography technique as explained below.¹³

The issue of high surface area in the energy device field is very important for high performance since the electron-hole transfer or electron-hole generations are related with the surface area of the energy materials.¹⁴⁻¹⁶ High efficiency photovoltaic devices means that fast and large amount of charge exchange or transfer from materials to the electrolyte solution or charge collector. To increase the surface area of the materials, the tens of nanometer size pores are very efficient. If the pore size become several nanometer, electrolyte was not infiltrated in the materials and devices couldn't work. The self-assembled silica or polystyrene nanoparticles were widely used as the template converting materials to inverse opal structures.¹⁷⁻¹⁹ In this thesis, we fabricated the periodic anti-reflection layer for enhancing photovoltaic devices and high surface area of 3D-graphene and 3D-Fe₂O₃ for the high performance photovoltaic devices such as Dye-sensitized solar cell (DSSCs) or Photoelectrochemical water splitting cell (PEC) by using interference lithography, soft-lithography and 3D silica template. The periodic materials can increase the performance of photovoltaic devices by increasing optical property and enhancing surface area of the materials.

1.1 Mie scattering

The Mie scattering is the representative phenomena of interaction between subwavelength scale materials and light. Common light scattering theory can be divided in terms of two theoretical category. One is the Rayleigh scattering which describes the light scattering by spheres which are much smaller than the wavelength of light. The intensity of the Rayleigh scattered electromagnetic wave is significantly increased when the ratio of particle size to wavelength is increased. When the particle size is greater than about 10% of the wavelength of the light, the Rayleigh scattering model is broken down. If the particle size is larger than this, Mie scattering model can be used to analysis of the scattered waves. It is relatively independent of wavelength and it is larger in the forward direction than in the reverse direction. The greater the particle size, the more of the light is scattered in the forward direction.²⁰⁻²²

The diffraction grating is also very effective optical layer with a periodic array, which splits and diffracts light into several radiations in different directions. The directions of these radiations is affected by the spacing of the grating and the wavelength of the light.²³ The diffraction grating layer which composed of a set of slits of spacing d , that should be wider than the wavelength to cause diffraction is idle. After diffraction grating layer was resolved by light, the diffracted light consist of the sum of interfering wave components arising from each slit in the grating. The phenomenon of constructive and destructive interference is occurred by changing the path length through grating layers. So the peaks and valleys are created due to the interferences of wave. When the path difference between the light

from adjacent slits is equal to half the wavelength, $\lambda/2$, the waves are canceled and create the points of minimum intensity. However, when the path difference is λ , the waves are added each other and create the points of maximum intensity.²⁴⁻²⁵

1.2 Photonic crystal

The photonic crystals are periodic dielectric nanostructures that can create the optical band gap similar way that ionic lattices affect electron band gap in solids. Photonic crystals can be fabricated for one, two, or three dimensions. One-dimensional photonic crystals can be generated by depositing or stacking the layers. Two-dimensional ones can be fabricated by drilling holes or photolithography on the substrate. To fabricate the three-dimensional ones, stacking 2D layer, two-photon lithography, self-assembly of nano-spheres were widely used. Photonic crystals can reflect specific wave length as the scale dimension of the periodic structures. These diverse dimensional periodic structures can enhance the performance of the photovoltaic devices such as Dye-sensitized solar cell (DSSCs) or Photoelectrochemical water splitting cell (PEC) by increasing optical properties.²⁶⁻²⁷

1.3 Interference Lithography

To fabricate the subwavelength scale template, photo-lithography is a very sophisticate, efficient, and fast technique. However, traditional photolithography should need the photo mask to fabricate the exact shape of the template and size of the mask is limited in the micro scale due to diffraction from the mask. The Su-8 is a negative photoresist which is widely used in the photolithography. It is very viscous polymer that can be spun or spread over a thickness ranging from hundreds of nanometer to hundreds of micrometers.

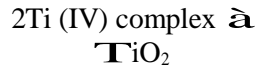
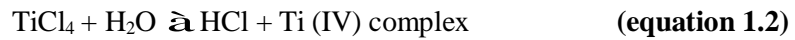
The Interference Lithography (IL) can complement the problems of the traditional photolithography. In the IL setup, from hundreds of nanometer to micron size of polymer template can be fabricated without photomask. In this work, the set-up of IL is made of He-Cd (365 nm) laser, pinhole, Lloyd's mirror and several optics. The Lloyd's-Mirror consists of an aluminum mirror (Edmund optics), which has a high reflectivity (> 92%) for the He-Cd laser, was placed vertically to the sample holder. To enhance the UV reflectivity over a broad range of angles, the aluminium mirror was chosen. The laser is passed through spatial filter and expanded through a pinhole to generate a Gaussian beam with a 20 cm in diameter at the sample holder. The substrate on the sample holder received the two beam which composed of the directly exposed and reflected UV beam by mirror at same time. The periodicity can be determined by the incident angle and the size of the polymer template can be varied by the heating and exposure time. The periodicity can be calculated by equation 1.1

$$= \text{---} \quad \text{(equation 1.1)}$$

Where P is periodicity, λ is the wave length of laser and Θ is an incident angle.²⁸⁻²⁹

1.4 Hydrothermal growth.

Hydrothermal growth can be explained as a method of synthesis of single crystals such as semiconductor nanowire which depends on the solubility of materials under high pressure with hot water. The nanowire growth is conducted in a tools composed of a steel autoclave with nutrients in the water. A temperature and concentration of nutrient is main factors to determine size and diameter of the nanowires. The hydrothermal method has the some advantages over the other method including the ability to fabricate crystalline phases which are unstable at the melting point. The Hydrothermal growth is also specially proper to the growth of large good-quality nanowires while maintaining good control over their composition. For example, the Titanium dioxide (TiO₂) nanowire can be synthesized through equation 1.2 in the Titanium precursor solution in water and HCl.



The dehydration of the 2Ti (IV) complexes can fabricate the TiO₂ nanowires along the [001] direction. The morphology of the TiO₂ can be determined by temperature of growth chamber and concentration of Ti procusors.¹⁹⁻²⁰

1.5 Dye-sensitized solar cell (DSSC)

Dye-sensitized solar cell is one of the most efficient solar cell which composed of working electrode, electrolyte and counter electrode. The dye on the TiO₂ paste in the working electrode are absorb the light and generate the electron-hole pairs. The excited electron can be reached to the counter electrode and the holes are recovered by the iodine electrolyte. After restore the dye, the iodine ions can be diffused to the counter electrode and are reduced at the counter electrode. Repeating this cycle, the DSSC cell can be worked for a long time.^{28,29}

1.6 Photoelectrochemical cell (PEC)

The PEC water splitting is a method which convert solar energy to chemical energy in the form of oxygen and hydrogen gas by using semiconductor materials. The set-up of the PEC cell consist of the photoanode, electrolyte, reference electrode and counter electrode. When the semiconductor materials absorb the light which is similar energy of the band gap of semiconductor, the electron-hole pairs are generated in the semiconductor. The electrons are flowed to the counter electrode to react with the hydrogen ion and then the hydrogen gas are generated. The hole from semiconductors can move to the interface semiconductor-electrolyte and react with the water which generate the oxygen gas.²⁸⁻²⁹

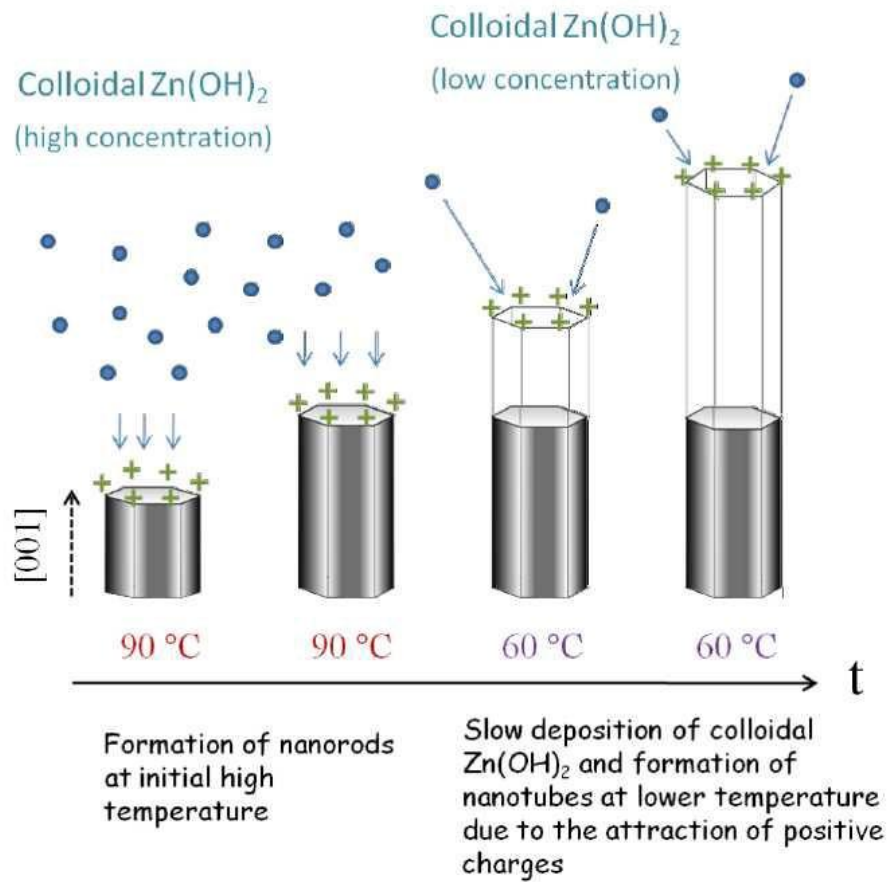


Figure 1. Mechanism of the hydrothermal growth.¹⁹

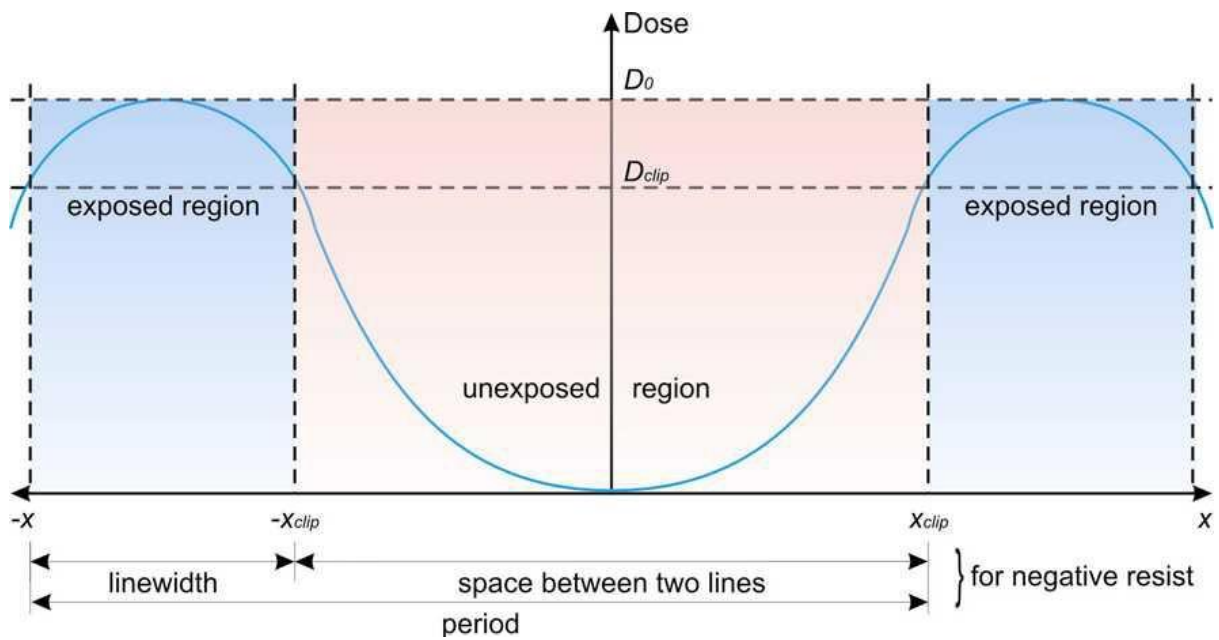
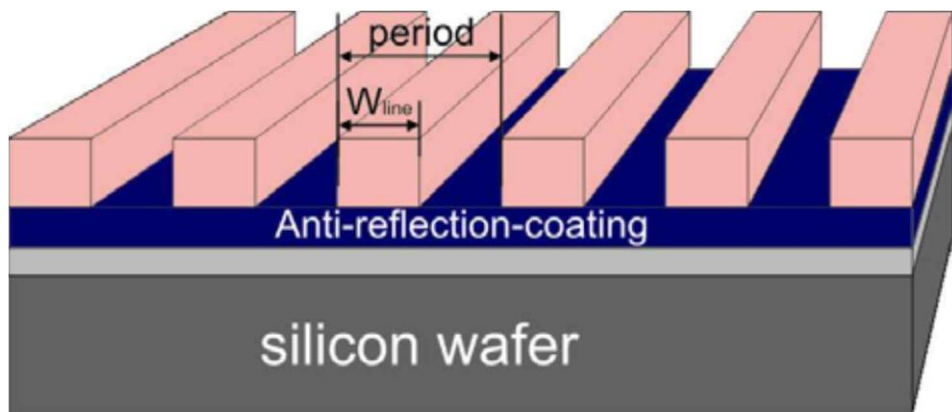


Figure 2. The mechanism of the interference lithography.²¹

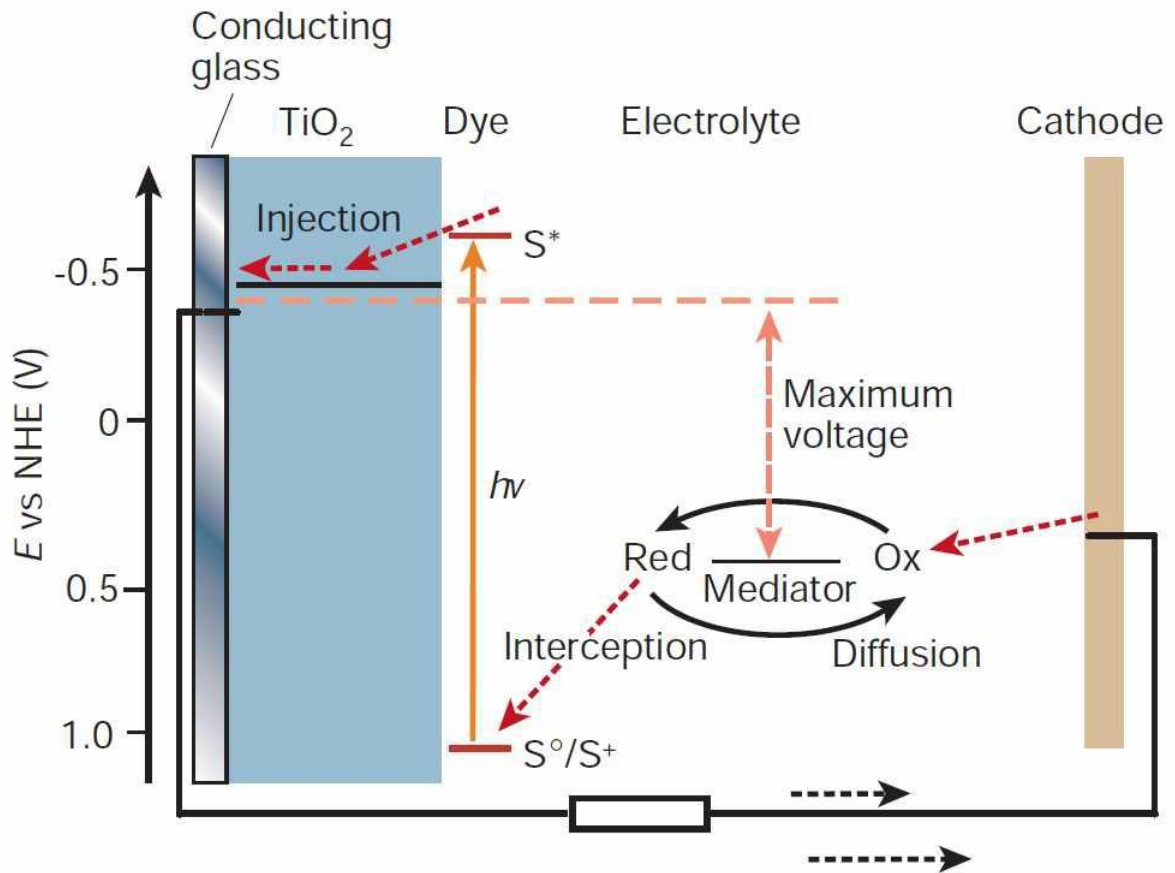


Figure 3. The mechanism of the Dye-sensitized Solar cell.²⁹

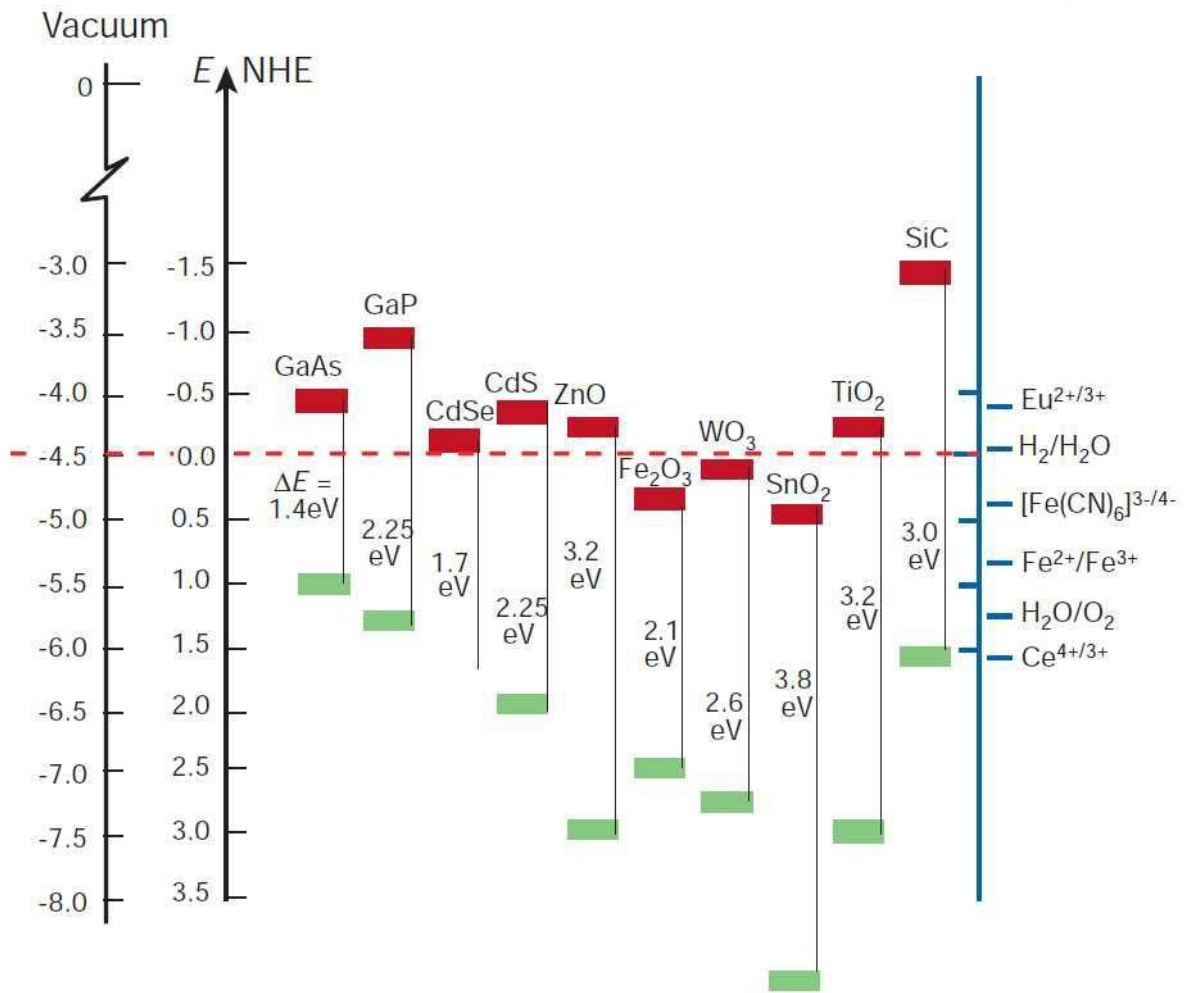


Figure 4. The energy level diagram of the semiconductors.²⁹

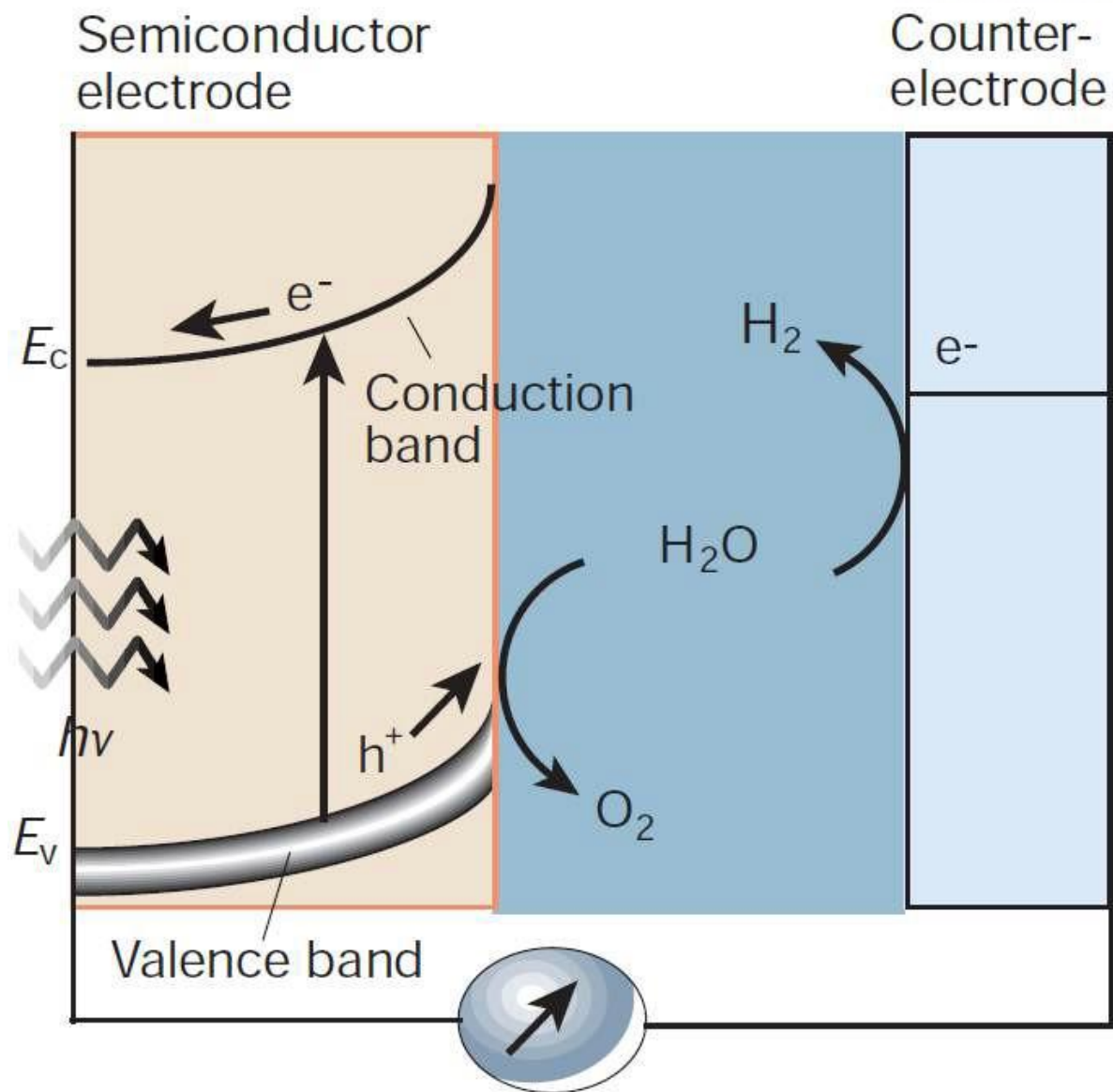


Figure 5. The mechanism of photocatalytic water splitting for n-type semiconductor.²⁹

REFERENCES

1. Cao, D.; Luo, W.; Feng, J.; Zhao, X.; Li, Z.; Zou, Z., Cathodic shift of onset potential for water oxidation on a Ti⁴⁺ doped Fe₂O₃ photoanode by suppressing the back reaction. *Energy. Environ. Sci.* 2014, 7 (2), 752-759.
2. Fujishima, A.; Honda, K., ELECTROCHEMICAL PHOTOLYSIS OF WATER AT A SEMICONDUCTOR ELECTRODE. *Nature* 1972, 238 (5358), 37-+.
3. Gratzel, M., Photoelectrochemical cells. *Nature* 2001, 414 (6861), 338-344.
4. Cho, C.-Y.; Moon, J. H., Hierarchically Porous TiO₂ Electrodes Fabricated by Dual Templating Methods for Dye-Sensitized Solar Cells. *Adv. Mater.* 2011, 23 (26), 2971-2975.
5. Toster, J.; Iyer, K. S.; Xiang, W.; Rosei, F.; Spiccia, L.; Raston, C. L., Diatom frustules as light traps enhance DSSC efficiency. *Nanoscale* 2013, 5 (3), 873-876.
6. Kushwaha, M. S.; Halevi, P.; Dobrzynski, L.; Djafari-Rouhani, B., Acoustic band structure of periodic elastic composites. *Phys. Rev. Lett.* 1993, 71 (13), 2022-2025.
7. Yablonovitch, E.; Gmitter, T. J.; Leung, K. M., Photonic band structure: The face-centered-cubic case employing nonspherical atoms. *Phys. Rev. Lett.* 1991, 67 (17), 2295-2298.
8. Wiscombe, W. J., Improved Mie scattering algorithms. *Appl. Opt.* 1980, 19 (9), 1505-1509.
9. Ashkin, A.; Dziedzic, J. M.; Bjorkholm, J. E.; Chu, S., Observation of a single-beam gradient force optical trap for dielectric particles. *Opt. Lett.* 1986, 11 (5), 288-290.
10. Clemens, N. T.; Mungal, M. G., A planar Mie scattering technique for visualizing supersonic mixing flows. *Exp. Fluids* 1991, 11 (2-3), 175-185.
11. Wilson, S. J.; Hutley, M. C., The Optical Properties of 'Moth Eye' Antireflection Surfaces. *Optica Acta: International Journal of Optics* 1982, 29 (7), 993-1009.
12. Huang, Y.-F.; Chattopadhyay, S.; Jen, Y.-J.; Peng, C.-Y.; Liu, T.-A.; Hsu, Y.-K.; Pan, C.-L.; Lo, H.-C.; Hsu, C.-H.; Chang, Y.-H.; Lee, C.-S.; Chen, K.-H.; Chen, L.-C., Improved broadband and quasi-omnidirectional anti-reflection properties with biomimetic silicon nanostructures. *Nat Nano* 2007, 2 (12), 770-774.
13. Yamada, N.; Kim, O. N.; Tokimitsu, T.; Nakai, Y.; Masuda, H., Optimization of anti-reflection moth-eye structures for use in crystalline silicon solar cells. *Progress in Photovoltaics: Research and Applications* 2011, 19 (2), 134-140.
14. Wang, S. S.; Moharam, M. G.; Magnusson, R.; Bagby, J. S., Guided-mode resonances in planar dielectric-layer diffraction gratings. *Journal of the Optical Society of America A* 1990, 7 (8), 1470-1474.
15. Hutley, M. C.; Maystre, D., The total absorption of light by a diffraction grating. *Opt. Commun.* 1976, 19 (3), 431-436.
16. Botten, L. C.; Craig, M. S.; McPhedran, R. C.; Adams, J. L.; Andrewartha, J. R., The Finitely

- Conducting Lamellar Diffraction Grating. *Optica Acta: International Journal of Optics* 1981, 28 (8), 1087-1102.
17. Akahane, Y.; Asano, T.; Song, B.-S.; Noda, S., High-Q photonic nanocavity in a two-dimensional photonic crystal. *Nature* 2003, 425 (6961), 944-947.
 18. Mekis, A.; Chen, J. C.; Kurland, I.; Fan, S.; Villeneuve, P. R.; Joannopoulos, J. D., High Transmission through Sharp Bends in Photonic Crystal Waveguides. *Phys. Rev. Lett.* 1996, 77 (18), 3787-3790.
 19. Blanco, A.; Chomski, E.; Grabtchak, S.; Ibisate, M.; John, S.; Leonard, S. W.; Lopez, C.; Meseguer, F.; Miguez, H.; Mondia, J. P.; Ozin, G. A.; Toader, O.; van Driel, H. M., Large-scale synthesis of a silicon photonic crystal with a complete three-dimensional bandgap near 1.5 micrometres. *Nature* 2000, 405 (6785), 437-440.
 20. Lin, S. Y.; Fleming, J. G.; Hetherington, D. L.; Smith, B. K.; Biswas, R.; Ho, K. M.; Sigalas, M. M.; Zubrzycki, W.; Kurtz, S. R.; Bur, J., A three-dimensional photonic crystal operating at infrared wavelengths. *Nature* 1998, 394 (6690), 251-253.
 21. Divliansky, I.; Mayer, T. S.; Holliday, K. S.; Crespi, V. H., Fabrication of three-dimensional polymer photonic crystal structures using single diffraction element interference lithography. *Appl. Phys. Lett.* 2003, 82 (11), 1667-1669.
 22. Solak, H. H.; David, C.; Gobrecht, J.; Golovkina, V.; Cerrina, F.; Kim, S. O.; Nealey, P. F., Sub-50 nm period patterns with EUV interference lithography. *Microelectron. Eng.* 2003, 67-68 (0), 56-62.
 23. Jang, J. H.; Ullal, C. K.; Maldovan, M.; Gorishnyy, T.; Kooi, S.; Koh, C.; Thomas, E. L., 3D Micro- and Nanostructures via Interference Lithography. *Adv. Funct. Mater.* 2007, 17 (16), 3027-3041.
 24. Sunandan, B.; Joydeep, D., Hydrothermal growth of ZnO nanostructures. *Science and Technology of Advanced Materials* 2009, 10 (1), 013001.
 25. Liu, B.; Aydil, E. S., Growth of Oriented Single-Crystalline Rutile TiO₂ Nanorods on Transparent Conducting Substrates for Dye-Sensitized Solar Cells. *J. Am. Chem. Soc.* 2009, 131 (11), 3985-3990.
 26. Wang, P.; Zakeeruddin, S. M.; Moser, J. E.; Nazeeruddin, M. K.; Sekiguchi, T.; Gratzel, M., A stable quasi-solid-state dye-sensitized solar cell with an amphiphilic ruthenium sensitizer and polymer gel electrolyte. *Nat Mater* 2003, 2 (6), 402-407.
 27. Mor, G. K.; Shankar, K.; Paulose, M.; Varghese, O. K.; Grimes, C. A., Use of Highly-Ordered TiO₂ Nanotube Arrays in Dye-Sensitized Solar Cells. *Nano Lett.* 2006, 6 (2), 215-218.
 28. Khan, S. U. M.; Al-Shahry, M.; Ingler, W. B., Efficient Photochemical Water Splitting by a Chemically Modified n-TiO₂. *Science* 2002, 297 (5590), 2243-2245.
 29. Gratzel, M., Photoelectrochemical cells. *Nature* 2001, 414 (6861), 338-344.

Chapter 2. Power Conversion Efficiency Enhancement Based on the Bio-inspired Hierarchical Antireflection Layer in Dye Sensitized Solar Cell

1. Introduction

The dye-sensitized solar cell (DSSC), a solar cell composed of a few- μm of nanoparticle TiO_2 layer decorated with a dye as a working electrode and a layer of Pt nanoparticles deposited onto a Fluorine doped tin oxide (FTO) as a counter electrode, has attracted much attention due to its high performance and low fabrication cost.¹⁻² Electrons generated by the photoexcitation of dyes by solar light irradiation transfer via the TiO_2 nanoparticle thin film to the collecting FTO substrate fabricating a closed circuit by offering electron back to the dyes through the iodine electrolyte solution. It is particularly important to apply a properly designed structure with a maximized light absorption for realizing a highly efficient DSSC, because the power conversion efficiency (PCE) of the DSSC strongly depends on the absorption properties of the solar cell.³⁻⁵ It has been elucidated that the periodic morphology of device is widely believed to be major factor for efficient light trapping.⁶ For example, rough surface at the back or front of the TiO_2 /dye in the thin nanoparticle layers can enhance the path length of the light by scattering and consequently increase absorption.⁷

A diffraction grating (DG) is an optical equipment with a few hundred nanometers scale of periodic structure, which splits photon into several beams travelling in diffraction paths.⁸ After light is resolved by the grating, the diffracted light is consisted of the sum of interfering wave components stemming from each slit in the grating. It has been studied that the optical path length can be enhanced via scattering or diffraction.⁹⁻¹⁰ In fact, higher order diffracted light can have advantage in light harvesting in that it may induce total inter reflection (TIR) in addition to providing longer optical interaction lengths.

Nanocrystalline- TiO_2 (NC- TiO_2) particles with a diameter of 25 nm, which have been widely used for the creation of the working electrode in the conventional DSSC with a large surface area, thereby maximizing the photoexcitation of dye molecules. However, they are poor light scatterers; this results in relatively low light harvesting in the red and near-infrared region of the light spectrum, because effective scatterings are mainly occurred by structures which have a sub-wavelength dimension. Alternatively, a new type of optical component, monodisperse TiO_2 beads with a few nanometer-sized diameter, has been adopted as a highly efficient scatterer to enhance the light path length in the solar cell.¹⁰⁻¹¹ However, the efficiency of DSSC is limited by a relatively low V_{oc} due to their lower surface area caused by the adoption of larger particles. Upon this background, a comprehensive knowledge of the relation between the efficient light trapping structures and the surface area of the active materials is

important to design and optimize a highly efficient DSSCs.

To increase the PCE of solar cells, the introduction of antireflection (AR) layer is one of effective way with relatively low-cost. Anti-reflection layers have been widely used for increasing efficiency of silicon solar cell, since silicon reflected much solar light which cannot be used as source of photoexcitation for solar cell.¹²⁻¹⁵ The AR structure of moth-eye surface¹⁶ or grating-like structures in the yellow and brown colored cuticle of the Oriental hornet have good examples of bio-inspired optical elements increasing the solar collections achieved by a textured surface of the antireflection layer.¹⁷⁻¹⁹

A subwavelength scale dimension grating layer work for these purposes since the dimensions of these structures which are much smaller than the wavelength of light can absorb more photon by the effective interference of light. The nanoporous structures allows the manipulation of the effective refractive index between the air and material, which helps reduce light losses in the nanostructure. The high-performance DSSCs with an interface between relatively low refractive index of FTO layer and the high refractive index TiO₂ need a periodic diffraction grating surface as an antireflective layer to reduce reflectance and to enhance optical path length of the diffracted light for maximized light trapping.

Interference lithography (IL)²⁰⁻²² is an efficient, trustworthy and dependable method for the creation of large area, defect-free nanostructures by transferring the light intensity distribution into a light sensitive medium. Through the proper choice of beam parameters, the volume fraction and geometry of the polymer nanostructures can be exactly controlled. An advantage of IL in filed where solar light is used as a source for photoexcitation is that it allow easy access to periodic structures with a scale of a subwavelength without defects, whose size is especially important for effective light trapping.

Here we report the synergic effect of a bio-inspired AR layer in the form of a 2-dimensional (2D) TiO₂ diffraction grating (DG) fabricated via IL with a working electrode of TiO₂ nanocrystalline thin film in a DSSC in order to increased light trapping property. The size of holes in the polymer templates was determined through control of the wave vectors and polarization vectors of the exposed laser. After TiO₂ nanowires (NWs) were grown by hydrothermal growth in the periodic holes of polymer templates, the polymer templates are removed by sintering at high temperature. A dual-scale nano-periodic pattern, which not only exhibits superior antireflection but also increased scattering/diffraction has been applied to minimize the loss in surface area. In contrast with a conventional DSSC, the hybrid structure with the dual-scale AR layer demonstrates stronger light absorption in the UV-visible region, leading to both a greater PCE and IPCE in the overall spectral range. The improved performance of the DSSC coupled with the periodic AR layer can be explained by the maximized photon trapping in the visible light region of the solar spectrum by the introduction of a high index-contrast nano-periodic structure with comparable lattice parameters to the wavelength of exposed light. The high performance of the hybrid nanostructures as photoanode in a DSSC indicates that properly designed hybrid nano-structures will open up the possibility of enhanced performance for energy related materials such as the electrodes for

silicon, organic solar cells and the substrates for surface enhanced Raman spectroscopy.

2. Experimental and characterization

2.1 Fabrication of 2-dimensional Diffraction Grating layer in Polymer template

The FTO substrates were cleaned using ultra-sonication with acetone, IPA, and de-ionized water for 10 min and dried by N₂ gas blowing. A 300 nm thick Su-8 photoresist film was deposited by spin-coating at 3000rpm on a 40mM of TiCl₄ treated FTO substrate. 2-dimensional square patterns with circular holes template were fabricated using interference lithography. The Su-8/FTO samples were double exposed for 8 x 8s by 90 degrees rotating the sample. Before developing the Su-8 photoresist using PGMEA, a post-exposure bake was carried out at 75 °C for 10min. The diameter and periodic cycle of the patterns were found to be 380 nm and 550 nm, respectively, from SEM measurements.

2.2 Fabrication of DSSC with the photoanode coupled with the hierarchical AR layer

TiO₂ NWs were grown by placing the substrates which have the 2-D polymer periodic pattern fabricated via IL in the solution of 20 mL of toluene, 0.5g of tetrabutyl titanate, 0.5 mL of titanium tetrachloride (1 M in toluene), and 1 mL of hydrochloric acid (37 wt %) in 30mL of the teflon reactor at 180°C for 1h. The 2-D periodic polymer template was removed by sintering at 500°C for 1h. A layer of NC-TiO₂ (solaronix Ti-nanoxide T/SP) was pasted on top of pre-patterned rutile nanowires by doctor blading followed by heating at 120 °C for 10 min. The film was then burned out at 500 °C for 30 min. This doctor blading procedure with paste (coating, drying, and sintering) was repeated to obtain a 12 μm of working electrode. The TiO₂ electrode was immersed in a 0.5 mM N-719 dye (Solaronix) solution in a solution of acetonitrile and tert-butyl alcohol (v/v: 1:1) and kept at room temperature for 18 hrs. A commercial available Pt catalyst (Solaronix platiso T) was coated on the FTO glass and sintered at 430oC for 30min to fabricate a platinum counter electrode. The preparation procedure of Pt coating was repeated 3times to obtain high performance. The dye-deposited TiO₂ with a dimension of 0.21 cm² (7 mm × 3 mm) and a platinum counter-electrode were assembled into a sandwich-type cell and sealed with hot-melt surlyn (Solaronix) with a thickness of 60 um. An iodine electrolyte (Solaronix Iodolyte AN-50) was injected via a hole on the back side of the Pt counter electrode.

2.3 Characterization

Photovoltaic efficiency of the DSSC was measured under AM 1.5 illumination (100 mWcm⁻², Oriel). EIS measurement was conducted using a potentiostat (prinstone, Versa STAT 3, AMETEK) and the data were fitted by using Zsimpwin 3.21 software. The acquired frequency ranged from 0.01Hz to 100 kHz with 10 mV AC amplitude. IPCE data were also carried out using an EQE system (Model QEX7) by

PV Measurements Inc. (Boulder, Colorado). The SEM images were obtained by a scanning electron microscope (FEI/USA Nanonova 230). The absorbance and reflectance spectrum were obtained using a Cary-100 conc UV/vis/NIR spectrophotometer (Varian). The diffuse reflectivity was collected by using a Belsorp max (Bel Japan). The NC-TiO₂ film thickness was measured using a surface profiler (P-6 KLA_Tencor/USA)

3. Results and Discussion

In a wide search of motivating organisms, moths confirmed to have the most efficient capabilities for the efficiency of solar cells in that it shows an extraordinary anti-reflective ability that is essential to their sight abilities. Several methods have been attempted to mimic moth-eye structure with a 2D pattern substrate, each approximately 200 nm high and spaced on 300 nm holes.^{11, 23-25} Figure 1a shows the schematic illustration for the fabrication of TiO₂ working electrode (V) with 2D rutile NW moth-eye inspired AR layer (IV) in the DSSC device (VI). As shown in the Figure 1b, the SEM images of a 2-dimensional patterned TiO₂ NWs grown in the holes of the polymer template generated by IL are shown. The SU-8 polymer template (II) fabricated here is an inverse structure of moth-eye motivated 500 nm-thick 2D square periodic pattern with diameter of 380 nm. The dimensions of the SU-8 templates were fabricated so that can efficiently reduce the reflectance as well as scatter the photons for an increased photon trapping ability. The TiO₂ NWs in the SU-8 template were grown using modified hydrothermal methods.¹³ The diameter and length of the nanowires can be tuned by changing the reaction times, concentrations of the precursors, and through other means. In particular, we have varied the amounts of precursor solutions in order to acquire TiO₂ NWs with diameters of 20-30 nm in a single SU-8 hole. A hierarchically patterned dual-scale TiO₂ NWs structure has been planned to minimize the loss of surface area for dye deposition and to obtain the superior antireflection and increased diffraction properties. Finally, the periodic SU-8 polymer patterns were burned out by sintering. Figure 1(c) is a SEM image of cross-sectional view of a NC-TiO₂ working electrode coupled with 2D patterned TiO₂ AR layer.

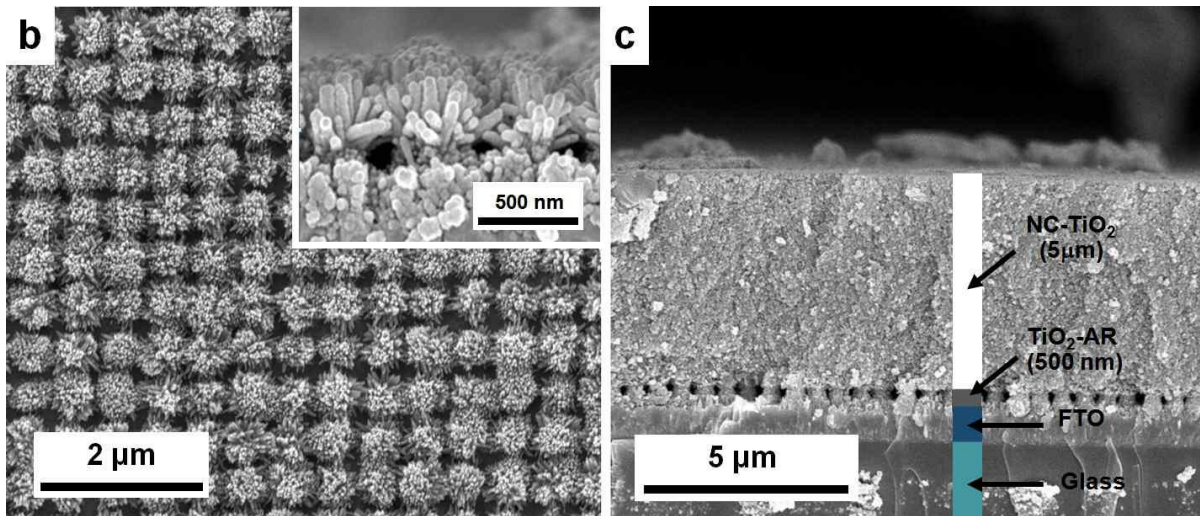
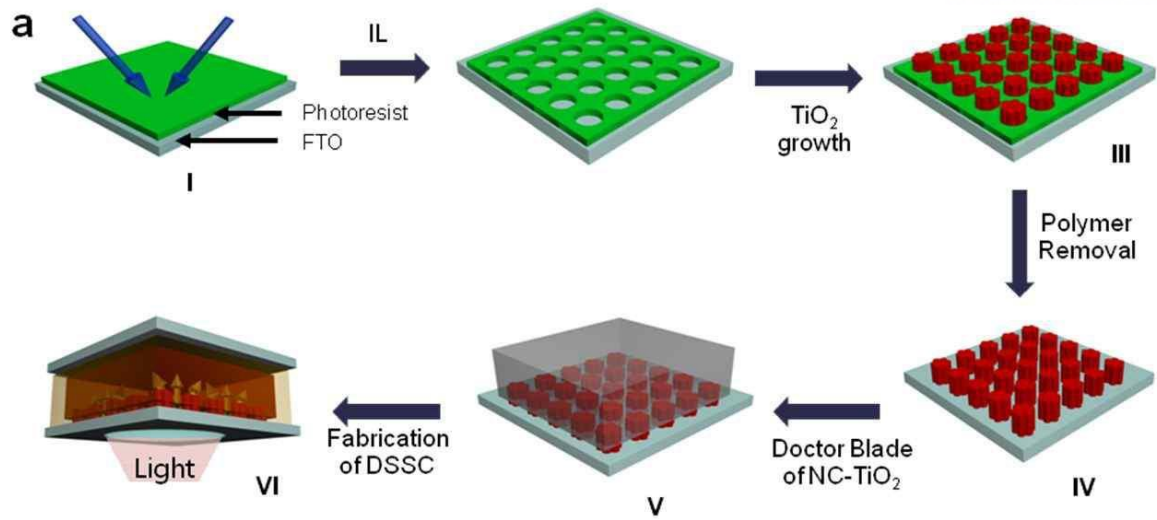


Figure 1. Schematic illustration for the fabrication of TiO₂ nanocrystalline electrode with moth-eye motivated anti-reflection layer in DSSC device (a) and SEM images of the TiO₂ nanowires (b, c): (b) The hybrid hierarchically patterned TiO₂ antireflection layer (IV). Inset image shows a cross-sectional image of dual-scale TiO₂ nanowires. (c) Cross-sectional image of the working electrode (V) consisted of a layer of NC-TiO₂ and an underlying patterned anti-reflection layer in TiO₂.

The photoanode (V) fabricated in this study is a double layered hierarchical nanostructure composed of a thin under-layer of AR (or DG) consisted of approximately 70-80 nm of TiO₂ nanowires with diameters of from 20 nm to 30 nm and heights of 500 nm in circular holes of 380 nm diameter in a square lattice and a 5mm- thick upper-layer of a conventional NC-TiO₂ structure. The surface area of the 5.5 mm-thick double layered structure obtained by BET was 109 cm²/g, which is slightly lower than that for a compact pure nanocrystalline TiO₂-NC film (117 cm²/g) due to the presence of the 500 nm-thick layer of larger scale patterns. Figure 2 shows the X-ray diffraction (XRD) pattern of hydrothermally prepared TiO₂ nanowires after calcination in air for 1hr at 550 °C. As-synthesized nanowires are rutile TiO₂ phase with a peaks in the (211), (101), and (110) planes as confirmed by JCPDS # 88-1175. The crystal structure of the annealed sample could be further proved by TEM measurement. Figure 2b shows a high-magnification TEM images of the TiO₂ nanowires verifying that the nanowires are crystalline with an lattice constant d-spacing of 0.24nm and 0.32 nm corresponding to (211) and (110) planes, respectively, of rutile TiO₂. It can be seen that the sintered TiO₂ nanowires are well connected and faceted NWs with an average diameter of about 20-30 nm in the rutile phase, in agreement with the obtained XRD pattern.

The enhanced antireflection property due to the coupling of properly designed underlying 300 nm thick dual-scale AR layer can be quantified by the reflection spectra measured by shining the light from the front glass side on a 5 um thick P25 NC-TiO₂ and 5.3 um of hierarchical nanostructures composed of 300 nm underlying periodic patterned TiO₂ NWs layer and 5 um NC-TiO₂ upper layer. In this configuration, the light goes through air/glass/FTO/(P-TiO₂ NWs)/TiO₂ NC hybrid structures from air to the TiO₂ NC layer, and it is thought that the majority of reflectance happens from the interface of FTO (n=1.7) and TiO₂(n=2.49) due to the remarkable difference of the refractive index. Figure 3a shows that the hierarchical TiO₂ structure with an underlying patterned TiO₂ nanowires layer gives much lower reflectance as compared to the reference structure with a pure TiO₂ nanocrystalline structure over the entire spectral range (nearly one order of magnitude lower at 460 nm). This means that much more light is absorbed by dyes and can be used in the light harvesting process in the DSSC solar cell. This is attributed to the gradual change of the refractive index due to the presence of the periodic patterned TiO₂ NW layer with the capability of modulating the effective refractive index according to the periodic vacancies of the patterned structure interface between the FTO glass and TiO₂ NC layers in the hybrid structure.

Next, in order to elucidate the intensity of diffusely reflected light under light irradiation on the TiO₂ hybrid substrate, the diffuse reflection spectrum of a pure TiO₂ thin film made from P25 nanocrystals, a hierarchically patterned anti-reflection layer of TiO₂ NWs, and hybrid nanostructure were measured. Interestingly, compared to the P25 NC-TiO₂ film, the films with a very thin AR layer showed significantly higher diffuse reflection spectra in the visible spectrum of light wavelengths (from 450 nm

- 650 nm), indicating that the absorbed light was efficiently scattered within the nanostructure film. This is attributed to increase of the light path within the TiO₂ nanostructure by adoption of a few hundred nanometer scale in the antireflection layer. The diffuse reflection spectrum do not show any slight difference between back side irradiation and front side irradiation. UV-vis spectroscopic experiments were further obtained so as to elucidate the final optical property of hybrid nanostructured TiO₂ with and without an antireflection layer. Figure 3c shows the UV-vis extinction spectra of a 5 μm thick plain NC-TiO₂ layer, 500 nm thick antireflection layer, and 550 nm height hybrid structure consisted of the two aforementioned layers illuminated at normal incidence from the glass side. The absorbance of peaks spanning 300 to 400 nm were allocated to the absorbance of the traditional TiO₂ nanoparticles. Interestingly, the latter two samples (even the 500 nm thick TiO₂-AR layer) demonstrated a more intense and wider spectroscopy with a broad and high absorption band ranging from 400 to 650 nm at the absorption maxima at 525 nm, 550 nm than the conventional TiO₂ nanocrystalline sample, even though a number of TiO₂ nanoparticles is much lower than that of NC-TiO₂ structure. The absorbance maximum for the hybrid hierarchical structure (P-NWs+NC) shows a blue-shift compared with that of periodic TiO₂ AR layer (P-NWs) due to the nanometer size of NC-TiO₂. The increased UV absorption of both samples with the diffraction grating (or AR) is ascribed to the synergy of scattering and antireflection effect taken by the higher size of nanostructures in the periodic patterned TiO₂ nanowires. As expected from the previous results, compared with the conventional layer of NC-TiO₂, the hybrid double layer structure assembled with an AR layer (P-NWs) in a larger dimension reduces the reflectance of the photons and adopt longer effective light path lengths and thus a clear and high absorbance band in the longer wavelength region ranging from 450 nm to 800 nm.

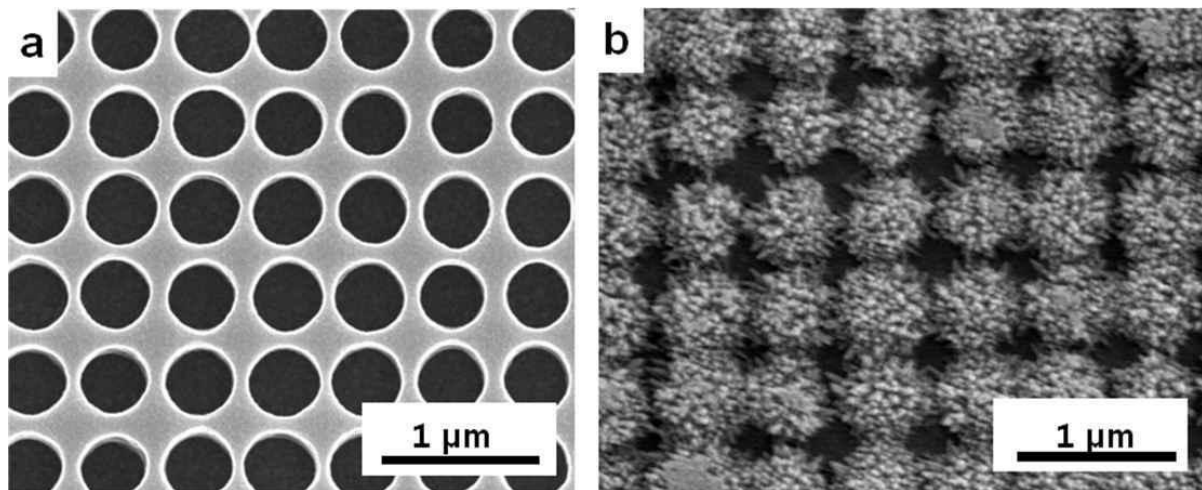


Figure 2: SEM images of a) SU-8 polymer template pattern b) periodic TiO₂ nanowires grown on FTO glass

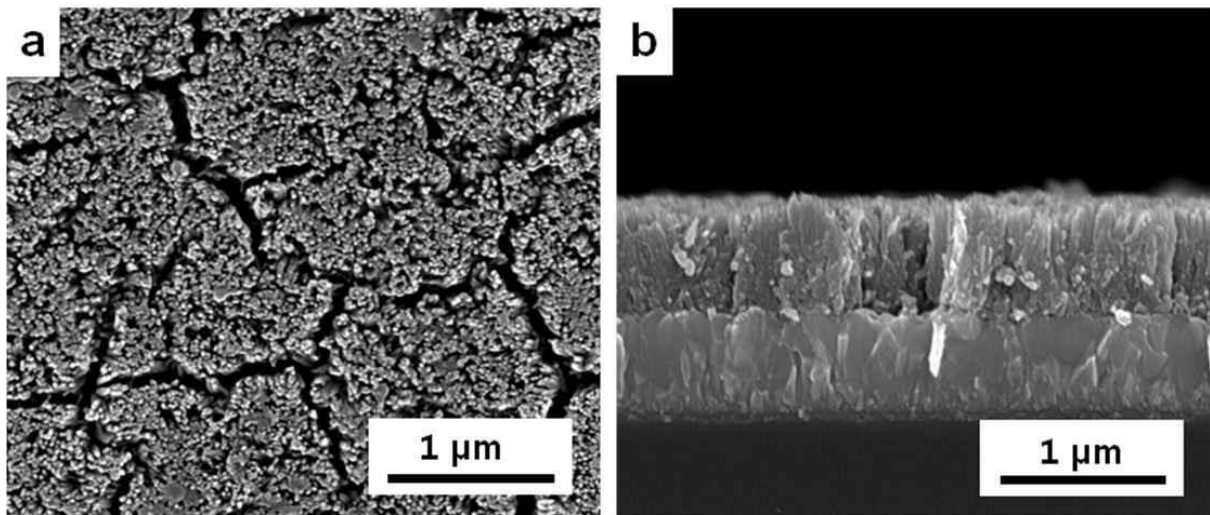


Figure 3. SEM images of a) TiO₂ nanowires; b) Cross-sectional view image of TiO₂ nanowires

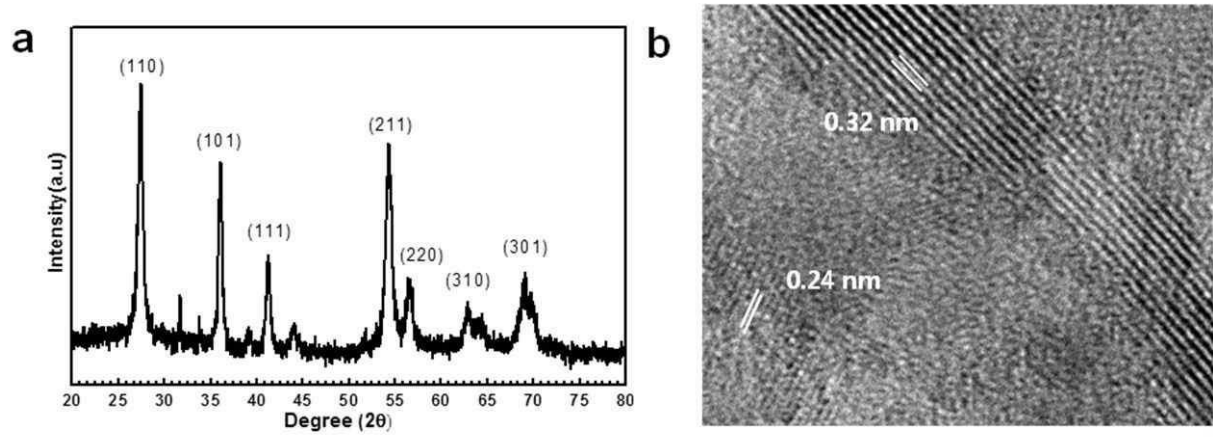


Figure 4. Confirmation of prepared TiO_2 hybrid sample: (a) XRD patterns of TiO_2 nanostructures. (b) HRTEM image of TiO_2 nanostructures.

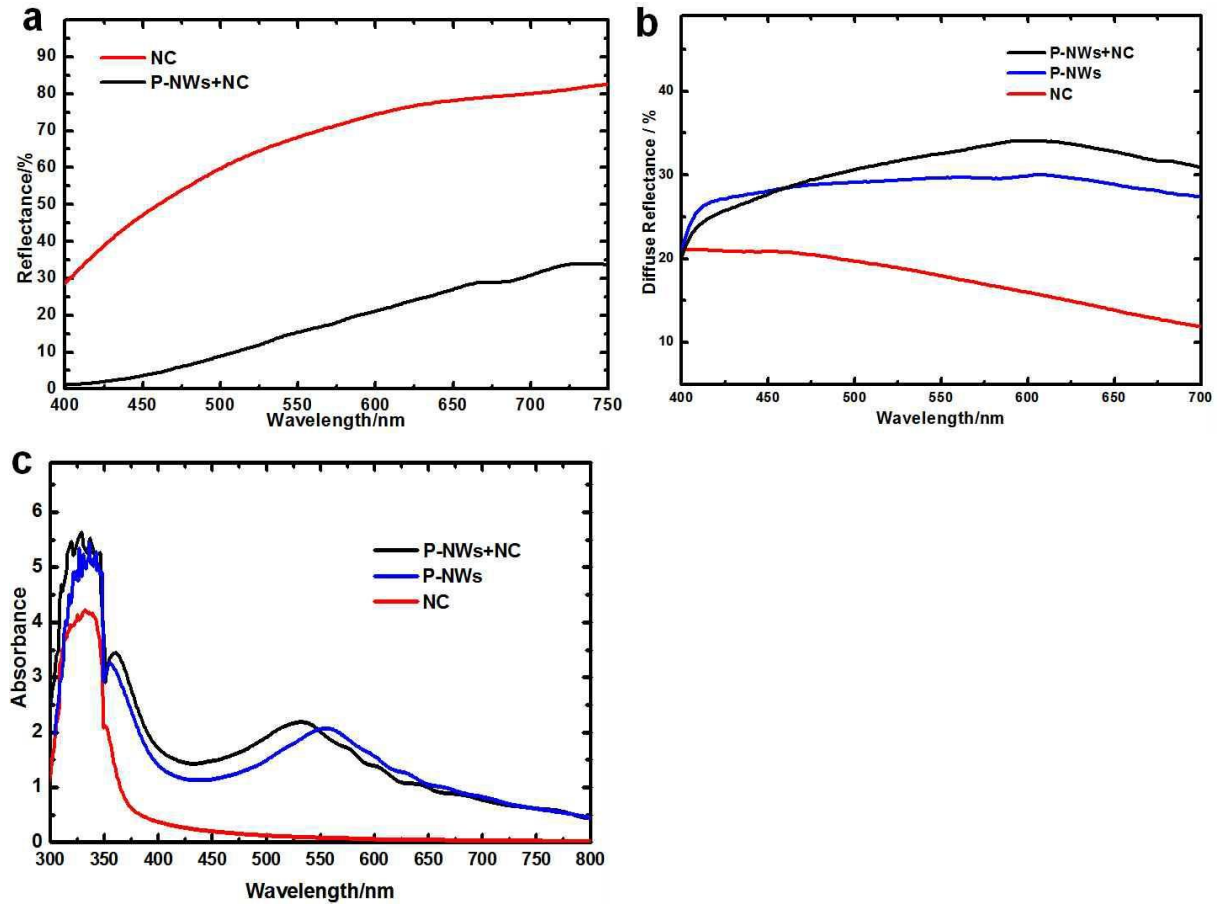


Figure 5. (a) Reflectivity spectrum measured, within the visible light wavelength range, on the pure TiO₂-NC structure and hybrid structure with an additional AR layer of TiO₂ nanostructure (P-NWs+NC). (b) Diffuse reflectance spectra and (c) UV-vis absorption spectra of the pure TiO₂-NC structure, pure patterned TiO₂ NWs structure, and hybrid structure composed of pure P25 NC and an additional AR layer of patterned TiO₂ NWs. All the measurements were taken without dye or electrolyte.

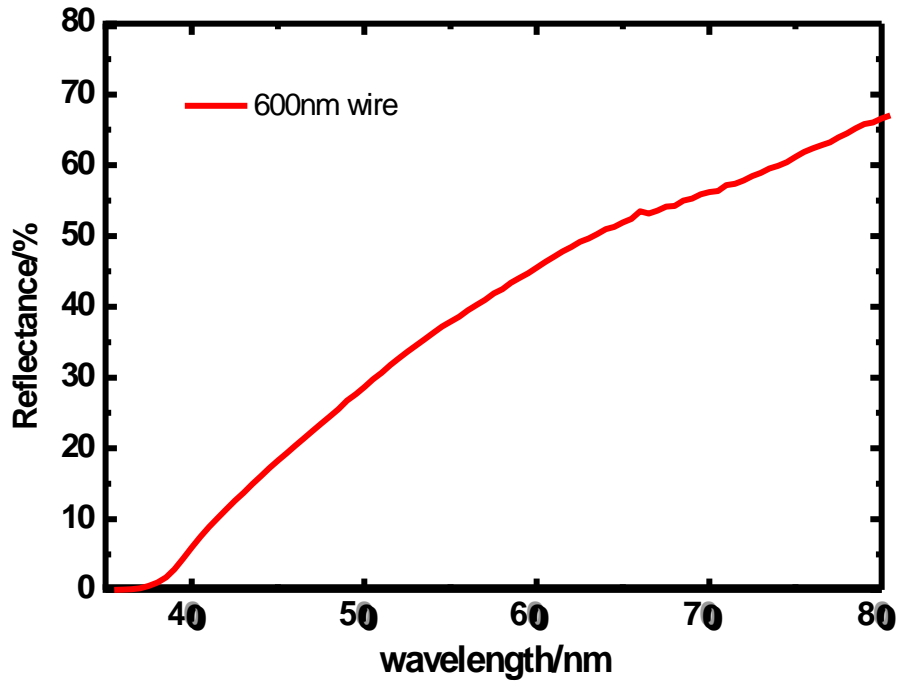


Figure 6. The reflectivity of 600 nm TiO₂ NWs

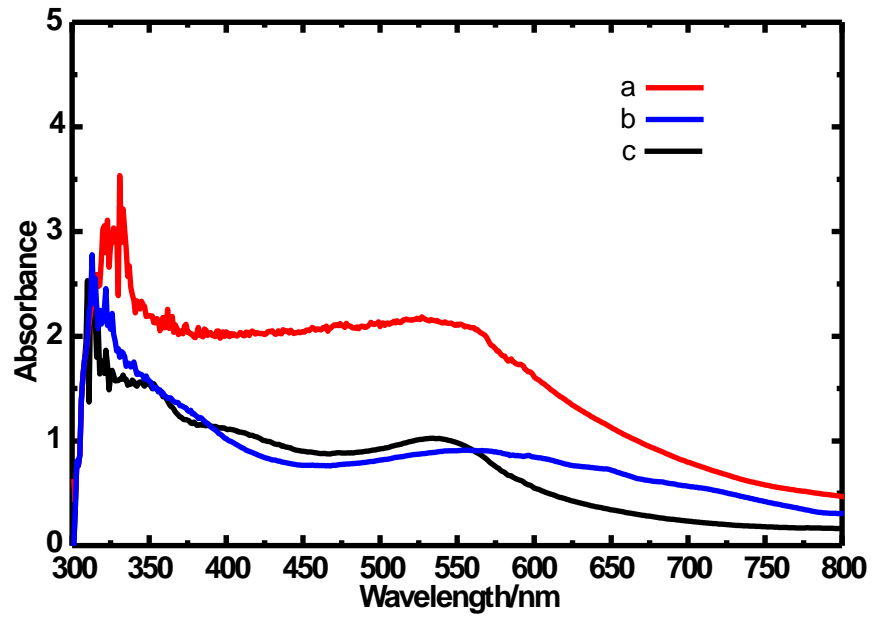


Figure 7. Absorbance spectra of TiO₂ NWs after N-719 dye absorption: a) 5.5 μ m hybrid structure; b) 500 nm TiO₂ NWs; c) 5 μ m NC-TiO₂ structure

To study the characteristics of the hybrid nanostructures as a photoanode for solar cells, the photovoltaic performances were obtained at 1-sun illumination condition. The incident photon-to-electron conversion efficiency (IPCE), the number of photoexcited electrons per incident photon, measured for the conventional TiO₂ anode and hybrid structure, is shown in Figure 4a. The broad IPCE curves, covering the visible spectrum from 380 nm-770 nm, exhibit a maximum of 60 % and 70% at 530-560 nm for the nanocrystalline TiO₂-NC film and hybrid structure, respectively, which proves the better PCE in hybrid cell. Current-voltage curves of the reference TiO₂-NC film cell and hybrid structure and a schematic diagram of a DSSC with a hybrid type photoanode are depicted in Figure 4b. The power conversion efficiency (η) of the hybrid structure with a periodic grating layer/5mm-thick TiO₂ nanocrystalline and the reference TiO₂ nanocrystalline cell with the same thickness is 6.5 % and 5.0 %, respectively. The efficiency of the enhanced photon trapping structure demonstrates 30% enhancement compared with the reference cell, which implies that a hierarchically patterned TiO₂ layer with relevant dimensions has a crucial impact on the efficiency of photovoltaic devices. Importantly, it can be seen that the photocurrent density of J_{sc} in the hybrid structure is notably higher while the open-circuit voltage (V_{oc}) is not affected by the added AR layer between TiO₂ NC and FTO, as shown in table 1. This is different from previously reported data that showed degradation of the V_{oc} and fill factor due to the greatly decreased surface area when a large beads scattering layer was used as light trapping structures. In our procedure, the fill factor (FF) is slightly decreased in the hybrid structure indicating the slower carrier mobility probably due to another junction between the NC-TiO₂ and AR layers. However, the V_{oc} remains the same due to the minimum loss in surface area of the hierarchically patterned structure. In order to obtain better insight into the dynamics of interfacial charge transfer processes, which are tightly related to the difference in current-voltage efficiency between two kinds of photoanode based DSSCs, electrochemical impedance spectroscopy (EIS) measurements on symmetrical dummy cells composed of two identical electrodes were carried out. The high frequency (around 100kHz) represents the sheet resistance (R_s) and the peaks between 1000Hz and 1Hz corresponds to the charge-transfer resistance (R_{ct}) at the TiO₂/dye/electrolyte interface, respectively in the Nyquist plots of the symmetric cells. As shown in Table 1, the periodic TiO₂ hybrid structure has a lower R_s ($R_s=1.9$) than the traditional TiO₂ photoanode ($R_s=2.4$), which exhibits the efficient photon trapping at the interface between the FTO substrates and TiO₂ nanowires AR layer as well as good adhesion to the substrate in the periodic hybrid structure. The strong connection between FTO and TiO₂ nanowires is likely due to the direct growth of TiO₂ nanowires on the FTO substrate in hybrid structure compared to the rough bonding taken by heating of NC-TiO₂ in the reference electrode. However, the R_{ct} value of the periodic TiO₂ hybrid structure was 0.96, which is slightly higher than 0.8 of the reference. This exhibits that

the reference TiO_2 electrode has a lower resistance at the interface of photoanode and iodine electrolyte than the TiO_2 hybrid-hierarchical structure with an additional interface of TiO_2 NWs and NC- TiO_2 does, which also explains lower fill factor in the hybrid structure (The additional resistance curve for this interface was not observed in the Nyquist plot). Although the hybrid structure have a slightly larger resistance and therefore, lower FF than the reference electrode, J_{sc} of hybrid structure is much higher than that of the reference, resulting in 30% of the overall power conversion efficiency enhancement, indicating that light harvesting by the introduction of a modified antireflective layer with minimum loss in surface area and the ability for higher scattering is efficiently balanced by the loss in interfacial resistance caused by the addition of another interface. We believe that further investigation of characteristics of the photovoltaic device can fully optimize charge mobility and recombination rates.

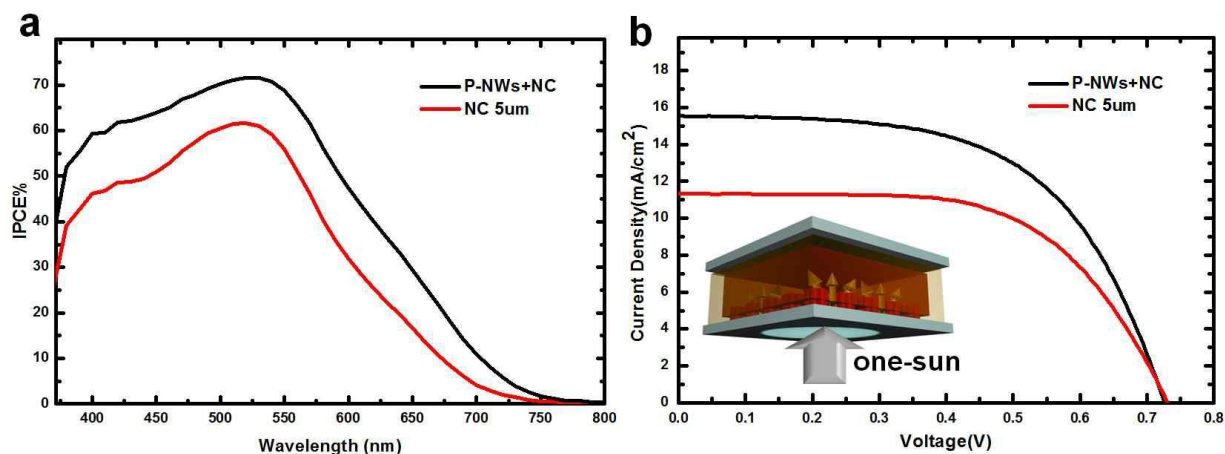


Figure 8. The photo-to-electron conversion efficiency of devices fabricated with and without the TiO_2 scattering and AR layer: (a) The incident photon-to-current collection efficiency (IPCE) spectra. (b) Current-voltage (I-V) curves for DSSCs using the hybrid structure (P-NWs+NC) and P25 NC. A schematic illustration of a DSSC with the hybrid type photoanode is inserted.

Table 1 Photovoltaic characteristics of the hybrid structure and conventional TiO_2 anode

	V_{oc} (mV)	J_{sc}	P_{max}	Fill Factor	R_s	R_{ct}	Efficiency
Reference	729	11.3	1.4	60.5	2.4	0.8	5.0
Hybrid	729	15.6	1.5	57.6	1.9	0.96	6.5

4. Conclusion

In conclusion, we have fabricated periodic hybrid TiO₂ structure incorporating a modified bio-inspired antireflection layer as photoanodes for use in DSSCs. A 500 nm thick hierarchically periodic 2D diffraction grating was introduced to maximize light trapping via effective lower reflection and increased photon scattering triggered by the dimensions of the nanostructure, which are comparable to the wavelength of exposed light. The photon trapping hybrid structure with minimum loss of surface area, achieved by the diffraction and antireflection, leads to a remarkable enhancement of absorbance in the red spectral range, resulting in a 30% increase in overall performance relative to solar cells prepared using pure P25 TiO₂ electrodes of same thickness. These results exhibit that the designed methodology is a low-cost and deterministic approach for achieving efficiency increase by photon trapping in a thin film DSSC.

5. REFERENCES

1. Gratzel, M., Photoelectrochemical cells. *Nature* **2001**, *414* (6861), 338-344.
2. Lee, C.; Kang, W.; Ko, M. J.; Kim, K.; Park, N. G., Study on the Change in Photovoltage by Control of Cell Gap in Dye-Sensitized Solar Cells. *J. Sol. Energy Eng. Trans.-ASME* **132** (2), 5.
3. Llopis, F.; Tobías, I., The role of rear surface in thin silicon solar cells. *Sol. Energy Mater. Sol. Cells* **2005**, *87* (1-4), 481-492.
4. Meng, S.; Ren, J.; Kaxiras, E., Natural Dyes Adsorbed on TiO₂ Nanowire for Photovoltaic Applications: Enhanced Light Absorption and Ultrafast Electron Injection. *Nano Lett.* **2008**, *8* (10), 3266-3272.
5. Colodrero, S.; Mihi, A.; Haggman, L.; Ocana, M.; Boschloo, G.; Hagfeldt, A.; Miguez, H., Porous One-Dimensional Photonic Crystals Improve the Power-Conversion Efficiency of Dye-Sensitized Solar Cells. *Adv. Mater.* **2009**, *21* (7), 764+.
6. Hore, S.; Vetter, C.; Kern, R.; Smit, H.; Hinsch, A., Influence of scattering layers on efficiency of dye-sensitized solar cells. *Sol. Energy Mater. Sol. Cells* **2006**, *90* (9), 1176-1188.
7. Garnett, E.; Yang, P., Light Trapping in Silicon Nanowire Solar Cells. *Nano Lett.* **2010**, *10* (3), 1082-1087.
8. Madzharov, D.; Dewan, R.; Knipp, D., Influence of front and back grating on light trapping in microcrystalline thin-film silicon solar cells. *Opt. Express* **2011**, *19* (6), A95-A107.
9. Hore, S.; Nitz, P.; Vetter, C.; Prahl, C.; Niggemann, M.; Kern, R., Scattering spherical voids in nanocrystalline TiO₂ - enhancement of efficiency in dye-sensitized solar cells. *Chemical Communications* **2005**, (15), 2011-2013.
10. Chen, D. H.; Huang, F. Z.; Cheng, Y. B.; Caruso, R. A., Mesoporous Anatase TiO₂ Beads with High Surface Areas and Controllable Pore Sizes: A Superior Candidate for High-Performance Dye-Sensitized Solar Cells. *Adv. Mater.* **2009**, *21* (21), 2206+.
11. Akira, U., Theoretical study of application of multiple scattering of light to a dye-sensitized nanocrystalline photoelectric cell. *Chemical Physics Letters* **1997**, *277* (1-3), 105-108.
12. Bouhafs, D.; Moussi, A.; Chikouche, A.; Ruiz, J. M., Design and simulation of antireflection coating systems for optoelectronic devices: Application to silicon solar cells. *Sol. Energy Mater. Sol. Cells* **1998**, *52* (1-2), 79-93.
13. Sheng, X.; Liu, J.; Kozinsky, I.; Agarwal, A. M.; Michel, J.; Kimerling, L. C., Design and Non-Lithographic Fabrication of Light Trapping Structures for Thin Film Silicon Solar Cells. *Adv. Mater.* **2011**, *23* (7), 843-847.
14. Shir, D.; Yoon, J.; Chanda, D.; Ryu, J.-H.; Rogers, J. A., Performance of Ultrathin Silicon Solar Microcells with Nanostructures of Relief Formed by Soft Imprint Lithography for Broad Band

- Absorption Enhancement. *Nano Lett.* **2010**, *10* (8), 3041-3046.
15. Zhu, J.; Hsu, C.-M.; Yu, Z.; Fan, S.; Cui, Y., Nanodome Solar Cells with Efficient Light Management and Self-Cleaning. *Nano Lett.* **2009**, *10* (6), 1979-1984.
 16. Chuang, S. Y.; Chen, H. L.; Shieh, J.; Lin, C. H.; Cheng, C. C.; Liu, H. W.; Yu, C. C., Nanoscale of biomimetic moth eye structures exhibiting inverse polarization phenomena at the Brewster angle. *Nanoscale* **2** (5), 799-805.
 17. Huang, Y.-F.; Chattopadhyay, S.; Jen, Y.-J.; Peng, C.-Y.; Liu, T.-A.; Hsu, Y.-K.; Pan, C.-L.; Lo, H.-C.; Hsu, C.-H.; Chang, Y.-H.; Lee, C.-S.; Chen, K.-H.; Chen, L.-C., Improved broadband and quasi-omnidirectional anti-reflection properties with biomimetic silicon nanostructures. *Nat Nano* **2007**, *2* (12), 770-774.
 18. Hadobas, K.; Kirsch, S.; Carl, A.; Acet, M.; Wassermann, E. F., Reflection properties of nanostructure-arrayed silicon surfaces. *Nanotechnology* **2000**, *11* (3), 161-164.
 19. Plotkin, M.; Hod, I.; Zaban, A.; Boden, S. A.; Bagnall, D. M.; Galushko, D.; Bergman, D. J., Solar energy harvesting in the epicuticle of the oriental hornet (*Vespa orientalis*). *Naturwissenschaften* **2010**, *97* (12), 1067-1076.
 20. Jang, J. H.; Ullal, C. K.; Maldovan, M.; Gorishnyy, T.; Kooi, S.; Koh, C.; Thomas, E. L., 3D Micro- and Nanostructures via Interference Lithography. *Adv. Fun. Mat.* **2007**, *17* (16), 3027-3041.
 21. Maldovan, M.; Ullal, C. K.; Jang, J. H.; Thomas, E. L., Sub-micrometer scale periodic porous cellular structures: Microframes prepared by holographic interference lithography. *Adv. Mater.* **2007**, *19* (22), 3809-+.
 22. Jang, J. H.; Ullal, C. K.; Choi, T.; Lemieux, M. C.; Tsukruk, V. V.; Thomas, E. L., 3D Polymer Microframes That Exploit Length-Scale-Dependent Mechanical Behavior. *Adv. Mater.* **2006**, *18* (16), 2123-2127.
 23. Baker, K. M., Highly corrected close-packed microlens arrays and moth-eye structuring on curved surfaces. *Applied Optics* **1999**, *38* (2), 352-356.
 24. Burmeister, F.; Kohn, C.; Kuebler, R.; Kleer, G.; Bläsi, B.; Gombert, A., Applications for TiAlN- and TiO₂-coatings with nanoscale surface topographies. *Surface and Coatings Technology* **2005**, *200* (5-6), 1555-1559.
 25. Nakanishi, T.; Hiraoka, T.; Fujimoto, A.; Saito, S.; Asakawa, K., Nano-patterning using an embedded particle monolayer as an etch mask. *Microelectronic Engineering* **2006**, *83* (4-9), 1503-1508.
 26. Tang, M. L.; Grauer, D. C.; Lassalle-Kaiser, B.; Yachandra, V. K.; Amirav, L.; Long, J. R.; Yano, J.; Alivisatos, A. P., Structural and Electronic Study of an Amorphous MoS₃ Hydrogen-Generation Catalyst on a Quantum-Controlled Photosensitizer. *Angew. Chem. Int. Ed.* **2011**, *50* (43), 10203-10207.

27. Smith, A. J.; Chang, Y.-H.; Raidongia, K.; Chen, T.-Y.; Li, L.-J.; Huang, J., Molybdenum Sulfide Supported on Crumpled Graphene Balls for Electrocatalytic Hydrogen Production. *Adv. Energy Mater.* **2014**, *4* (14).
28. Lin, Y.-C.; Zhang, W.; Huang, J.-K.; Liu, K.-K.; Lee, Y.-H.; Liang, C.-T.; Chu, C.-W.; Li, L.-J., Wafer-scale MoS₂ thin layers prepared by MoO₃ sulfurization. *Nanoscale* **2012**, *4* (20), 6637-6641.
29. Cao, D.; Luo, W.; Feng, J.; Zhao, X.; Li, Z.; Zou, Z., Cathodic shift of onset potential for water oxidation on a Ti⁴⁺ doped Fe₂O₃ photoanode by suppressing the back reaction. *Energy Environ. Sci.* **2014**, *7* (2), 752-759.
30. Zhong, D. K.; Gamelin, D. R., Photoelectrochemical Water Oxidation by Cobalt Catalyst (“Co-Pi”)/ α -Fe₂O₃ Composite Photoanodes: Oxygen Evolution and Resolution of a Kinetic Bottleneck. *J. Am. Chem. Soc.* **2010**, *132* (12), 4202-4207.
31. Zhong, D. K.; Cornuz, M.; Sivula, K.; Gratzel, M.; Gamelin, D. R., Photo-assisted electrodeposition of cobalt-phosphate (Co-Pi) catalyst on hematite photoanodes for solar water oxidation. *Energy Environ. Sci.* **2011**, *4* (5), 1759-1764.
32. Sun, P.; Zhang, W.; Hu, X.; Yuan, L.; Huang, Y., Synthesis of hierarchical MoS₂ and its electrochemical performance as an anode material for lithium-ion batteries. *J. Mater. Chem. A* **2014**, *2* (10), 3498-3504.

Chapter 3. Hierarchical Metal/Semiconductor Nanostructure for Efficient Water Splitting

1. Introduction

The conversion of photon energy into chemical fuel through photoelectrochemical water splitting (PEC) process is of the good clean energy source for the mankind.¹⁻³ Solar water splitting is a method to generate the hydrogen and oxygen by using reaction between photo-electrode, photons and water.⁴⁻⁸ Among the photo-electrode, metal oxide semiconductors such as Fe₂O₃, CuO, ZnO and TiO₂ have been widely elucidated for the photoanode due to their proper flatband potential, high corrosion resistance and low electrical resistance.⁸⁻¹⁵ Although metal oxides have the many advantages for solar water splitting, they have the a large bandgap, lead to the poor light absorbance in the visible light region (400 nm~800 nm) and low performance of PEC. Metal/semiconductor junctions¹⁶⁻¹⁷ shows the many advantages in the PEC such as superior rectification, hot electron generation and photocatalytic property since the metal nanoparticles can improve the visible light absorption by occurring the surface plasmon and providing a Shottky barrier which can reduce the electron-hole recombinations.¹⁸⁻²⁰ For example, Ag or Au deposited semiconductors have exhibit increased performances in charge transfer processes between semiconductor and electrolyte by changes of the Fermi level.²¹

Zinc Oxide (ZnO) is a n-type semiconductor with a large band gap (~3.3eV) and proper conductivity showing superior efficiency in DSSC, organic solar cells and photocatalytic water splitting. The realization of synthesis of different morphologies such as terapods, nanotubes and nanowires also permit to many applications of the ZnO nanostructures. The major limitation for the usage of ZnO as a photoanode for solar water splitting is an its large bandgap, leading to the poor photoexcitation in the visible light region as mentioned before.^{13,23} The surface coating of a photo-absorber having high PEC performance such as CdS and CdSe quantum dots (QD) has been reported to address the poor PEC efficiency limitation of ZnO through the enhancement in the photoreaction to the visible light.²⁴ It has been also reported that plasmon of the metal NPs can enhance the PEC efficiency because of the decreases in recombination of the electron-hole pairs near the surface of the semiconductor.^{14,25}

Surface enhanced Raman scattering (SERS) is a highly sensitive sensor that could be operated by the excitation of the surface plasmon in optical, biological and chemical sensing.²⁶⁻²⁸ To fabricate the highly sensitive SERS substrate, metal nanoparticle suspension²⁹⁻³¹ and rough surfaces³² and periodic metal array³³ have been designed and proposed.

The benefits of periodic patterned arrays compared with disordered scattered NPs and bulk film are related with the fact that the many optical properties of materials that are useful in fields such as biosensors, nano-optics and SERS could be notably affected by the geometries and dimensions of the periodic units.^{18,34-35} Furthermore, periodically patterned nanostructures allow for highly reliable SERS substrates in coverage of large area for applications.³⁶

Interference lithography (IL) is a sophisticated technique to quickly fabricate periodic nano-structures by transferring the laser intensity distribution into a photoresist in large area without defects.^{37,38}

The morphology and geometry of the nanostructures could be controlled via the proper choice of laser components of IL which is a good method to fabricate the sensitive SERS substrate.

In this work, We hypothesize that synergetic effect of plasmon from metal NP and photon trapping effect of periodic semiconductor nanostructures can address the limitation of ZnO with a large band gap for PEC and potentially enhance the performance of solar water splitting. Light trapping in the nanostructure can be increased by appropriate design of geometry and morphology of periodic structures, and the photon absorbance of semiconductors with a large bandgap can be increased by deposition of visible active metal NPs.

2. Experimental Procedures

2.1 Chemicals used

Chloroauric acid (Sigma-Aldrich, >99.9%), sodium citrate (Sigma-Aldrich, >98%), Zinc nitrate hexahydrate (Sigma-Aldrich, >98%), Hexamethylenetetramine (HMTA) (Sigma-Aldrich, >98%), Sodium hydroxide (Duksan pure chemical ls) Ethanol. All chemicals were used without further purification.

2.2 Fabrication of 2D patterns via interference lithography

The substrates were cleaned using ultra-sonication with acetone, isopropanol and de-ionized water for 10 min respectively and dried by nitrogen blowing. A 200 nm of ZnO seed layer is sputtered onto the substrate. A 100nm thickness of photoresist film was obtained by spin coating at 3000rpm on the ZnO sputtered substrate. The 2D square patterns with circular holes were fabricated via interference lithography. The exposure time was 6 x 6s. Before developing the photoresist using PGMEA, post-exposure bake was done at 55 °C for 10min. The diameter and pitch of patterns were found to be 380 nm and 550 nm, respectively from SEM measurements.

2.3 ZnO NWs growth via hydrothermal method

The ZnO NWs growth was carried out by suspending the wafer upside-down in a glass bottle filled with an aqueous solution of zinc nitrate hydrate (25 mM) and hexamethylenetetramine (25 mM) at 90°C for 2 hr 30 min. After the reaction, substrate was removed from the growth solution, rinsed with ethanol

and deionized water, and dried. 30 mM of chloroauric acid was dissolved in ethanol to which 1% wt of sodium citrate dissolved in water was added. The mixture was heated to 100°C for 30 min and then allowed to cool down naturally along with substrate. The pH of the prepared solution was adjusted to be 8~9 using 1M NaOH solution before deposition. The samples were washed with D. I. water and ethanol.

2.4 Characterization

The structure of the ZnO NWs was taken using NOVA NANOSEM 230 FESEM. The powder diffraction data was obtained using Rigaku D/MAZX 2500V/PC HPXRD. The SERS spectrums were obtained by using alpha 300S spectrograph from WITEC. The instrument uses an Olympus BX-40 microscope with a 100 X (0.9 N.A) objective with a power of 0.1 mW of the 632.8 nm line from an electrically cooled He-Ne laser. The laser spot size in these studies was approximately 429 nm. In this work, all sample integration time for single measurement was set to 20 s.

2.5 EF calculations

The enhancement factor was calculated using the following formula:

$$EF = \frac{I_{SERS}}{I_{bulk}} \frac{N_{bulk}}{N_{SERS}},$$

where I and N correspond to the intensity of the Raman band and number of molecules being probed, respectively, and the subscript refers to the SERS and bulk cases. I_{bulk} and N_{bulk} were estimated from the Raman spectra of 1×10^{-7} M of crystal violet solution. N_{bulk} was calculated to be 2.9×10^5 . The N_{SERS} was calculated to be 7.3×10^{10} molecules. The number of gold NPs adsorbed on the ZnO NW and subsequently the number of crystal violet molecules was calculated based on a laser spot size of 1 μ m and a focal depth of 34.6 μ m. The enhancement factors were calculated to be 4.75×10^7 for p-Au NPs/ZnO NWs and 1.5×10^8 for Au NPs/ZnO NWs.

2.6 Photo electrochemical (PEC) Measurement

The PEC measurements were done using Ag/AgCl, Pt wire, and Au NPs/ZnO NWs/FTO as a reference electrode, as a counter electrode, and as a working electrode, respectively, in 0.5 M of Na₂SO₄ (pH = 6.8) electrolyte solution. Newport solar simulator (M-91190A) was used to illuminate the sunlight at AM 1.5 condition. Enhanced aluminum mirror (edmundoptics) was used to reflect the light onto the sample. The power of the solar simulator was measured to be 80 mW/cm². The electrochemical data

was measured using Princeton Applied research VersaSTAT3 potentiostat. Linear sweep voltammograms were obtained from -0.5V to 1.1 V range with a scan rate of 10 mV/S under the illumination of AM 1.5 except for dark sample. Chronoamperometry measurements were measured at +0.5V while the simulator was switched on and off every 10 seconds manually using the shutter to record the increase in photocurrent. The PEC performances of ZnO NWs solely in the visible range were acquired by the solar simulator coupled with the UV cutoff filter ($\lambda > 420$ nm). The transmittance of the light passing through the filter was given in fig S5.

3. Results and Discussion

In this work, we reported a hierarchical hybrid metal/semiconductor nanostructure fabricated by greatly reproducible polymer Su-8 templates synthesized through IL as a superior candidate for a water splitting cell with a broad absorption band in visible light for PEC as well as a very sensitive SERS substrate.

The photoanode composed of ZnO nanowires (ZnO NWs) and gold nanoparticles (Au NPs) were fabricated by using hydrothermal growth and solution coating method, respectively. The periodic patterned ZnO NWs were synthesized by using hydrothermal growth of ZnO NWs in the holes of SU-8 polymeric templates. The hierarchically patterned Au NPs/ZnO NWs (hp-Au NPs/ZnO NWs) exhibit increased photon absorbance in the UV-visible region, resulting in both higher SERS signal and better efficiency in the PEC than those of the un-patterned Au NPs decorated ZnO NWs (Au NPs/ZnO NWs).

The enhanced PEC performance of the hierarchical Au/ZnO NWs structures is attributed to the increased plasmon-induced electron transfer because of the enhanced scattering of the absorption of photon via the synergetic effect of the two types of geometries. The superior performance of the hierarchical Au/ZnO NW nanostructures as the photoanodes for PEC demonstrate that appropriate proposed metal/semiconductor heterojunctions has the great potential for solar-energy related materials.

The four process steps for hp-Au NPs/ZnO NWs nanostructures have shown in **Figure 1**. First, a 200 nm height of ZnO seed layer was coated onto the prepared FTO glass using a RF-sputtering. The ZnO seed layer was confirmed to be crystalline and [110] direction, which is optimized condition for the epitaxial growth of ZnO NWs via XRD measurement (displayed in the supporting information). The periodic Su-8 polymer templates with 300nm holes and 500nm pitch size were synthesized on the ZnO seed layer coated FTO glass through IL via double exposure of He-Cd laser beam with double exposure of substrate by rotating 90°. Second, ZnO nanowires were synthesized in circular holes of periodically patterned SU-8 template using the hydrothermal growth method. The reaction time and density of the precursors were decided to generate a proper diameter and height for nanowires in holes of 2D lattices. Third, the Au NP was decorated onto ZnO NWs using a solution-based technique, and the inter particle distances between the Au NPs were varied by the density of the precursor solution.

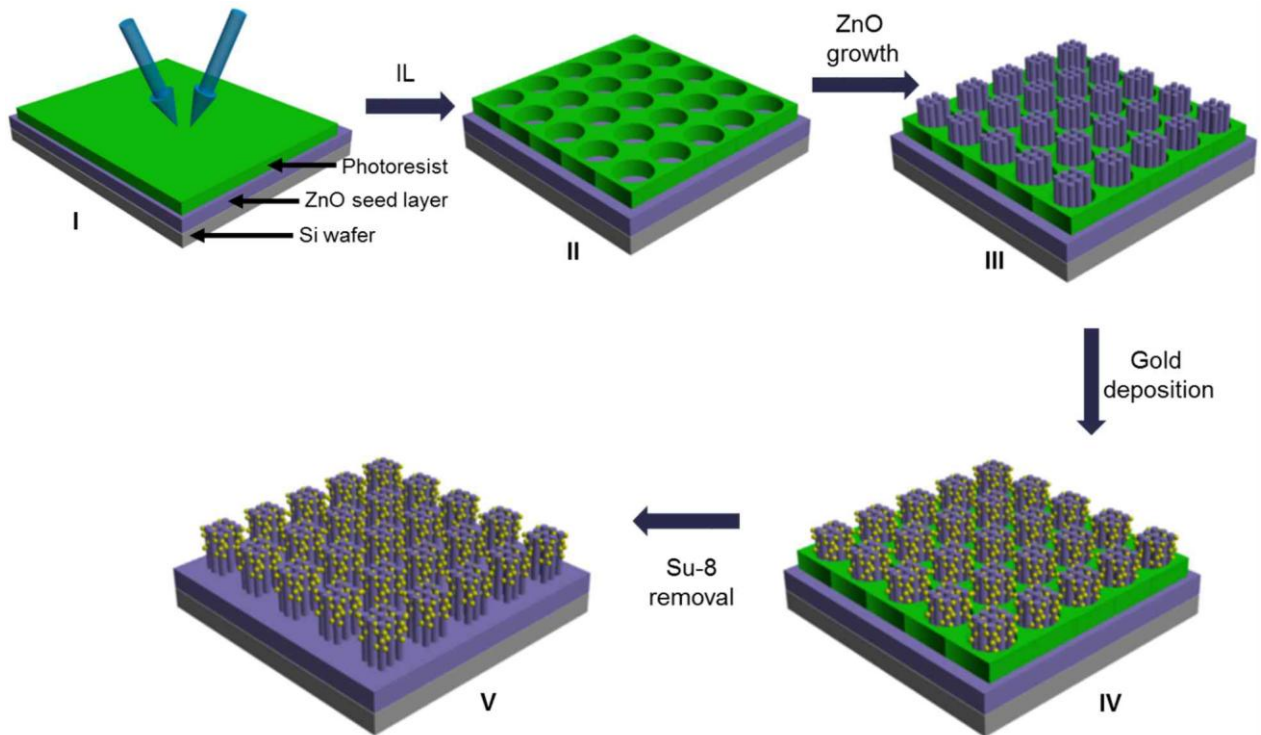


Figure 1. Schemes shows the fabrication process of the surface deposited hierarchical SERS substrate. (I) Double exposure through interference lithography (IL). The blue arrows display the direction of the laser beams. (II) IL template synthesized on the ZnO seed layer. (III) ZnO NWs grown in the circular holes of the 2-D square lattice. (IV) Hierarchical Au NPs coated ZnO NWs (Au NPs/ZnO NWs) in SU-8 templates. (V) Hierarchical Au NPs/ZnO NWs.

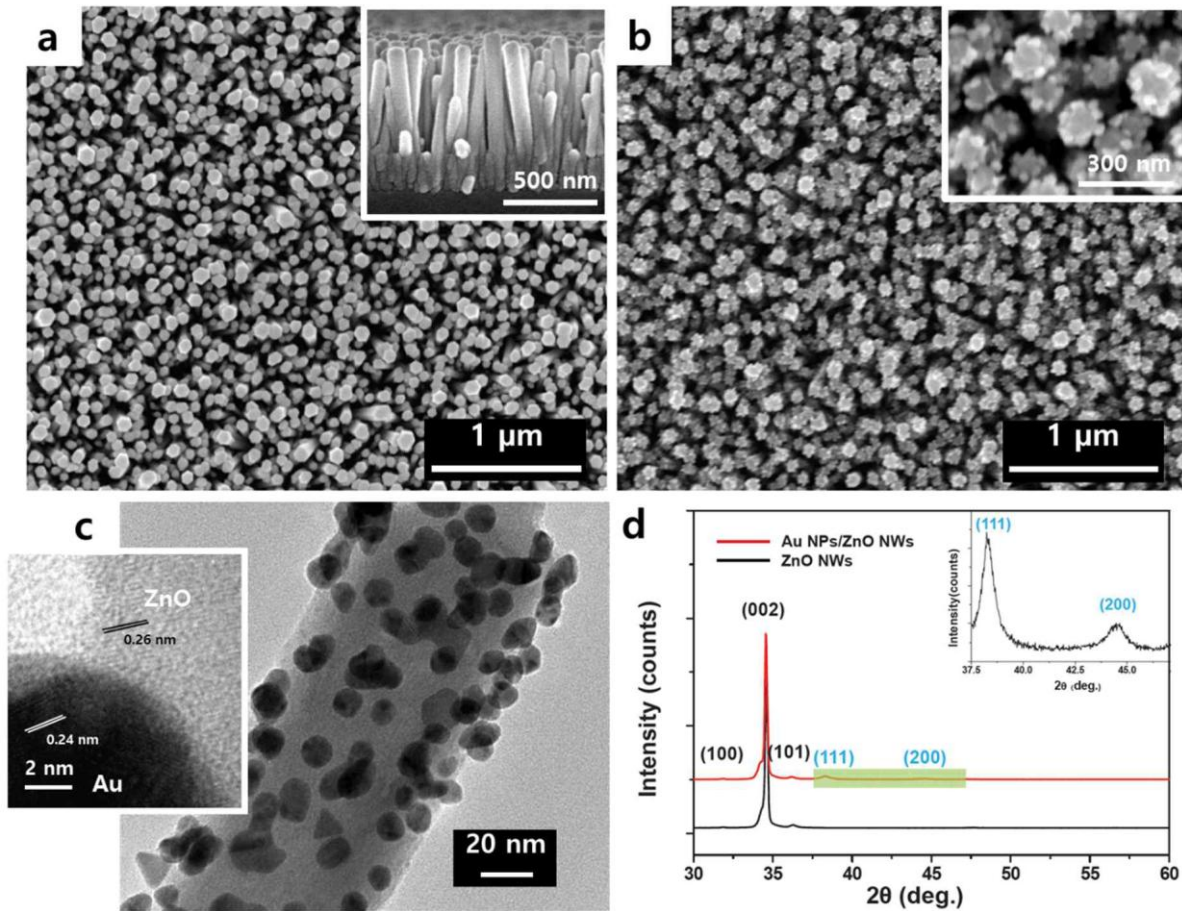


Figure 2. SEM, TEM and XRD of ZnO NWs and Au NPs/ZnO NWs: (a) SEM images of ZnO NWs growth on FTO glass and (b) Top-view SEM of Au NPs/ZnO NWs. The insets in (a) and (b) are cross sectional images of the ZnO NWs and a macro image of the Au NPs/ZnO NWs, respectively. (c) TEM image of the gold coated ZnO NWs. The inset is the closed-up image of the Au NP/ZnO NW. (d) XRD of ZnO NWs before (lower) and after (upper) Au deposition. The inset is a magnified image of rectangular area of the Au NPs/ZnO NWs.

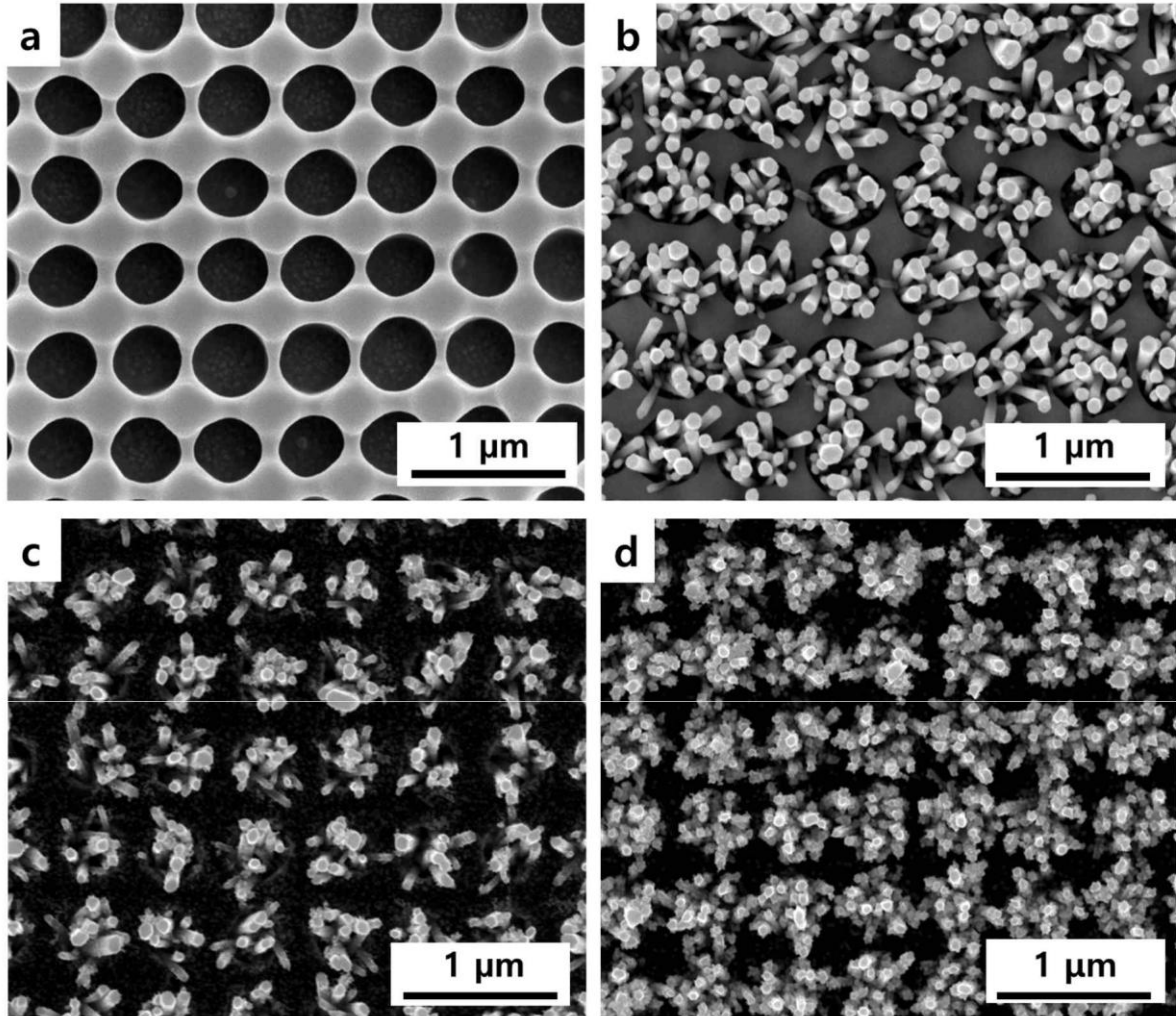


Figure 3. SEM images of (a) Su-8 polymer template, (b) Su-8/ZnO NW substrate, (c) patterned ZnO NW and (d) hp Au/ZnO nanostructures.

Finally, the periodic SU-8 patterns were got rid of using an oxygen plasma condition. The plain (non-patterned) Au NPs/ZnO NWs were prepared using the same procedures as that used for the periodic patterned structure without fabrication of the SU-8 patterning and oxygen plasma treatment.

Figure 2 shows the results of the characterization of the ZnO NWs and Au NP decorated ZnO nanowires. The height and diameter of the nanowires were 550-750 nm and 65-95 nm, respectively, as displayed in Figure 2 a. The cross sectional view of the ZnO nanowires in the inset exhibits that as-grown ZnO nanowires with a smooth surfaces and uniform holes could be taken vertically. The TEM and SEM images of the Au nanoparticle decorated ZnO nanowires (Au NPs/ZnO NWs) are shown in Figures 2b and c. The surfaces of the ZnO nanowires are decorated with gold nanoparticles with high reproducibility as shown in the Figure 2c. The radius of the gold nanoparticle tightly attached to the wall of ZnO NWs was determined to be approximately 6 nm from TEM images. The inset image is the high-resolution TEM image exhibiting gold nanoparticles and ZnO nanowire with the lattice constant of 0.24 nm and 0.26 nm, respectively. The XRD data of the ZnO NWs and Au NPs/ZnO are included in Figure 2 d. The peak at near 35° corresponding to (002) plane and two small peaks corresponding to the (101) and (100) planes mean a strong crystalline of as-grown ZnO nanowires. The peaks for the Au NPs/ZnO NWs depicts that there are the further small peaks at $2\theta=44.46^\circ$ and 38.24° , corresponding to the (200) and (111) plane of the gold-metal, respectively, demonstrating the deposition and polycrystalline property of Au NPs. The inset image of the Figure 2d in the spectra of Au NPs/ZnO NWs was illustrated because of the slightly small content of gold nanoparticles, and a then a low peak intensity, compared with the measured peaks of the ZnO NWs. The SEM images of the morphologies at each step of the making proceed for the hp-Au NPs/ZnO NWs are shown in **Figure 3**. The Su-8 polymeric template designed this work is a original two-dimensional (2-D) periodic holes array synthesized through IL. As shown in Figure 3a, the period length and diameter of the Su-8 polymeric template in the circular hole arrays were 550 nm and 380 nm, respectively. The dimensions of the SU-8 polymeric lattice were proposed so as to maximize the photon trapping property caused by the increased scattering in the morphologies with a radius similar to the wavelength of the visible light and to secure large space to grow the almost 15 ZnO NWs for the decoration of many Au NPs.³⁹ Further improvement of the periodicity of the patterns trigger the SERS effect to be reduced and results in poor absorption. The SEM image of the ZnO nanowires synthesized in the periodic SU-8 template is shown in Figure 3 b. Commonly, the efficiency of PEC can be enhanced by improving the length of the nanowires.⁹ But synthesis of longer ZnO nanowires in the vacant holes of the SU-8 template with a specific thickness often resulted in the generation of tilted ZnO nanowires. The longer ZnO nanowires grown in adjacent Su-8 holes that are almost connected and then reducing the property of pattern nature as shown in Figure S7.

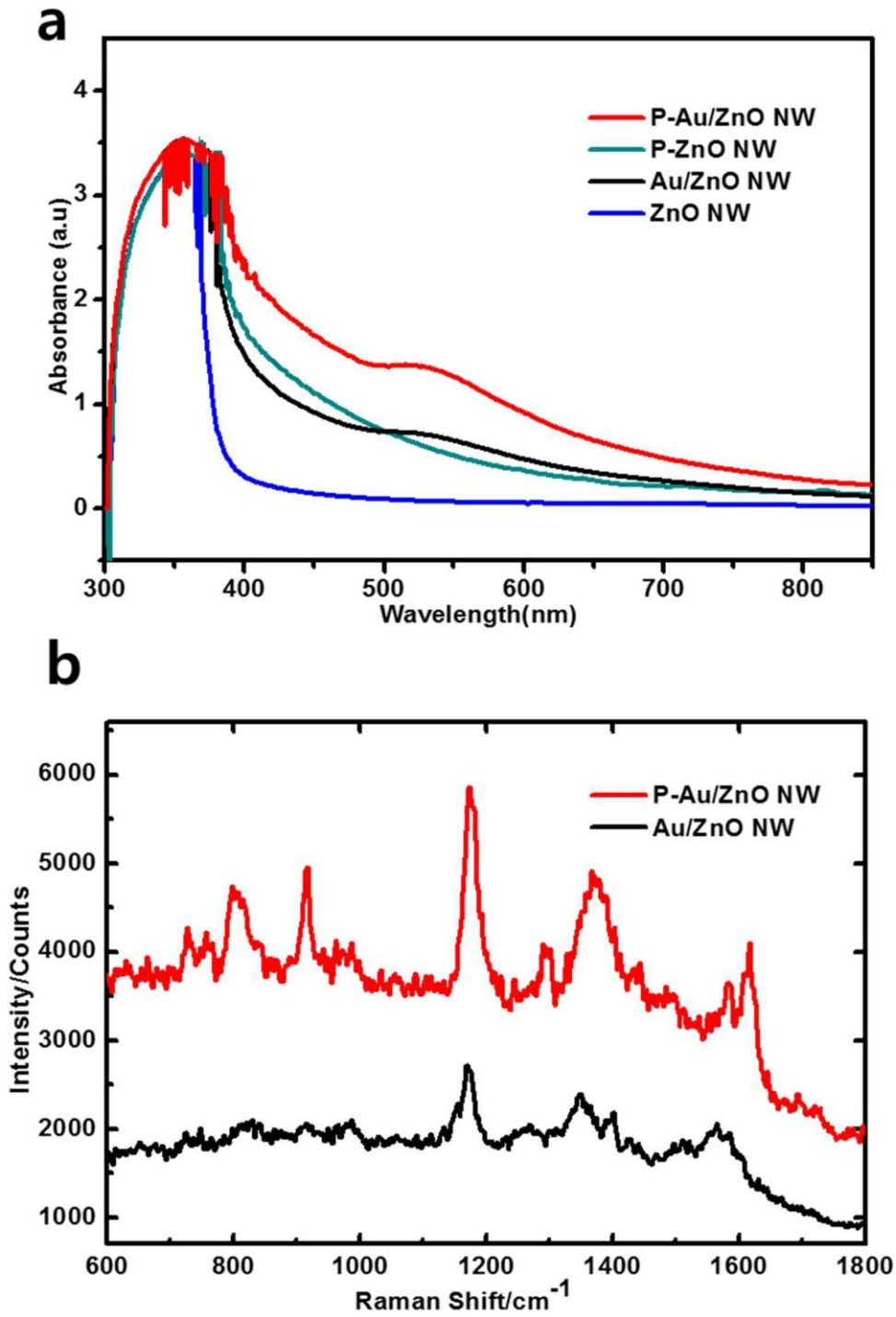


Figure 4. (a) Absorbance of the P-Au/ZnO NW, P-ZnO NW, Au/ZnONW and ZnO. (b) Raman data of the P-Au/ZnO NW and Au/ZnO NW with crystal violet.

This may be addressed by additional optimization of the synthesis step such as by hydrothermal growth of ZnO nanowires through an epitaxial growth or by using a high aspect ratio periodic SU-8 template. The gold NPs coating on the ZnO NWs were conducted on polymeric template as a mask such that gold nanoparticles would only be deposited on the surface of ZnO NWs as displayed in Figure 3 c. The morphologies of the Au NPs/ZnO nanowires taken from the removal of the polymer template were shown in Figure 3 d, offering obvious proof of the uniformly decorated gold nanoparticles over a large area. The structures obtained in this work are periodic hierarchical pattern nanostructures consisted of cluster of almost 15 ZnO nanowires with diameters of 55 to 95 nm and leng of 550 to 650nm, uniformly decorated with approximately 13nm of Au nanoparticles with an inter-particle distance of about 14nm, in the periodic pattern with circular holes of 190 nm in radius.

The UV-vis spectra was measured so as to elucidate the optical property of the ZnO nanowires. The UV-Vis absorption spectroscopy of the non-patterned and hp-ZnO nanowires, and the non-patterned and hp-Au NPs/ZnO NWs synthesized on the FTO glass obtained at vertical irradiation as shown in Figure 4a. The shoulder band peak at 527 nm in the latter 2 spectra are the property of plasmon absorbance of the Au nanoparticles on the ZnO nanowires and are slightly shifted toward red color compared to those of Pure gold nanoparticles (520 nm). The absorbance peak from 300 to 400 nm was corresponding to the bandgap energy of the ZnO nanowires. Importantly, the periodic hierarchical pattern samples including hp-ZnO NWs and hp-Au NPs/ZnO NWs) exhibited more wider and intense spectra with a broad absorbance from 400 to 800 nm than that of non-patterned samples. Although the numbers of both gold nanoparticles and ZnO nanowires in periodic hierarchical pattern sample are lower than those of the densely packed non-patterned samples. The increased UV absorption of the periodic hierarchical pattern sample can be ascribed to the mixing scattering effect taken by the coupling of different size in the hierarchical pattern. Generally, the intensity of scattering can be controlled by light incident angle, polarization and a relation of the ratio of the particle diameter to the wavelength of light.⁴⁰ For example, working electrode composed of 25 nm of nanocrystalline TiO₂ (nc-TiO₂) with lager TiO₂ particles was exhibited increased photocurrent density in Dye sensitized solar cell.⁴¹

Compared with the single layer of the nc-TiO₂ where the light was weakly scattered, the double layers assembled with larger particles and thus with longer effective light path lengths can have much greater light trapping effect via multiple scattering, i.e. Mie scattering where electromagnetic radiation is scattered by a particle with the size of diameter-to-wavelength ratio approaching 1. Therefore, combination of two dimensions in periodic hierarchical morphology (380 nm of circular holes and 12 nm of NPs) can maximize the light trapping, resulting in a strong and broad absorbance band in the visible light region (400 nm – 800nm) in a similar way. Upon this result, the spectra of SERS measured from 1×10^{-7} M of crystal violet (CV) solution on the hp-Au NPs/ZnO NWs with the excitation at 633 nm is compared with that of the plain Au NPs/ZnO NWs (Figure 4 b). The SERS results exhibited great

improvement in the hp-Au NPs/ ZnO NWs, which is well matched with the absorbance spectroscopy in Figure 4 a. The enhancement factor (EF) surveyed for hp-Au NPs/ ZnO NWs was 1.5×10^8 as calculated in the supporting information.

The higher SERS EF of the periodic hierarchical structures than that non-patterned structure is attributed to the favorable absorbance of the plasmon resonances of gold nanoparticles enhanced by the increased photon wave surrounding them because of the bigger dimensions of patterned ZnO NWs (380nm in diameter). Furthermore, the inter particle distance between the Au NPs in the periodic hierarchical structure is 10-15nm, which is satisfied to take a localized hot spot via the increased collective oscillation by the adjacent nanoparticles.

In this situation, the bundle of Au NPs in a single unit cell of the large scale pattern could be considered as cluster with the combined plasmonic effects of many small NPs. Hence, the combination of two different dimensional size in the hierarchical structures can maximize the absorbance of the surface plasmons by balancing the promoted dipolar plasmon resonance and increased photon trapping.

The performance of PEC was obtained using closed circuit composed of Au NPs/ZnO NWs, Pt mesh and Ag/AgCl as a photoanode, a counter electrode and a reference electrode, in 0.5M of Na₂SO₄ (pH=6.8) electrolyte solution, and the photoresponses are included in **Figure 5**. The surface plasmon enhanced PEC mechanism of Au NPs/ZnO nanowires is illustrated in Figure 5 a and c. After the plasmon generated electrons are moved from gold nanoparticles to ZnO nanowires, the oxygen evolution reaction was occurred at the surface of oxidized Au NPs or of the ZnO semiconductor. The photoexcited electrons from Au NPs and ZnO Nws are flowed and collected at counter electrode where the hydrogen gas is generated by the reducing H⁺ ions, while the photoexcited holes can be extracted to the interface of ZnO NW/electrolyte and reacted with the OH⁻ ions to generate the oxygen gas. The current-voltage curve of ZnO NWs and Au NPs/ZnO nanowires under 1sun condition is shown in Figure 5 a. The UV cutoff filter ($\lambda > 420$ nm) was used so as to elucidate the PEC performance of ZnO NWs solely in the visible light. The photocurrent density of Au NPs/ZnO nanowires shows the approximately 3.5times higher than that of the ZnO NWs at 0.5 V indicating that Au NPs can effectively absorb the visible light by the resonance of surface plasmon. Furthermore, the hp-Au NPs/ZnO nanowires display more enhanced photocurrent than non-patterned Au NPs/ZnO NWs against all voltage regions. This is attributed to electrons generated by more highly localized surface plasmon are easily extracted to surface of ZnO NWs without a recombination.¹⁹ Thus, the enhanced PEC performance becomes higher when increased by plasmonic gold nanoparticles with a higher excitation.

The stability of the PEC performance of the hp-Au NPs/ZnO NWs photoanode after 30 on/off illumination cycles was confirmed in Figure 5 b.

When solar light including UV and Visible region were shined without UV cutoff filter, the PEC performance of ZnO nanowires was enhanced by a factor of ~30 because the additional direct excitation

of electrons in ZnO nanowires by increased UV light absorbance. The photocurrent density of hp-Au NPs/ZnO NWs and Au NPs/ZnO NWs was 4.2 and 1.8 times higher than that of ZnO NWs at 0.5 V, respectively. This result can further support the water splitting mechanism of ZnO NWs based on surface plasmon excitation and the efficient photon trapping effect. The photoresponses over time (I-t curve) of the samples were measured at + 0.5 V with chopped illumination of AM 1.5 at a rate of 10 s exposure followed by 10 s nonillumination, as shown in Figure 5 d. The sharp spike/dip shape in the I-t curve during the on/off irradiation cycles imply the fast transfer of photoexcited electrons in ZnO NWs. Overall, photocurrent and the rate of the solar water splitting in the hp-Au NPs/ZnO NWs are more prominent because of the increased photon trapping effect, which also can explain the contribution of electric field enhancement of surface plasmon to the photocatalytic conversion reaction. This study conclusively exhibited a correspondence between the SERS property and the performance of PEC reaction proceeding by hot electron transfer and other possible charge transfer mechanism between Au NPs and ZnO NWs.

4. Conclusion

In conclusion, by combining Au NPs with ZnO NWs, we have fabricated hierarchical metal/semiconductor nanostructures with excellent performance for surface plasmon enhanced water splitting under visible light illumination. We also experimentally demonstrated a positive relationship between SERS properties and the rate of plasmon enhanced photocatalytic water splitting by the comparison of plain Au NPs/ZnO NWs with hierarchically patterned Au NPs/ZnO NWs. The improved absorbance and enhanced photoconversion efficiency of hierarchically patterned Au NPs/ZnO NWs are obtained as a result of the maximized scattering effect, by the coupling of the large scale period of the nanostructure into the small scale of the NW diameter. Interference lithography-base fabrication of hierarchical Au NP/ZnO NWs enables the straightforward integration of multiple dimensions of nanostructures with a large coverage area and high reproducibility. The excellent performance of the hierarchical Au/ZnO nanostructures enables greater potential for semiconductor/metal hybrid structures for application in energy-related materials and photocatalysts with high electron collections.

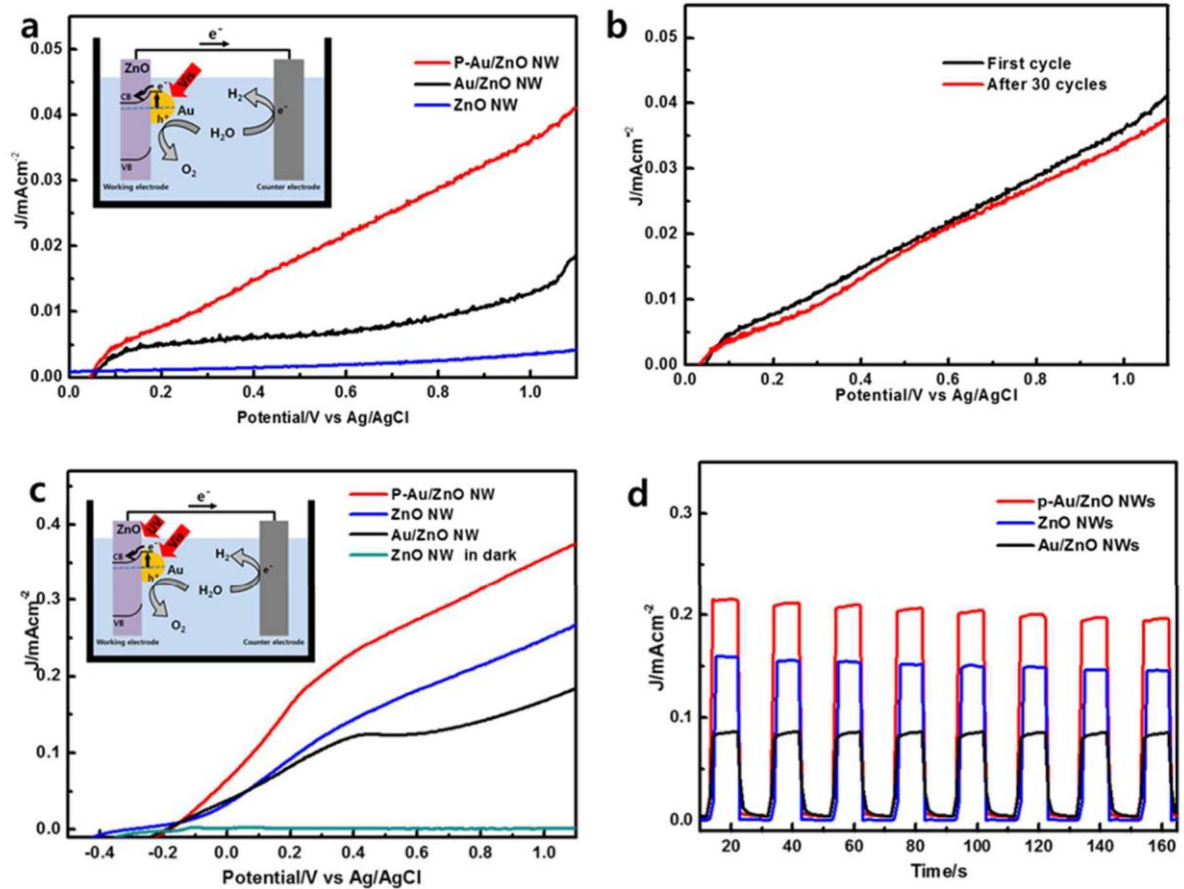


Figure 5. (a) I-V curve of the hp-Au NPs/ZnO NWs, Au/ZnO ZnONw and ZnO with optical filter. (b) I-V curve of hp-Au NPs/ZnO NWs after 30cycles working. (c) I-V curves under both UV and visible illumination. (d) I-t curves of the samples with light-chopping conditions. The insets in a and c are illustrations showing the PEC mechanism of the ZnO NWs photoanodes.

5. REFERENCES

1. Banholzer, M. J.; Millstone, J. E.; Qin, L.; Mirkin, C. A., Rationally designed nanostructures for surface-enhanced Raman spectroscopy. *Chem. Soc. Rev.* 2008, 37 (5), 885-897.
2. Bendall, J. S.; Etgar, L.; Tan, S. C.; Cai, N.; Wang, P.; Zakeeruddin, S. M.; Graetzel, M.; Welland, M. E., An efficient DSSC based on ZnO nanowire photo-anodes and a new D-pi-A organic dye. *Energy Environ. Sci.* 2011, 4 (8), 2903-2908.
3. Chen, H. M.; Chen, C. K.; Chang, Y.-C.; Tsai, C.-W.; Liu, R.-S.; Hu, S.-F.; Chang, W.-S.; Chen, K.-H., Quantum Dot Monolayer Sensitized ZnO Nanowire-Array Photoelectrodes: True Efficiency for Water Splitting. *Angew. Chem. Int. Ed.* 2010, 49 (34), 5966-5969.
4. Chen, Z. H.; Tang, Y. B.; Liu, C. P.; Leung, Y. H.; Yuan, G. D.; Chen, L. M.; Wang, Y. Q.; Bello, I.; Zapien, J. A.; Zhang, W. J.; Lee, C. S.; Lee, S. T., Vertically Aligned ZnO Nanorod Arrays Sensitized with Gold Nanoparticles for Schottky Barrier Photovoltaic Cells. *J. Phys. Chem. C* 2009, 113 (30), 13433-13437.
5. Fan, P.; Chettiar, U. K.; Cao, L.; Afshinmanesh, F.; Engheta, N.; Brongersma, M. L., An invisible metal-semiconductor photodetector. *Nature Photon.* 2012, 6 (6), 380-385.
6. Fang, Z.; Zhen, Y.-R.; Fan, L.; Zhu, X.; Nordlander, P., Tunable wide-angle plasmonic perfect absorber at visible frequencies. *Phys. Rev. B* 2012, 85 (24).
7. Freeman, R. G.; Grabar, K. C.; Allison, K. J.; Bright, R. M.; Davis, J. A.; Guthrie, A. P.; Hommer, M. B.; Jackson, M. A.; Smith, P. C.; Walter, D. G.; Natan, M. J., SELF-ASSEMBLED METAL COLLOID MONOLAYERS - AN APPROACH TO SERS SUBSTRATES. *Science* 1995, 267 (5204), 1629-1632.
8. Fujishima, A.; Honda, K., ELECTROCHEMICAL PHOTOLYSIS OF WATER AT A SEMICONDUCTOR ELECTRODE. *Nature* 1972, 238 (5358), 37-+.
9. Hoang, S.; Guo, S.; Hahn, N. T.; Bard, A. J.; Mullins, C. B., Visible Light Driven Photoelectrochemical Water Oxidation on Nitrogen-Modified TiO₂ Nanowires. *Nano Lett.* 2012, 12 (1), 26-32.
10. Hwang, Y. J.; Hahn, C.; Liu, B.; Yang, P., Photoelectrochemical Properties of TiO₂ Nanowire Arrays: A Study of the Dependence on Length and Atomic Layer Deposition Coating. *Acs Nano* 2012, 6 (6), 5060-5069.
11. Ingram, D. B.; Linic, S., Water Splitting on Composite Plasmonic-Metal/Semiconductor Photoelectrodes: Evidence for Selective Plasmon-Induced Formation of Charge Carriers near the Semiconductor Surface. *J. Am. Chem. Soc.* 2011, 133 (14), 5202-5205.
12. Jang, J.-H.; Ullal, C. K.; Choi, T.; Lemieux, M. C.; Tsukruk, V. V.; Thomas, E. L., 3D polymer microframes that exploit length-scale-dependent mechanical behavior. *Adv. Mater.* 2006, 18 (16), 2123-+.

13. Jang, J.-H.; Ullal, C. K.; Maldovan, M.; Gorishnyy, T.; Kooi, S.; Koh, C.; Thomas, E. L., 3D micro- and nanostructures via interference lithography. *Adv. Funct. Mater.* 2007, 17 (16), 3027-3041.
14. Jing, L.; Zhou, J.; Durrant, J. R.; Tang, J.; Liu, D.; Fu, H., Dynamics of photogenerated charges in the phosphate modified TiO₂ and the enhanced activity for photoelectrochemical water splitting. *Energy. Environ. Sci.* 2012, 5 (4), 6552-6558.
15. Knight, M. W.; Sobhani, H.; Nordlander, P.; Halas, N. J., Photodetection with Active Optical Antennas. *Science* 2011, 332 (6030), 702-704.
16. Koo, H.-J.; Kim, Y. J.; Lee, Y. H.; Lee, W. I.; Kim, K.; Park, N.-G., Nano-embossed hollow spherical TiO₂ as bifunctional material for high-efficiency dye-sensitized solar cells. *Adv. Mater.* 2008, 20 (1), 195-201.
17. Linic, S.; Christopher, P.; Ingram, D. B., Plasmonic-metal nanostructures for efficient conversion of solar to chemical energy. *Nat. Mater.* 2011, 10 (12), 911-921.
18. Liu, Z.; Hou, W.; Pavaskar, P.; Aykol, M.; Cronin, S. B., Plasmon Resonant Enhancement of Photocatalytic Water Splitting Under Visible Illumination. *Nano Lett.* 2011, 11 (3), 1111-1116.
19. Lunz, M.; Gerard, V. A.; Gun'ko, Y. K.; Lesnyak, V.; Gaponik, N.; Susha, A. S.; Rogach, A. L.; Bradley, A. L., Surface Plasmon Enhanced Energy Transfer between Donor and Acceptor CdTe Nanocrystal Quantum Dot Monolayers. *Nano Lett.* 2011, 11 (8), 3341-3345.
20. Mayer, K. M.; Lee, S.; Liao, H.; Rostro, B. C.; Fuentes, A.; Scully, P. T.; Nehl, C. L.; Hafner, J. H., A label-free immunoassay based upon localized surface plasmon resonance of gold nanorods. *Acc Nano* 2008, 2 (4), 687-692.
21. Nehl, C. L.; Liao, H. W.; Hafner, J. H., Optical properties of star-shaped gold nanoparticles. *Nano Lett.* 2006, 6 (4), 683-688.
22. Odom, T. W.; Gao, H.; McMahon, J. M.; Henzie, J.; Schatz, G. C., Plasmonic superlattices: Hierarchical subwavelength hole arrays. *Chem. Phys. Lett.* 2009, 483 (4-6), 187-192.
23. Park, J. H.; Kim, S.; Bard, A. J., Novel carbon-doped TiO₂ nanotube arrays with high aspect ratios for efficient solar water splitting. *Nano Lett.* 2006, 6 (1), 24-28.
24. Qiu, Y.; Yan, K.; Deng, H.; Yang, S., Secondary Branching and Nitrogen Doping of ZnO Nanotetrapods: Building a Highly Active Network for Photoelectrochemical Water Splitting. *Nano Lett.* 2012, 12 (1), 407-413.
25. Schuller, J. A.; Barnard, E. S.; Cai, W.; Jun, Y. C.; White, J. S.; Brongersma, M. L., Plasmonics for extreme light concentration and manipulation. *Nat. Mater.* 2010, 9 (3), 193-204.
26. Singh, W. M.; Pegram, D.; Duan, H.; Kalita, D.; Simone, P.; Emmert, G. L.; Zhao, X., Hydrogen Production Coupled to Hydrocarbon Oxygenation from Photocatalytic Water Splitting. *Angew. Chem. Int. Ed.* 2012, 51 (7), 1653-1656.
27. Stoerzinger, K. A.; Lin, J. Y.; Odom, T. W., Nanoparticle SERS substrates with 3D Raman-active

- volumes. *Chem. Sci.* 2011, 2 (8), 1435-1439.
28. Thomann, I.; Pinaud, B. A.; Chen, Z.; Clemens, B. M.; Jaramillo, T. F.; Brongersma, M. L., Plasmon Enhanced Solar-to-Fuel Energy Conversion. *Nano Lett.* 2011, 11 (8), 3440-3446.
 29. Tong, L.; Zhu, T.; Liu, Z., Approaching the electromagnetic mechanism of surface-enhanced Raman scattering: from self-assembled arrays to individual gold nanoparticles. *Chem. Soc. Rev.* 2011, 40 (3), 1296-1304.
 30. Townsend, T. K.; Browning, N. D.; Osterloh, F. E., Nanoscale Strontium Titanate Photocatalysts for Overall Water Splitting. *ACS Nano* 2012, 6 (8), 7420-7426.
 31. Vaneski, A.; Susha, A. S.; Rodriguez-Fernandez, J.; Berr, M.; Jaeckel, F.; Feldmann, J.; Rogach, A. L., Hybrid Colloidal Heterostructures of Anisotropic Semiconductor Nanocrystals Decorated with Noble Metals: Synthesis and Function. *Adv. Funct. Mater.* 2011, 21 (9), 1547-1556.
 32. Vasudev, A. P.; Schuller, J. A.; Brongersma, M. L., Nanophotonic light trapping with patterned transparent conductive oxides. *Opt. Express* 2012, 20 (10), A385-A394.
 33. Waller, M. R.; Townsend, T. K.; Zhao, J.; Sabio, E. M.; Chamousis, R. L.; Browning, N. D.; Osterloh, F. E., Single-Crystal Tungsten Oxide Nanosheets: Photochemical Water Oxidation in the Quantum Confinement Regime. *Chem. Mater.* 2012, 24 (4), 698-704.
 34. Walsh, D.; Kim, Y.-Y.; Miyamoto, A.; Meldrum, F. C., Synthesis of Macroporous Calcium Carbonate/Magnetite Nanocomposites and their Application in Photocatalytic Water Splitting. *Small* 2011, 7 (15), 2168-2172.
 35. Walter, M. G.; Warren, E. L.; McKone, J. R.; Boettcher, S. W.; Mi, Q.; Santori, E. A.; Lewis, N. S., Solar Water Splitting Cells. *Chem. Rev.* 2010, 110 (11), 6446-6473.
 36. Wang, H.; Halas, N. J., Mesoscopic Au "Meatball" particles. *Adv. Mater.* 2008, 20 (4), 820-+.
 37. Warren, S. C.; Thimsen, E., Plasmonic solar water splitting. *Energy. Environ. Sci.* 2012, 5 (1), 5133-5146.
 38. Wei, Y.; Wu, W.; Guo, R.; Yuan, D.; Das, S.; Wang, Z. L., Wafer-Scale High-Throughput Ordered Growth of Vertically Aligned ZnO Nanowire Arrays. *Nano Lett.* 2010, 10 (9), 3414-3419.
 39. Willner, I.; Eichen, Y.; Frank, A. J., TAILORED SEMICONDUCTOR RECEPTOR COLLOIDS - IMPROVED PHOTOSENSITIZED H₂ EVOLUTION FROM WATER WITH TiO₂-BETA-CYCLODEXTRIN COLLOIDS. *J. Am. Chem. Soc.* 1989, 111 (5), 1884-1886.
 40. Yang, X.; Wolcott, A.; Wang, G.; Sobo, A.; Fitzmorris, R. C.; Qian, F.; Zhang, J. Z.; Li, Y., Nitrogen-Doped ZnO Nanowire Arrays for Photoelectrochemical Water Splitting. *Nano Lett.* 2009, 9 (6), 2331-2336.
 41. Zhang, L.; Baumanis, C.; Robben, L.; Kandiel, T.; Bahnemann, D., Bi₂WO₆ Inverse Opals: Facile Fabrication and Efficient Visible-Light-Driven Photocatalytic and Photoelectrochemical Water-Splitting Activity. *Small* 2011, 7 (19), 2714-2720.

Chapter 4. An optimal substrate design for SERS: dual-scale diamond-shaped gold nanostructures fabricated via interference lithography

1. Introduction

The fabrication of metal nanostructures such as periodic arrays, plate or nanoparticles has received great attention due to its superior optical properties such as scattering and plasmonic effect for the biomaterials, optical devices and nano electronic.¹⁻⁵ Surface enhanced Raman scattering (SERS), which apply the localized surface plasmons by an electromagnetic wave in metal nanostructures, is one of the very strong sensing method, allowing for real time, non-destructive, and very sensitive measurement for detection of organic-inorganic species and biomolecules.⁶⁻¹¹ The very weak Raman signals which comes from even single molecule detection can be increased up to 10^{13} to 10^{17} times at “hot spots” by controlling the morphology for increase of the electric field.¹² The control of the inter particle distance and structure and morphology of the metal nanoparticle in the nanometer scale i.e. interactions of inter-particles, as well as the effect of sharp shape, which can occur remarkably enhanced local electromagnetic fields have been studied for increase of SERS signal. Thus, a properly rough surface with a disordered nanoparticles with smaller size than the wavelength of light has been designed a highly sensitive SERS, because the contribution of plasmon oscillation is more active by nanometer size of particles than by larger particles.²² There are major factors for enhancing the sensitivity of SERS substrate such as rough surface of metal, small metal nanoparticle and periodic metalstructures in submicrolength, among them, the periodic nanostructures have merits because the periodicity and inter-particle distance of the metal nano-structures which are tightly related to increase of SPR can be controllable.

Interference lithography (IL) is a sophisticated technique to quickly fabricate periodic nano-structures by transferring the laser intensity distribution into a photoresist in large area without defects.^{37,38} The morphology and geometry of the nanostructures could be controlled via the proper choice of laser components of IL which is a good method to fabricate the sensitive SERS substrate. ; this in turn will affect SPR coupling, which can be varied to optimize the SERS reaction for a given signal. Furthermore, the periodic structures by IL can be controllable optimization by providing a uniformly and reliable substrate which solves the reproducibility problem in SERS Whereas, the enhancement factor (EF) of SERS substrate by interference lithography is still low (10^5 to 10^6) because the dimension and distance between adjacent nanostructure is too large to occur the SPR effect by wavelength of light.^{28,29} However, The lager dimensional structures, which can increase the light scattering and diffraction by reacted with generally available Raman laser for SERS measurement, are also be considered as a supporters for highly sensitive SERS substrate by helping increase the light path which can occur the

SPR effect of small metal nanoparticles. Therefore, nanometer scale structures on the few hundred nm scale, which greatly affect the absorption properties, i.e. effective light trapping,³³⁻³⁵ caused by the maximized scattering events and the increase in the path length of the light, are also important for rational and controllable design of further optimized SERS substrates.

Here, we report the highly sensitive and reliable SERS substrate using a few hundred nanometer sized diamond-shaped Au nanoarrays (DGN) which decorated with a few tens nanometer scale of gold nanoparticles via interfere lithography (IL) and solution deposition. We discuss the synergetic effect of SPR and light scattering on the SERS signal by both simulation and experimental method. The much enhanced SERS performance of gold nanoparticle decorated DGNs (d-DGNs) demonstrates that appropriate proposed hybrid nanostructures can result in enhanced energy materials such as working electrodes for solar cell and PEC cell as well as SERS substrate. The merits of IL in the synthesis of hybrid structures are that they permit facile design to dual scale structures with a dimension of a few hundred nanometers with uniform condition, where the size of the morphologies are essential for sufficient light scattering in visible range as origin of SERS excitation.

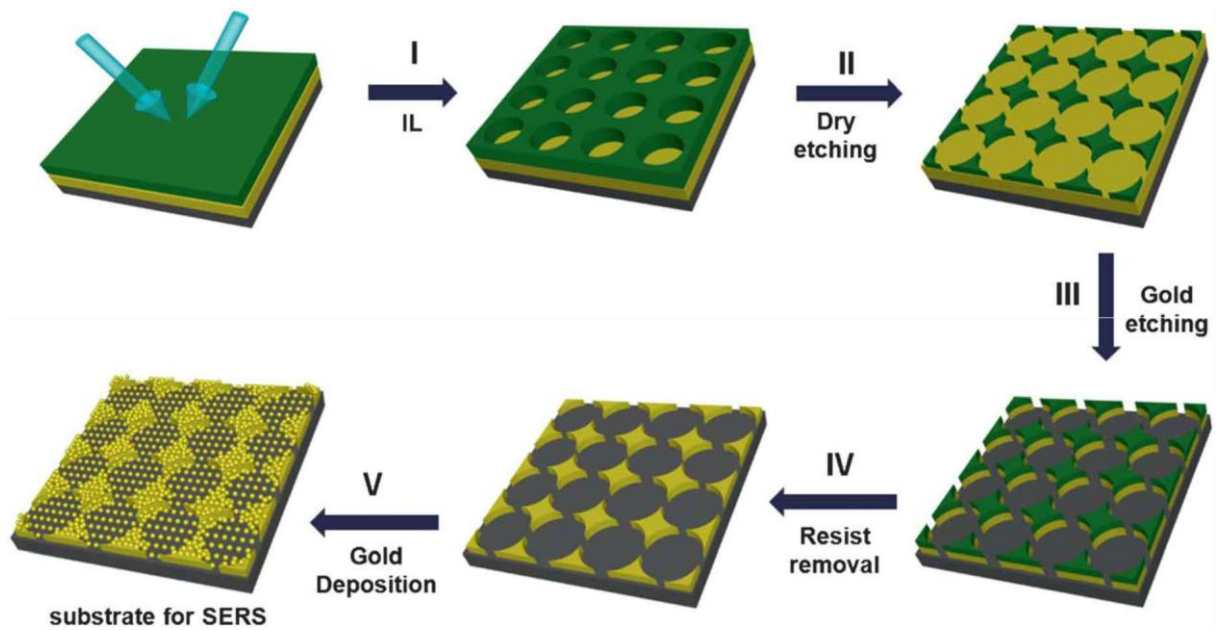


Figure. 1 Schemes for the fabrication procedures of d-DGNs. (I) Interference Lithography technique for fabrication periodic polymer template. (II) O₂ plasma etching of circular SU-8 for making diamond shape. (III) R.I.E etching for DGN shape of gold. (IV) Removal of the SU-8 polymer template (V) gold deposition on the DGN.

2. Experimental

Chemicals used

4-aminothiophenol (Sigma-Aldrich, 97%), SU-8 2010 (microchem), 1-methoxy-2-propanol acetate (SAMCHUN,99%), (3-mercaptopropyl)-trimethoxysilane (Sigma-Aldrich,95%), acetone (Skchemicals,99.5%), isopropanol (Skchemicals 99.5%), ethanol (Fisher scientific,99.9%), chloroauric acid (Sigma-Aldrich, >99.9%), sodium citrate (Sigma-Aldrich, >98%), zinc nitrate hexahydrate (Sigma-Aldrich, >98%), hexamethylenetetramine (HMTA) (Sigma-Aldrich, >98%), sodium hydroxide (Duksan pure chemicals) Ethanol, crystal violet(CV) (Sigma-Aldrich, >90%). All chemicals were used without further purification.

Fabrication of DGN patterns via interference lithography

The silicon substrates were cleaned using ultra-sonication with acetone, IPA and DI water for 15min and blow away by N₂ gas. A 5nm of Chrome layer and 300nm height of Au were coated by e-beam evaporator on the prepared substrate. In the case of

A 5nm Cr layer and 300 nm thick Au film was deposited by e-beam evaporator onto the Si substrate. A Cr/Au coated substrate was dipped in ethanol solution of 10mM 4-ATP (4-aminothiopheol) for 8 hours to attach 4-ATP SAMS monolayer on gold film. After remove the residue of 4-ATP, a 500 nm thick photoresist film was coated by spincoating at 3000rpm on the Au substrate to fabricate periodic patterns with circular holes through interference lithography. The Su-8 coated samples were double exposed for 6 x 6s by rotating the sample 90 degrees.

A post-exposure bake and hard-bake procedures were conducted for 10min at 75°C and 95°C, respectively, before develop eh Su-8 photoresist by propylene glycol monomethyl ether acetate. After plasma treatment (1.5 Torr using Room Air, 18W) for 10 min on patterned SU-8 gold substrate, the gold is partially etched away by metal reactive ion etching (metal RIE) at 2m Torr of Cl₂/Ar (10sccm:40sccm) condition.

Attachment of gold nanoparticles on the DGN substrate.

The ethanol solution of 30 mM of chloroauric acid was mixed with solution of 1% of sodium citrate. The mixture was placed in the oven at 100°C for 30min and stay it cool down to room temperature. The pH of the mixture solution was optimized to be 8 using NaOH solution.

3. Results and Discussion

The illustrations of the figure 1 depict the synthesis procedure to fabricate d-DGNs. First, a 300nm of gold film was coated on the cleaned silicon substrate and monolayer of 4-aminothiophenol was coated on Au film to enhance the adhesion between polymer photoresist and gold. A two-dimensional periodic patterns of holes in 300nm height Su-8 photoresist were fabricated thorough IL composed of 325nm of He-Cd laser. To fabricate the 350nm and 550nm holes in Su-8, periodicity of template with 550nm and 800nm was used, respectively. For shape control of DGNs we used a hardening process

The hardening treatment, which help increase the durability of Su-8 polymer template was conducted to shape control of DGNs more easily. The O₂ plasma was treated on periodic Su-8 patterns to fabricate the diamond shape of polymer template with sharp edge by etched away thinly connected regions in Su-8.³⁶ The thickness of Su-8 reduced to 300nm and the circular walls were removed and diamond shaped polymer template was fabricated by the isotropic O₂ plasma etching. To fabricate the diamond-shaped gold arrays, the open region of the Au film were etched away using a R.I.E process. As distance between hole-hole become longer, length between the edges of the arrays, the sharpness of gold posts become shorter by varying the tip angle from 80 to 30 degree after RIE reaction. Then, the residue Su-8 polymer was fully etched by the long-time O₂ plasma. Finally, clusters of 25-35nm of Au NPs which increase the SPR effect were decorated by hydrothermal growth on diamond shaped gold arrays and Si substrate using a precursor of Au.

The SEM images of the nanostructures during the fabrication steps for the d-DGN are shown in Figure 2. Figure 4a shows that height, period and diameter of periodic polymer template designed in this work are a 500nm, 550nm and 350nm, respectively, synthesized through IL. The periodic diamond shaped Su-8 arrays with a length of 350 nm and distance between the each edges in from 150nm – 200nm fabricated by O₂ plasma treatment as shown in figure 4b. Figure 4c is a SEM image of the d-DGN followed by RIE etching to get rid of the open region of gold substrate between the posts. The design of a diamond shape which has the 4 sharp edge is selected rather than a cylindrical Au post shape so that get the higher EF because the sharp edge can increased intensity of SPR along the faces and these results are well matched the simulation data. The d-DGNs synthesized from deposition of Au NPs on the surface of the DGNs, showing clear proof of the uniformly decorated gold nanoparticles over a large area with 25-30nm diameters are shown in Figure 4d.²⁸ Even though the periodicities of Au NPs are slightly random, the gap between Au NPs is considered to less than 8 nm because of the high concentrations of Au NPs, that is essential to take remarkably enhanced SERS signal.

Furthermore, it is notable that the AU NPs has preferred to grow at the end of diamond gold posts and this tendency will facilitates to increase the localized surface plasmon.

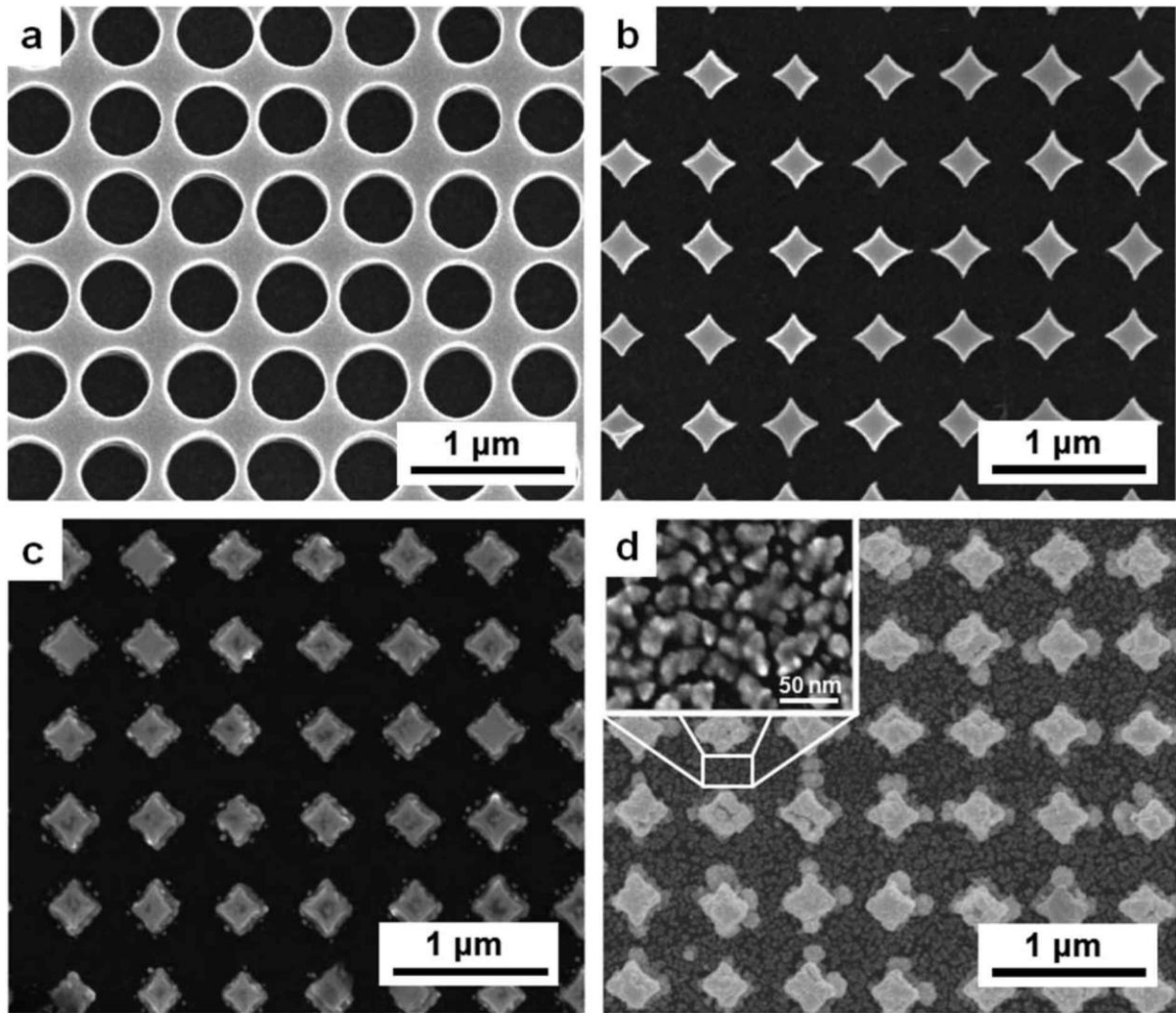


Figure. 2 SEM images of (a) a square pattern of air cylinders in a SU-8 film after baking and development of the double exposure IL pattern. (b) Sharply pointed diamond shaped posts of SU-8 fabricated via oxygen plasma etching of the photoresist on the gold substrate. (c) 350 nm DGN with 200 nm spacing between edges after metal RIE of the gold film and removal of the remaining SU-8. (d) A dual-scale 350 nm d-DGN after deposition of gold nanoparticles. The inset is a close-up image of the rectangular area showing gold nanoparticle separation. Note that the preferential accumulation of gold nanoparticles is apparent along the edges/tips of the nanoposts.

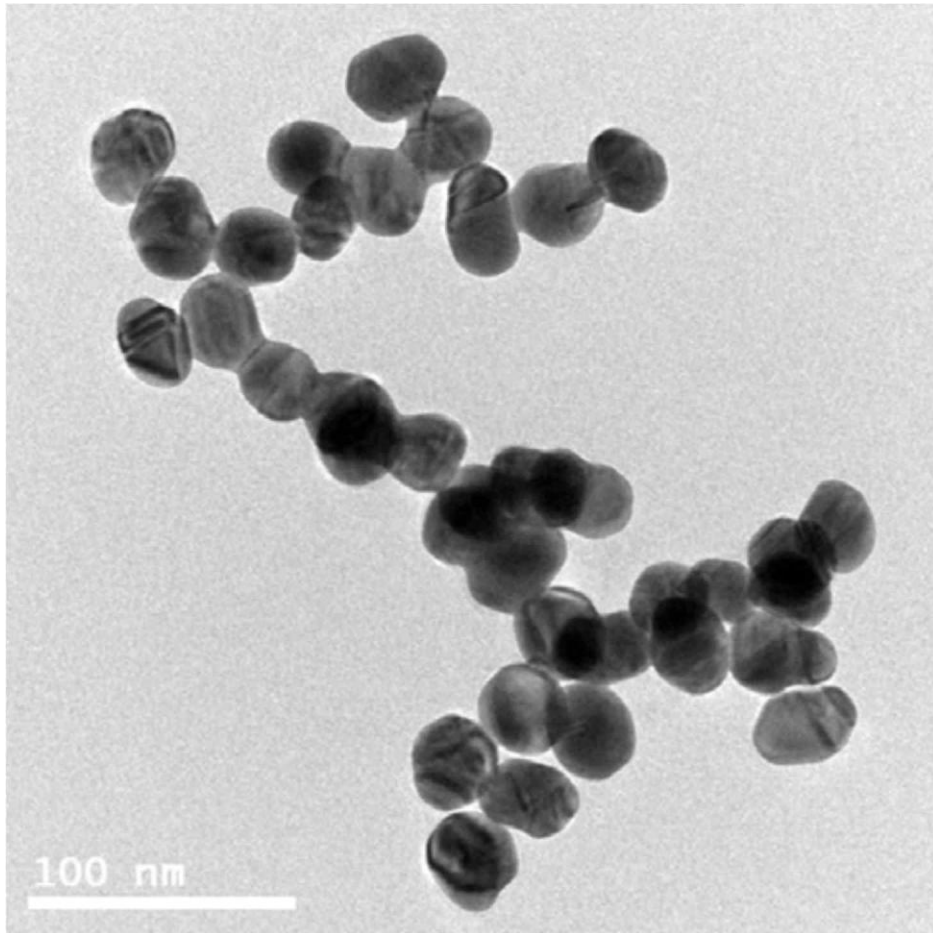


Figure 3. TEM image of as-prepared Au nanoparticles.

The absorbance spectrum of the gold nanostructure were measured so as to elucidate the effects of morphological properties and dimensions and the reflection properties of the hybrid samples also are taken as shown in Figure. 5. The 300nm of height and 350nm of periodicity of DGNs and 300nm of height and 800 nm of periodicity of DGNs film on silicon substrates are shown Figure 5. The high reflectance peaks of at pristine Au film from 500nm was corresponded to the nature optical property of the gold. As compared with pristine Au film, the 350nm DGNs and 500nm DGNs exhibited much reduced reflectance in the visible region which shows the light trapping nature of the periodic metal structures. The direct-camera images in Figure 5. are well matched with the UV-vis spectrum. The density of the gold film, 350nm DGNs, and 500nm DGNs is measured to be 100, 29.6 and 19.07 % of gold by calculating the SEM images, the very enhanced in UV-vis absorption peak of 350nm DGNs and 500nm DGNs is because of the higher input of the scattering property. The maximize SER intensity is taken when the minimum reflectance of an Au surface react with the Raman laser wavelength. The 350nm DGNs display a reflectance minimum 629.5nm and thus are assumed to exhibit the highest SERS signal for 629.5 nm Raman laser however the 500nm DGNs display a red-shift of reflectance minimum around 700nm. The increased UV-vis spectrum of 350nm DGNs in the visible region in range from 550nm to 650nm, demonstrates the largest SPR attributable to sufficient light because of the well matched sizes of the DGN structure for scattering/diffraction with irradiated light in the visible range. The effect of the number of DGN structure and the gap between gold nanoparticles on SERS intensity was studied by examination of the EF measured from 1×10^{-7} M of CV solution on a pristine gold film of irregularly decorated 30 nm gold nanoparticles and 3 DGNs with a stable diamond shaped morphology of 350nm with a 629.5nm Raman laser. The DGN without Au NPs between gold nanoposts (29% of gold density, denoted as DGN-29), a DGN with irregularly decorated 30nm Au NPs with a density of 44% (denoted as d-DGN-44), and a DGN with irregularly deposited 30nm Au NPs with a density of 78% (denoted as d-DGN-78) are examined. The average density of Au NPs on Si substrate was optimized by changing the cycles of gold deposition and the density of gold precursor solution, giving a manipulative substrate to study the increase of SERS. The average size of Au NPs sometimes enhances reaching to 80-90 nm in diameter in the d-DGN-78 because of the synthesis of clusters.

The comparison of SERS spectra of CV on the pristine gold NPs and pristine gold nanopost is included in Figure 4a. The peak at 1172 cm^{-1} of CV is used to calculate the SERS EF.

As compared with the very small peak of the DGN-29 sample (without Au nanoparticles between DGNs) which well matched with the small EF values of the few hundred sized pattern nanostructures similar to as reported elsewhere,^{20,21} the examined SERS peaks at 1591, 1371, 1172, 914 and 804 cm^{-1} are easily obvious for the Au NPs substrate. The EFs of pristine Au NPs substrate and DGN-29 were obtained to be 2.3×10^8 and 2.6×10^6 , respectively. The large differences approximately two order between the Au NPs and DGN-29 can be attributed to the feature that extreme ratio of the EF comes from the excitation

of the surface plasmon resonance mode supported by few tens of gold nanoparticles, however, the multipole resonance, which may come from a few hundreds of larger particle, result in a relevantly lower EF at the visible range excitation.^{22, 37-39} Furthermore, Figure 6b shows the importance of the density of gold structures for SERS enhancement was demonstrated by the comparison of the EF values for d-DGN78, d-DGN-44 and DGN-29. Because decorated lower size Au NPs take advantages of dipolar plasmons, the gold nanoparticle decorated DGN nanostructures shows higher EF of SERS intensity. In addition, inset images in each figures shows the more density of Au NPs DGN have, the more enhanced EF signal is measured. The normalized light intensity ($|E|^2$) distribution of the simulation data shows the average gap between particle-particle is lower, the total electromagnetic fields are increased by coupling of the metal nanoparticles. When the interparticle distance in the d-DGN-78 is less than 10nm, which is satisfied the condition for the optimizing their coupling with adjacent metal nanoparticles, the bundles of Au NPs can become the clusters for combining plasmonic oscillation of the many small Au NPs. This result is well matched with recent reports which explore the SERS enhancement of the electric field via metal nanoparticle clusters in small gaps.^{20,40,41} As compared with EF of d-DGN-78, the EF of both DGN-29 and d-DGN-44 is lower due to low EM coupling. Therefore, the highly enhanced EF in the d-DGN-78 can be attributed by synergetic effect of high surface plasmon resonance from small Au NPs and the increased scattered light source for the excitation of the SPR of Au NPs from the light trapping effect by DGN posts. The surface plasmon resonance according to a function of the the morphologies was designed through finite-difference time domain (FDTD) simulation.⁴²⁻⁴⁴ A laser of 632.5 nm wavelength transferred vertically to the specimen with linear polarization along the perpendicular direction. The enhanced electromagnetic wave near sharp edge of DGN is specially noticeable when the polarization of the irradiated electromagnetic wave is parallel to the diamond shape DGN as shown in the simulation data.

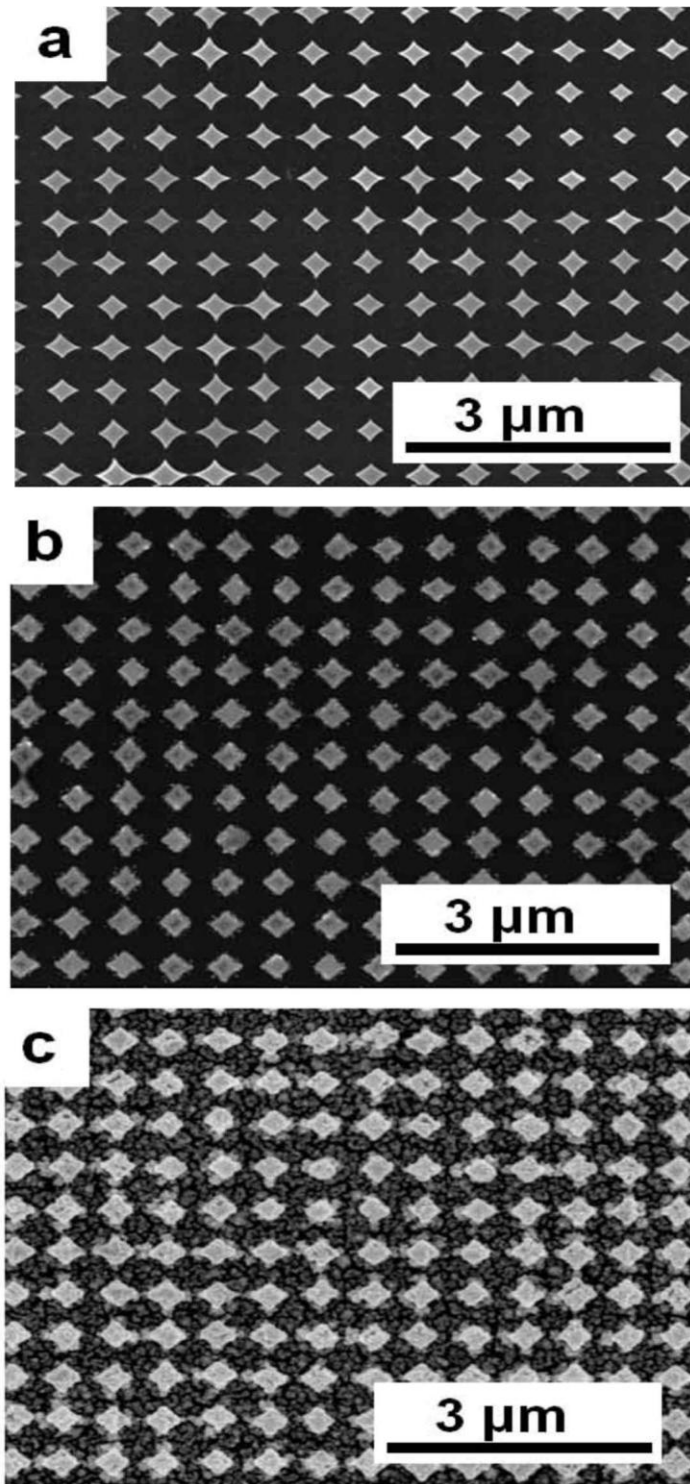


Figure 4. SEM images of low magnification mode: a) 350nm sized SU-8 polymer template with sharp-edges. b) 200nm sized DGN gap between end of edges. c) DGN with Au NPs.

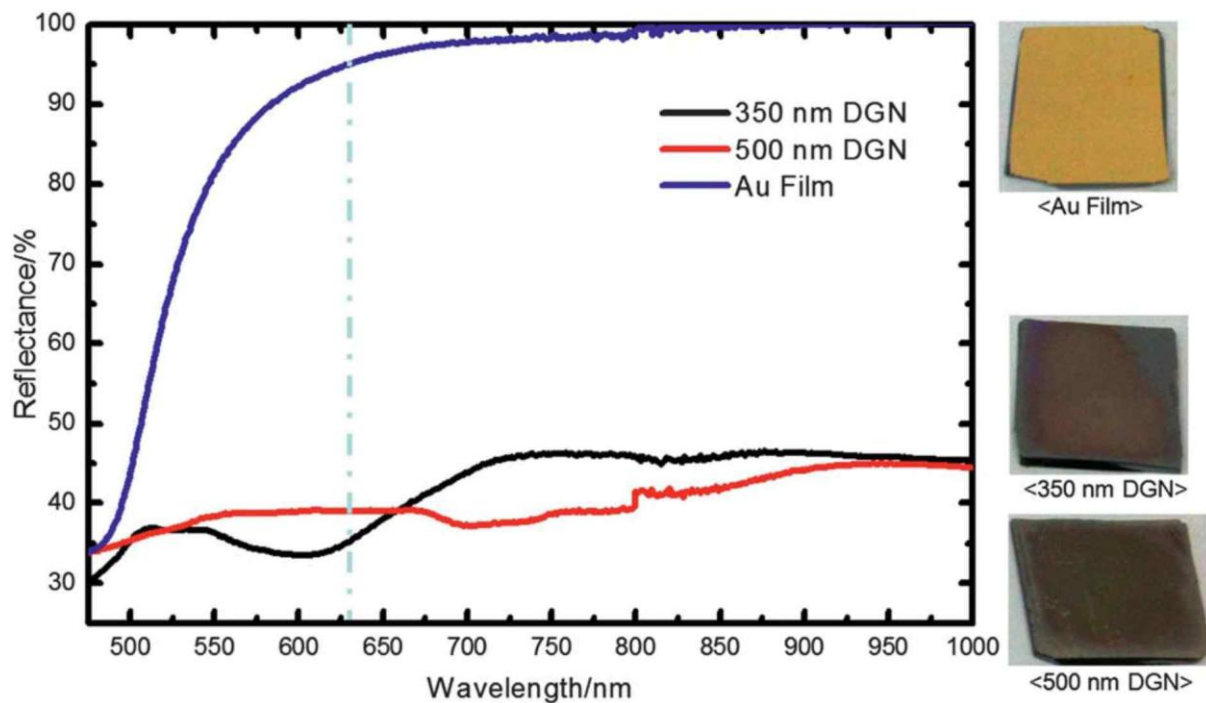


Figure. 5 Reflection spectrums of a pristine Au film, 350 nm of DGN and 500 nm of DGN substrates with a height of 300 nm on the cleaned silicon substrate. The direct camera image of each sample with the size of 1 cm x 1 cm, representing the reflectivity spectra in the visible range, appears at the right.

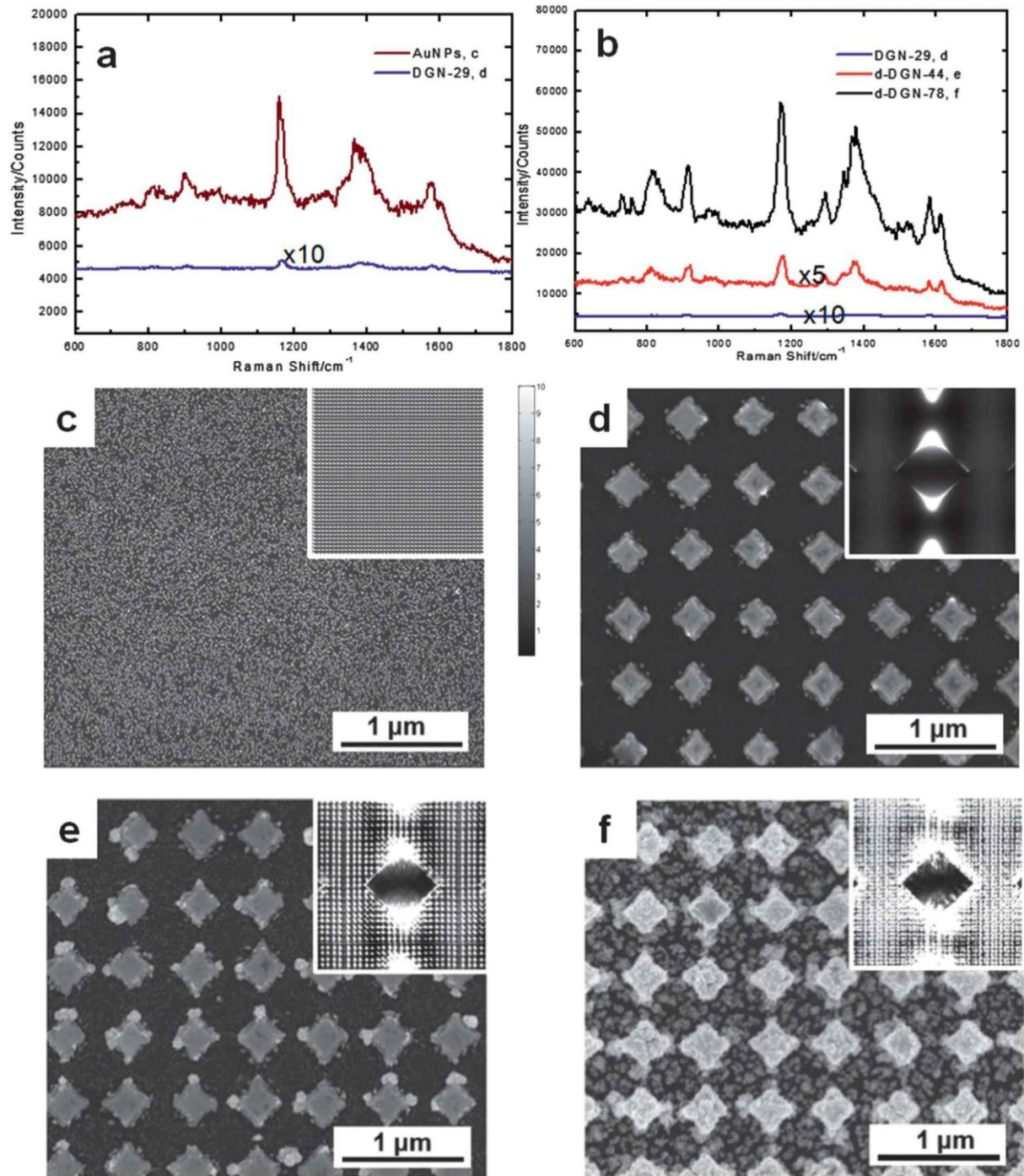


Figure. 6 SERS spectrum of DGNs with size of 350 nm and 3 different densities of Au NPs by 629.5 nm Raman laser with a power of 0.1mW. (a) The SERS spectrum of DGN-29 vs. pristine Au nanoparticles substrate. (b) The SERS spectrum of DGN-29, d-DGN-44, and d-DGN-78. The SEM images of (c) pristine gold NP, (d) DGN-29, d-DGN-44, and (e) d-DGN-78 substrates. The inset images in the each SEM image are normalized light intensity ($|E|^2$) distribution of electric field distribution of the each morphology on the top view via the height of the 300nm diamondal gold array

The simulated intensity of electromagnetic waves in the inset of Figure 6f exhibits the highest SPR, which is well matched to the experimental data. The highest SPR property is attributed to the favorable excitation of the SPR of small Au NPs promoted by the multiple scattering feature of the larger DGN array: the optical resonance of the larger DGN spread the optical light surrounding it. The increased optical wave has the more chances to interact with the decorated small Au NPs and promote larger value than the plasmonic strength from small Au NPs alone. We compared the SERS of irregularly spread Au NPs, 350nm DGN and 500nm DGN so as to further study the influence of the size of the DGN structures on light trapping and very intensive SERS. The peaks of SERS shown Figure. 8a for a uniform pristine 30nm of Au NPs and Au NPs decorated on 350 nm diamond DGN and 500 nm diamond DGN, each with the similar areal density of 77%. The EF of SERS is calculated as 2.3×10^8 , 2×10^9 , and 7.8×10^8 , respectively from 632.5nm of Raman laser. The 10 times and 3 times higher EF of SERS of Au NPs decorated 350nm DGN than that of pristine Au NPs film and Au NPs/500 nm DGN is obtained due to light trapping effects. It is noteworthy that the EF of 350nm d-DGNs is higher than 500nm d-DGNs because 350nm DGN arrays can be interacted better than 500nm d-DGNs with 632.5nm laser.

This correlates well with the previous experiments on metal coated spheres with various diameters ranging from 350 nm to 800 nm made from polystyrene beads; the 350 nm diameter sphere exhibited the greatest plasmonic peak at an excitation of 633 nm.^{45,46} The FDTD simulations also verify the comparison of the electric field enhancement between simple gold nanoparticles substrate and two dimensions of diamond-shaped 300 nm-thick gold nanoposts (350 nm and 500 nm diagonal dimension). From our systematic approach, we suggest that the compact assembly of small particles is not the best choice to construct enhanced hot spots within a certain area. If the minimum density and suitably small size of gold nanoparticles are maintained, the total EM field can be further enhanced by the introduction of a properly designed larger dimension structure with the capability of maximizing the absorption of the light for plasmonic excitation. Additionally, the d-DGN structure provides a highly repeatable EF compared to the pure gold nanoparticle pristine substrate due to the uniformity of gold deposition performed on the pre-patterned substrate, which is one of the most challenging issues for reliable SERS measurements. For example, the SERS spectra from 10 random locations on each sample are quite similar for 9 out of 10 samples.

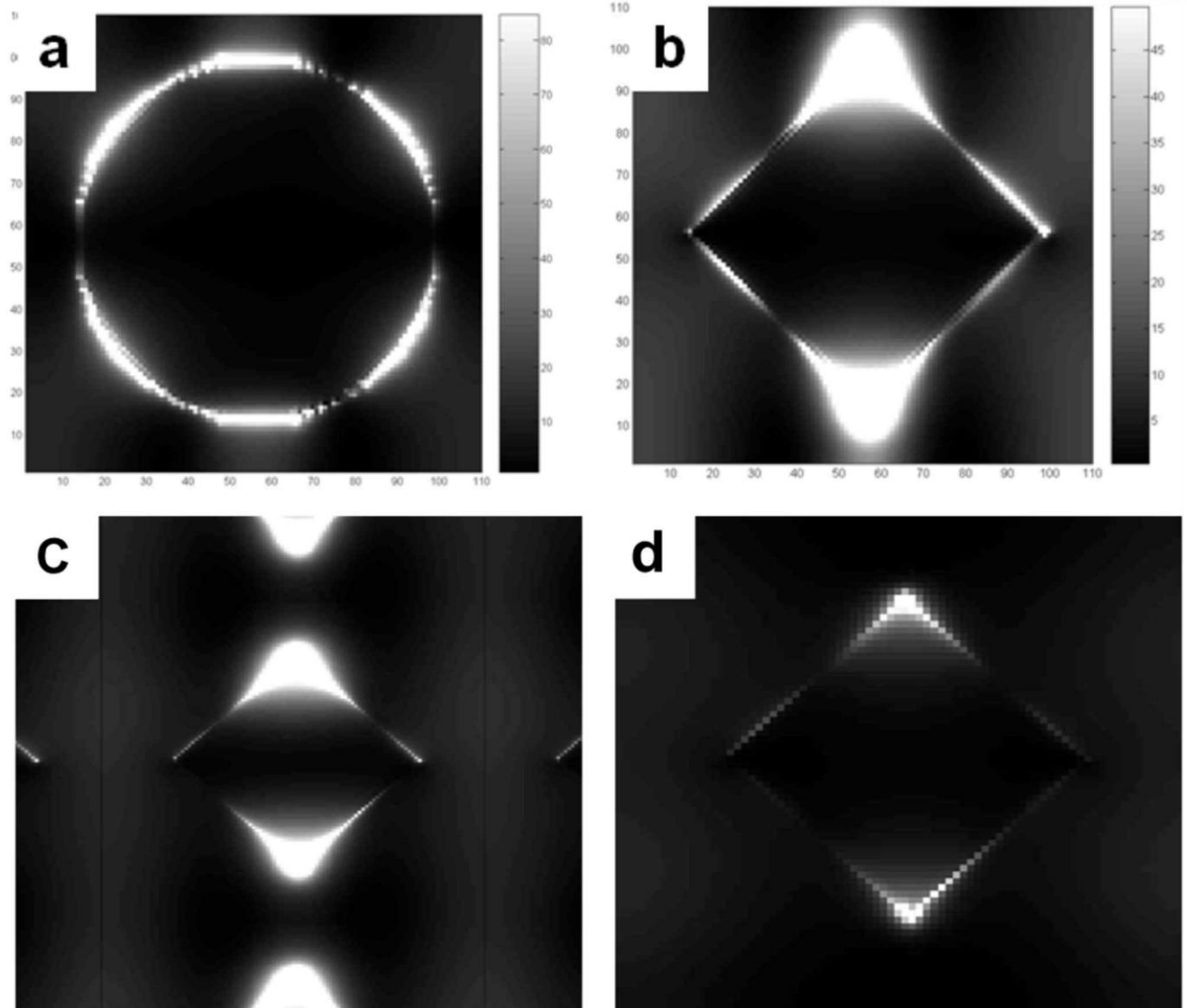


Figure 7. Simulated Electric field distribution of (a) circular shape and (b) diamondal shape of gold structure with the 350nm diameter and 500nm periodicity.

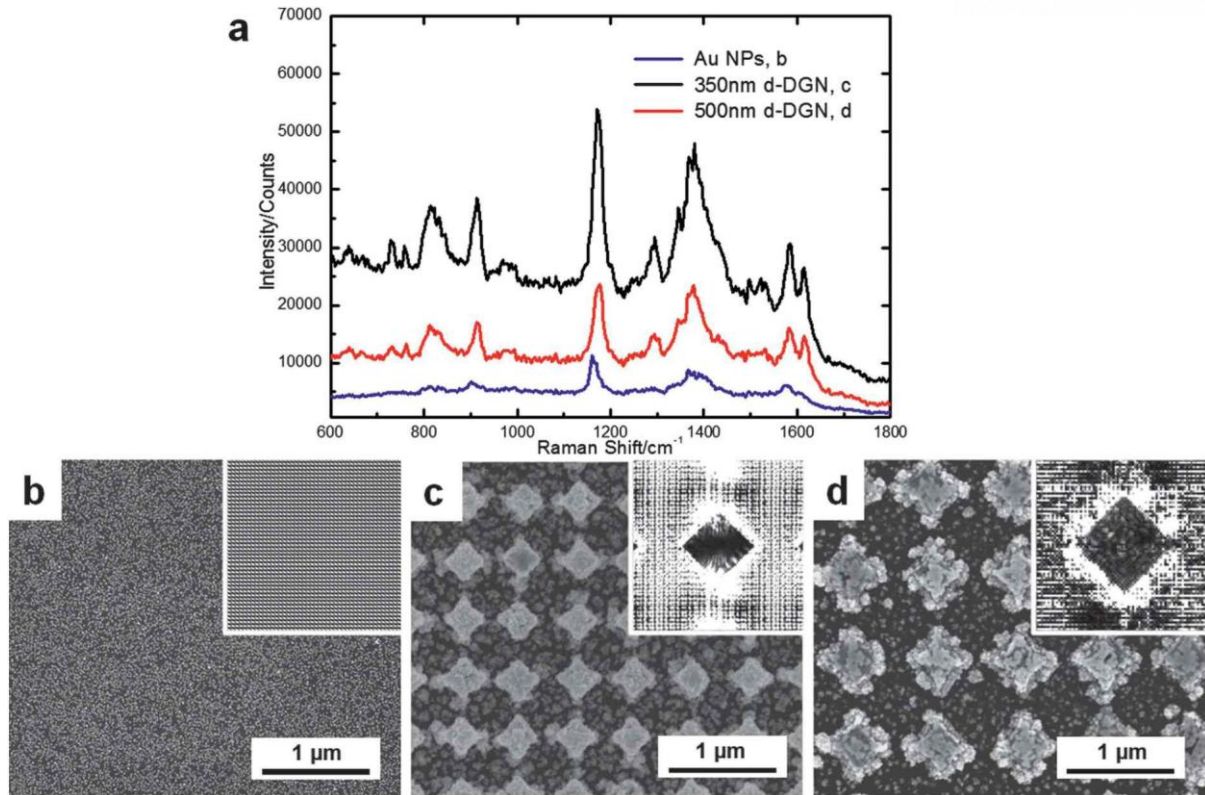


Figure. 8 (a) SERS spectrum of DGN taken at 632.5 nm laser excitation with a power of 0.1 mW; (b–d) SEM images of SERS substrates: Au NPs on flat Silicon substrate (b); d-DGN with the dimonal dimension of 350 nm arrays (c); and d-DGN with the dimonal dimension of 500 nm posts (d). The corresponding calculated electric field enhancements are given. The power of the lasers are normalized to the same scale for comparison. The highest plasmonic behavior of the structure in (c) is observed.

4. Conclusion

In conclusion, we successfully fabricated a Au NPs decorated DGNs as a highly sensitive and reproducible SERS substrate by using interference lithography which can control the morphology of the gold arrays. A DGN with a diamond size of 350nm was designed to obtain maximum photon trapping effects through increased light scattering because of the dimensions of the nanostructure, which are similar dimension to the wavelength of the incident laser. The photon trapping in the d-DGN morphology with well controlled density of Au NPs results in an extremely enhancement in the absorbance of the visible light range, leading to a reliable SERS EF of higher than 10^9 . These results exhibit that the synergy of a dual-scale structure is a good approach for achieving maximized SERS enhancement by light trapping in the larger dimension structures as well as enhanced plasmon excitation in the smaller size particles.

5. REFERENCES

1. Abu Hatab, N. A.; Oran, J. M.; Sepaniak, M. J., Surface-enhanced Raman spectroscopy substrates created via electron beam lithography and nanotransfer printing. *ACS Nano* 2008, 2 (2), 377-385.
2. Adams, S. M.; Campione, S.; Caldwell, J. D.; Bezares, F. J.; Culbertson, J. C.; Capolino, F.; Ragan, R., Non-lithographic SERS Substrates: Tailoring Surface Chemistry for Au Nanoparticle Cluster Assembly. *Small* 2012, 8 (14), 2239-2249.
3. Ahn, H.-J.; Kim, S.-I.; Yoon, J.-C.; Lee, J.-S.; Jang, J.-H., Power conversion efficiency enhancement based on the bio-inspired hierarchical antireflection layer in dye sensitized solar cells. *Nanoscale* 2012, 4 (15), 4464-4469.
4. Alvarez-Puebla, R. A.; Liz-Marzan, L. M., Environmental applications of plasmon assisted Raman scattering. *Energy Environ. Sci.* 2010, 3 (8), 1011-1017.
5. Cho, W. J.; Kim, Y.; Kim, J. K., Ultrahigh-Density Array of Silver Nanoclusters for SERS Substrate with High Sensitivity and Excellent Reproducibility. *ACS Nano* 2012, 6 (1), 249-255.
6. Fang, J.; Du, S.; Lebedkin, S.; Li, Z.; Kruk, R.; Kappes, M.; Hahn, H., Gold Mesostructures with Tailored Surface Topography and Their Self-Assembly Arrays for Surface-Enhanced Raman Spectroscopy. *Nano Lett.* 2010, 10 (12), 5006-5013.
7. Freeman, R. G.; Grabar, K. C.; Allison, K. J.; Bright, R. M.; Davis, J. A.; Guthrie, A. P.; Hommer, M. B.; Jackson, M. A.; Smith, P. C.; Walter, D. G.; Natan, M. J., SELF-ASSEMBLED METAL COLLOID MONOLAYERS - AN APPROACH TO SERS SUBSTRATES. *Science* 1995, 267 (5204), 1629-1632.
8. GarciaVidal, F. J.; Pendry, J. B., Collective theory for surface enhanced Raman scattering. *Phys. Rev. Lett.* 1996, 77 (6), 1163-1166.
9. Gersten, J.; Nitzan, A., ELECTROMAGNETIC THEORY OF ENHANCED RAMAN-SCATTERING BY MOLECULES ADSORBED ON ROUGH SURFACES. *J. Chem. Phys.* 1980, 73 (7), 3023-3037.
10. Halas, N. J.; Lal, S.; Chang, W.-S.; Link, S.; Nordlander, P., Plasmons in Strongly Coupled Metallic Nanostructures. *Chem. Rev.* 2011, 111 (6), 3913-3961.
11. Hartland, G. V., Optical Studies of Dynamics in Noble Metal Nanostructures. *Chem. Rev.* 2011, 111 (6), 3858-3887.
12. Homan, K. A.; Chen, J.; Schiano, A.; Mohamed, M.; Willets, K. A.; Murugesan, S.; Stevenson, K. J.; Emelianov, S., Silver-Polymer Composite Stars: Synthesis and Applications. *Adv. Funct. Mater.* 2011, 21 (9), 1673-1680.
13. Hore, S.; Vetter, C.; Kern, R.; Smit, H.; Hinsch, A., Influence of scattering layers on efficiency of dye-sensitized solar cells. *Sol. Energy Mater. Sol. Cells* 2006, 90 (9), 1176-1188.

14. Hou, W.; Pavaskar, P.; Liu, Z.; Theiss, J.; Aykol, M.; Cronin, S. B., Plasmon resonant enhancement of dye sensitized solar cells. *Energy. Environ. Sci.* 2011, 4 (11), 4650-4655.
15. Jang, J.-H.; Ullal, C. K.; Kooi, S. E.; Koh, C.; Thomas, E. L., Shape control of multivalent 3D colloidal particles via interference lithography. *Nano Lett.* 2007, 7 (3), 647-651.
16. Jang, J.-H.; Ullal, C. K.; Maldovan, M.; Gorishnyy, T.; Kooi, S.; Koh, C.; Thomas, E. L., 3D micro- and nanostructures via interference lithography. *Adv. Funct. Mater.* 2007, 17 (16), 3027-3041.
17. Jia, L.; Bitá, I.; Thomas, E. L., Impact of Geometry on the TM Photonic Band Gaps of Photonic Crystals and Quasicrystals. *Phys. Rev. Lett.* 2011, 107 (19).
18. Jia, L.; Thomas, E. L., Initiation of a Database of Functional Micro- and Nanostructures. *Small* 2011, 7 (21), 2981-2989.
19. Kelly, K. L.; Coronado, E.; Zhao, L. L.; Schatz, G. C., The optical properties of metal nanoparticles: The influence of size, shape, and dielectric environment. *J. Phys. Chem. B* 2003, 107 (3), 668-677.
20. Kim, D. S.; Ji, R.; Fan, H. J.; Bertram, F.; Scholz, R.; Dadgar, A.; Nielsch, K.; Krost, A.; Christen, J.; Goesele, U.; Zacharias, M., Laser-interference lithography tailored for highly symmetrically arranged ZnO nanowire arrays. *Small* 2007, 3 (1), 76-80.
21. Kim, N. H.; Lee, S. J.; Moskovits, M., Reversible Tuning of SERS Hot Spots with Aptamers. *Adv. Mater.* 2011, 23 (36), 4152-+.
22. Kim, W. S.; Jia, L.; Thomas, E. L., Hierarchically Ordered Topographic Patterns via Plasmonic Mask Photolithography. *Adv. Mater.* 2009, 21 (19), 1921-1926.
23. Knight, M. W.; Sobhani, H.; Nordlander, P.; Halas, N. J., Photodetection with Active Optical Antennas. *Science* 2011, 332 (6030), 702-704.
24. Kumbhar, A. S.; Kinnan, M. K.; Chumanov, G., Multipole plasmon resonances of submicron silver particles. *J. Am. Chem. Soc.* 2005, 127 (36), 12444-12445.
25. Li, J. F.; Huang, Y. F.; Ding, Y.; Yang, Z. L.; Li, S. B.; Zhou, X. S.; Fan, F. R.; Zhang, W.; Zhou, Z. Y.; Wu, D. Y.; Ren, B.; Wang, Z. L.; Tian, Z. Q., Shell-isolated nanoparticle-enhanced Raman spectroscopy. *Nature* 2010, 464 (7287), 392-395.
26. Li, Q.; Kuo, C. W.; Yang, Z.; Chen, P.; Chou, K. C., Surface-enhanced IR-visible sum frequency generation vibrational spectroscopy. *PCCP* 2009, 11 (18), 3436-3442.
27. Li, S.; Pedano, M. L.; Chang, S.-H.; Mirkin, C. A.; Schatz, G. C., Gap Structure Effects on Surface-Enhanced Raman Scattering Intensities for Gold Gapped Rods. *Nano Lett.* 2010, 10 (5), 1722-1727.
28. Liang, H.; Li, Z.; Wang, W.; Wu, Y.; Xu, H., Highly Surface-roughened "Flower-like" Silver Nanoparticles for Extremely Sensitive Substrates of Surface-enhanced Raman Scattering. *Adv. Mater.* 2009, 21 (45), 4614-4618.
29. Lu, Y.; Liu, G. L.; Lee, L. P., High-density silver nanoparticle film with temperature-controllable interparticle spacing for a tunable surface enhanced Raman scattering substrate. *Nano Lett.* 2005, 5

- (1), 5-9.
30. Marquestaut, N.; Martin, A.; Talaga, D.; Servant, L.; Ravaine, S.; Reculosa, S.; Bassani, D. M.; Gillies, E.; Lagugne-Labarthet, F., Raman enhancement of azobenzene monolayers on substrates prepared by Langmuir-Blodgett deposition and electron-beam lithography techniques. *Langmuir* 2008, 24 (19), 11313-11321.
 31. You, E.-A.; Zhou, W.; Suh, J. Y.; Huntington, M. D.; Odom, T. W., Polarization-Dependent Multipolar Plasmon Resonances in Anisotropic Multiscale Au Particles. *Acs Nano* 2012, 6 (2), 1786-1794.
 32. Yap, F. L.; Thoniyot, P.; Krishnan, S.; Krishnamoorthy, S., Nanoparticle Cluster Arrays for High-Performance SERS through Directed Self-Assembly on Flat Substrates and on Optical Fibers. *Acs Nano* 2012, 6 (3), 2056-2070.
 33. Weitz, D. A.; Gramila, T. J.; Genack, A. Z.; Gersten, J. I., ANOMALOUS LOW-FREQUENCY RAMAN-SCATTERING FROM ROUGH METAL-SURFACES AND THE ORIGIN OF SURFACE-ENHANCED RAMAN-SCATTERING. *Phys. Rev. Lett.* 1980, 45 (5), 355-358.
 34. Warren, S. C.; Thimsen, E., Plasmonic solar water splitting. *Energy. Environ. Sci.* 2012, 5 (1), 5133-5146.
 35. Wang, H.; Halas, N. J., Mesoscopic Au "Meatball" particles. *Adv. Mater.* 2008, 20 (4), 820-+.
 36. Thiyagarajan, P.; Ahn, H.-J.; Lee, J.-S.; Yoon, J.-C.; Jang, J.-H., Hierarchical Metal/Semiconductor Nanostructure for Efficient Water Splitting. *Small* 2013, 9 (13), 2341-2347.
 37. Sun, Y., Metal Nanoplates on Semiconductor Substrates. *Adv. Funct. Mater.* 2010, 20 (21), 3646-3657.
 38. Smythe, E. J.; Dickey, M. D.; Bao, J.; Whitesides, G. M.; Capasso, F., Optical Antenna Arrays on a Fiber Facet for in Situ Surface-Enhanced Raman Scattering Detection. *Nano Lett.* 2009, 9 (3), 1132-1138.
 39. Sawai, Y.; Takimoto, B.; Nabika, H.; Ajito, K.; Murakoshi, K., Control of near-infrared optical response of metal nano-structured film on glass substrate for intense Raman scattering. *Faraday Discuss.* 2006, 132, 179-190.
 40. Ross, B. M.; Wu, L. Y.; Lee, L. P., Omnidirectional 3D Nanoplasmonic Optical Antenna Array via Soft-Matter Transformation. *Nano Lett.* 2011, 11 (7), 2590-2595.
 41. Paczesny, J.; Kaminska, A.; Adamkiewicz, W.; Winkler, K.; Sozanski, K.; Wadowska, M.; Dziecielewski, I.; Holyst, R., Three Steps of Hierarchical Self Assembly Toward a Stable and Efficient Surface Enhanced Raman Spectroscopy Platform. *Chem. Mater.* 2012, 24 (19), 3667-3673.
 42. Oldenburg, S. J.; Hale, G. D.; Jackson, J. B.; Halas, N. J., Light scattering from dipole and quadrupole nanoshell antennas. *Appl. Phys. Lett.* 1999, 75 (8), 1063-1065.
 43. Murphy, C. J.; Gole, A. M.; Stone, J. W.; Sisco, P. N.; Alkilany, A. M.; Goldsmith, E. C.; Baxter, S.

- C., Gold Nanoparticles in Biology: Beyond Toxicity to Cellular Imaging. *Acc. Chem. Res.* 2008, 41 (12), 1721-1730.
44. Moskovits, M., Surface-enhanced Raman spectroscopy: a brief retrospective. *Journal of Raman Spectroscopy* 2005, 36 (6-7), 485-496.
45. Mayer, K. M.; Lee, S.; Liao, H.; Rostro, B. C.; Fuentes, A.; Scully, P. T.; Nehl, C. L.; Hafner, J. H., A label-free immunoassay based upon localized surface plasmon resonance of gold nanorods. *Acc Nano* 2008, 2 (4), 687-692.

Chapter 5. MoS₂/Ti-doped α -Fe₂O₃ Heterojunctions for Enhanced Photoelectrochemical Performance

1. Introduction

Photoelectrochemical (PEC) cells that convert solar energy to a hydrogen gas has attracted much attention since Honda and Fujishima demonstrated the first application of titanium dioxide (TiO₂) in 1972.¹⁻⁴ However, the large band gap of TiO₂ (3.1-3.3eV) hinders absorption of visible light and limits the solar-to-hydrogen efficiency to 2.2% under AM 1.5 illumination.^{5, 6} To substitute the TiO₂ photoanode for the PEC cell, many semiconductor materials with a lower band gap have been researched, for example, Fe₂O₃, BiVO₄, WO₃ and Ta₃N₅.⁷⁻¹¹ Among many semiconductors, hematite (α -Fe₂O₃) is one of the most fascinating photoanode materials with a high theoretical maximum solar-to-hydrogen efficiency of 16%, a relatively low bandgap (2.1-2.2 eV), low cost, high chemical stability, non-toxicity and abundance.¹²⁻¹⁴

However, several problems, such as a very short diffusion length, low conduction band bottom and short carrier life time, have prevented hematite from achieving the practical excellent PEC performance of α -Fe₂O₃.¹⁵⁻¹⁷ To overcome these drawbacks, diverse methods have been investigated such as doping of α -Fe₂O₃ by elements, morphology control and adoption of catalysts on the surface of α -Fe₂O₃. Si, Ti and Pt have been widely used as dopants to enhance PEC performance by increasing the electrical conductivity, crystallinity and hole diffuse length.^{13, 18, 19} For example, nanotubes, nanowires, ultrathin sheets and 3D-inverse opal structures of α -Fe₂O₃ with facile hole/electron transfer pathways have been suggested to solve these issues of α -Fe₂O₃.²⁰⁻²² Besides, applying catalysts such as Co-Pi and IrO₂ on the surface of α -Fe₂O₃ has been suggested to improve the PEC performance by reducing the onset potential.^{23,24}

Recently, the p-n heterojunction has been tried to enhance the PEC performance of the photoanode because it is hard to obtain maximum PEC performance using a single material photoanode because of the fixed bandgap, band position and poor charge separation of photogenerated electrons/holes. It has been reported that the electric field created in the p-n junctions of semiconductors not only suppresses the charge recombination but also enhances the photogeneration of electron-hole pairs.²⁵⁻²⁸

The molybdenum disulfide (MoS₂), a two-dimensional (2D) sheet with an optical band gap of 1.8 eV,²⁹ falling in the visible range, has received great attention in phototransistors,³⁰ gas sensors,³¹ electrocatalysts³² and other applications due to its unique electronic, mechanical and optical properties. Moreover, the MoS₂ thin layer, which is considered as a p-type semiconductor,³³ can easily extract the holes from a photoexcited absorber by fabricating the p-n junction with an n-type semiconductor, such as MoS₂/CdS or MoS₂/rGO junctions.^{34, 35} The simplest way of synthesizing MoS₂ structures is by the hydrothermal method using ammonium thiomolybdate precursors. However the thermal decomposition

of ammonium thiomolybdate into MoS_2 , NH_3 , S is inevitable at temperatures above 800°C . The low temperature-hydrothermal growth yields MoS_2 but with some impurities or non-stoichiometric portions that are commonly denoted as amorphous MoS_x .³⁶ It has been reported that MoS_x , which can be synthesized with a cost-effective method, also showed high electrocatalytic properties in hydrodesulfurization (HDS)³⁷, oxygen reduction reaction (ORR)³⁸ and hydrogen evolution reaction (HER).³⁹⁻⁴¹ However, studies on the electron-hole transport properties of MoS_x have barely been reported in the PEC cells.

In this study, we report a p-n heterojunction of MoS_x and $\text{Ti-Fe}_2\text{O}_3$ for enhanced PEC cells fabricated via a simple hydrothermal growth and CVD synthesis. The best PEC performance of $\text{MoS}_x/\text{Ti-Fe}_2\text{O}_3$ was obtained by optimizing the thickness of the amorphous MoS_x layer in the p-n junction. $\text{MoS}_x/\text{Ti-Fe}_2\text{O}_3$ had 150% and 240% improved PEC efficiency over $\text{Ti-Fe}_2\text{O}_3$ and pristine Fe_2O_3 , respectively, which can be attributed to the reduced charge recombination and back reaction and the enhanced carrier transport to the electrolyte solution.

2. Experimental section

2.1 Preparation of $\text{Ti-Fe}_2\text{O}_3$ and $\text{MoS}_x/\text{Ti-Fe}_2\text{O}_3$

For the synthesis of Ti doped Fe_2O_3 ($\text{Ti-Fe}_2\text{O}_3$), the FTO substrate was immersed in a mixture of 2.4 μl of TiCl_3 and 40 ml of $\text{FeCl}_3 \cdot 6\text{H}_2\text{O}$ and kept in a convection oven at 100°C with a ramp rate of $1^\circ\text{C}/\text{min}$ for 4 hrs. The samples were washed with DI water and EtOH. Finally $\beta\text{-FeOOH}$ was annealed at 550°C for 1 h and 800°C for 20 min in the furnace.

To fabricate precursors of MoS_x , 0.1 wt% of $(\text{NH}_4)\text{MoS}_4$ in DMF was diluted to the proper concentration. The 10 $\mu\text{wt}\%$, 100 $\mu\text{wt}\%$ and 1000 $\mu\text{wt}\%$ of $(\text{NH}_4)\text{MoS}_4$ solution was drop-casted on $\text{Ti-Fe}_2\text{O}_3$ for 10- $\text{MoS}_x/\text{Ti-Fe}_2\text{O}_3$, 100- $\text{MoS}_x/\text{Ti-Fe}_2\text{O}_3$ and 1000- $\text{MoS}_x/\text{Ti-Fe}_2\text{O}_3$, respectively, and annealed at 100°C for 10 min. To fabricate $\text{MoS}_x/\text{Ti-Fe}_2\text{O}_3$, the $(\text{NH}_4)\text{MoS}_4$ treated $\text{Ti-Fe}_2\text{O}_3$ was placed in a quartz tube with an outer diameter of 2 inches and heated at 700°C under Ar (200 sccm) atmosphere with sulfur powder in alumina boat for 1 h.

2.2 Photoelectrochemical measurement

The PEC performance of the $\text{Ti-Fe}_2\text{O}_3$ and $\text{MoS}_x/\text{Ti-Fe}_2\text{O}_3$ electrodes was explored in a three-cell electrode system under front-side illumination of AM 1.5 G. An Ag/AgCl electrode and a Pt mesh were used as reference and counter electrodes, respectively. A solution of 1 M NaOH was used as an electrolyte. The exposed area of the working electrode was an exact value of 0.287 cm^2 . Photocurrent stability tests were carried out by measuring the photocurrent produced under chopped light irradiation (light/dark cycles of 30 s) at a bias of 1.50 V versus

RHE.). IPCE measurements were also conducted using an EQE system (Model QEX7) by PV Measurements Inc. (Boulder, Colorado) with 3 electrode system. Electrochemical impedance spectroscopy (EIS) was carried out at a frequency range from 100 kHz to 0.1 Hz using a potentiostat at 1.50 V_{RHE}. The photodegradation of methylene blue (MB) was measured by separately immersing Ti-Fe₂O₃ and MoS_x/Ti-Fe₂O₃ in 100ml of the MB solution (50mg/l in water) under illumination. After the given exposure period, the absorbance change of MB was tracked by a UV-visible spectrophotometer to compare the photocatalytic activity.

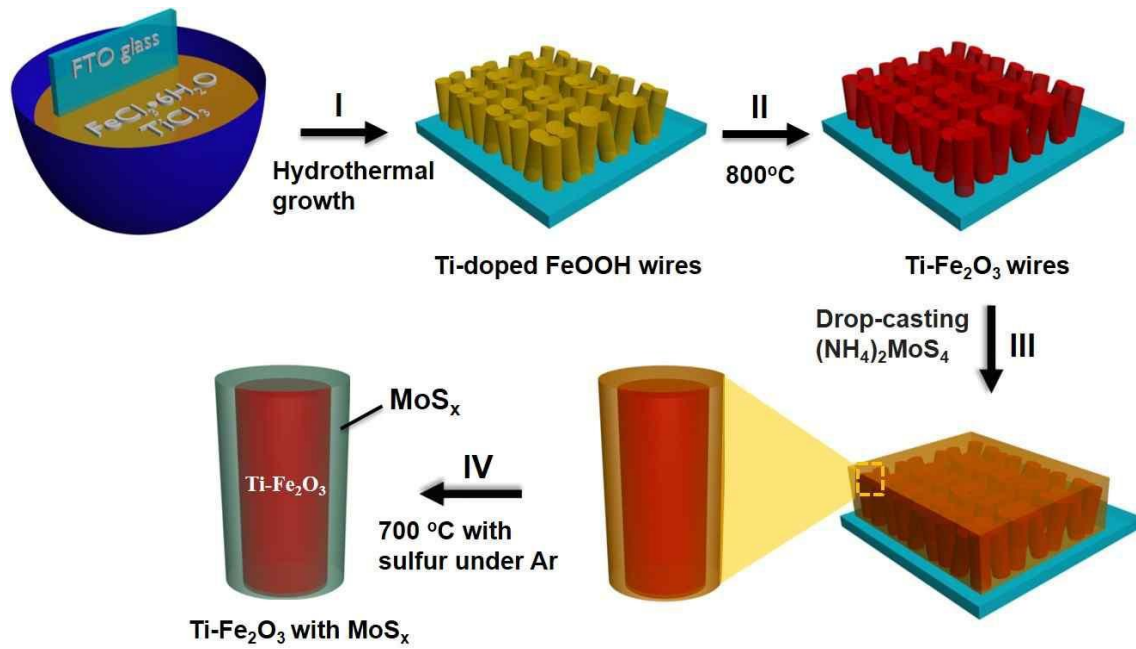


Figure 1. Scheme for fabrication of a MoS_x/Ti-Fe₂O₃ photoanode for the PEC cell. (I) Hydrothermal growth of FeOOH with TiCl₃. (II) Annealing of Ti doped FeOOH at 800°C for 20 min in the furnace. (III) Drop-casting of (NH₄)₂MoS₄ on Ti-Fe₂O₃. (IV) Annealing of Ti-Fe₂O₃/(NH₄)₂MoS₄ at 700°C for 1 h with sulfur powder sitting aside in the CVD chamber under an Ar gas condition.

3. Results and Discussion

The $\text{MoS}_x/\text{Ti-Fe}_2\text{O}_3$ photoanode for the PEC cells was fabricated by a combination of the hydrothermal growth method and CVD growth method as shown in Figure 1. First, a thin layer of Ti-doped $\beta\text{-FeOOH}$ nanowires (in yellow) was grown on the pre-cleaned FTO glass substrate by dipping in a mixture of $\text{FeCl}_3 \cdot 6\text{H}_2\text{O}$ and TiCl_3 solutions. To convert Ti-doped $\beta\text{-FeOOH}$ to $\text{Ti-Fe}_2\text{O}_3$, $\beta\text{-FeOOH}/\text{FTO}$ was two-step heated in the furnace at 550°C for 1 h and 800°C for 20 min. The high temperature annealing is known to enhance the PEC performance of $\text{Ti-Fe}_2\text{O}_3$, due to the creation of improved crystallinity of $\alpha\text{-Fe}_2\text{O}_3$ as confirmed by XRD (Figure S1). To deposit MoS_x on the surface of $\text{Ti-Fe}_2\text{O}_3$, the $(\text{NH}_4)_2\text{MoS}_4$ solution was drop-casted on $\text{Ti-Fe}_2\text{O}_3$ and the sample was placed on the hotplate at 100°C . The prepared $(\text{NH}_4)_2\text{MoS}_4/\text{Ti-Fe}_2\text{O}_3$ sample was annealed at 700°C for 1 h in Ar atmosphere CVD conditions with sulfur powders in an alumina boat which allowed it to be evaporated for the conversion into $\text{MoS}_x/\text{Ti-Fe}_2\text{O}_3$. Figure 2a is the TEM image of Ti-doped Fe_2O_3 with a lattice spacing of 0.25 nm, which corresponded to the (110) lattice of $\alpha\text{-Fe}_2\text{O}_3$. Figures 2b-2d show the variation in the thickness of the MoS_x layer coated on the surface of $\text{Ti-Fe}_2\text{O}_3$ after the CVD reaction. The phase of the thin MoS_x layer was amorphous whereas a clear surface of $\text{Ti-Fe}_2\text{O}_3$ with the lattice spacing of 0.25 nm was observed, as can be seen in Figure 2b (The further confirmation of MoS_x will be discussed in the following section). As shown in the TEM image, the thickness of MoS_x increased by increasing the concentration of the precursor solution, $(\text{NH}_4)_2\text{MoS}_4$, from 10 $\mu\text{wt}\%$ to 1000 $\mu\text{wt}\%$ (10- MoS_x , 100- MoS_x , and 1000- MoS_x was designated accordingly). Measurements of 1 nm, 3.25 nm, and 18.5 nm of the MoS_x layer on the surface of $\alpha\text{-Fe}_2\text{O}_3$ were observed in 10- $\text{MoS}_x/\text{Ti-Fe}_2\text{O}_3$ (Figure 2b), 100- $\text{MoS}_x/\text{Ti-Fe}_2\text{O}_3$ (Figure 2c) and 1000- $\text{MoS}_x/\text{Ti-Fe}_2\text{O}_3$ (Figure 2d), respectively. We found that the one with the uniform distribution of the thinnest MoS_x layer (10- $\text{MoS}_x/\text{Ti-Fe}_2\text{O}_3$) exhibited the best PEC performance, as will be illustrated in Figure 5.

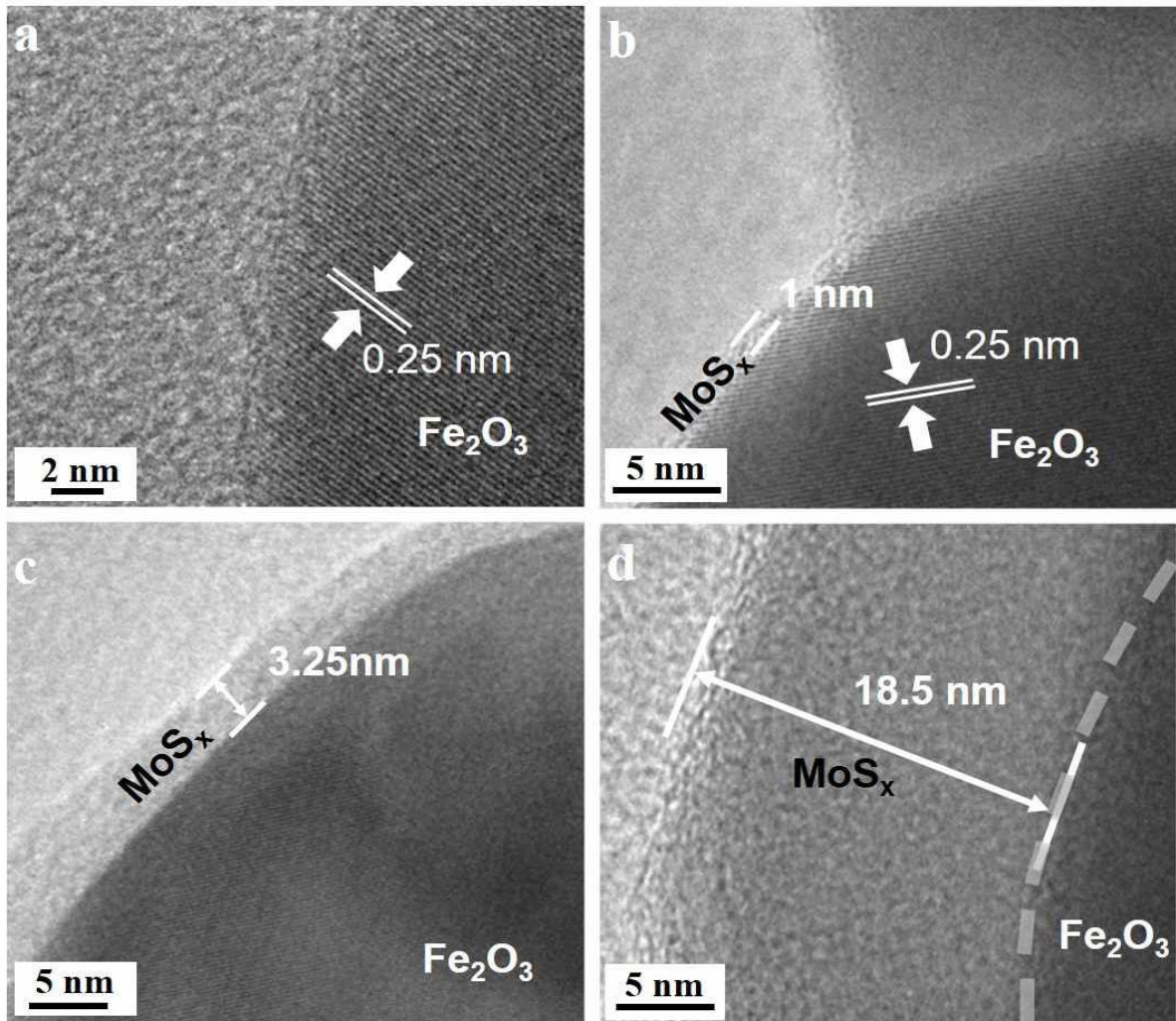


Figure 2. TEM images of (a) Ti-doped hematite ($\text{Ti-Fe}_2\text{O}_3$), (b) 10- $\text{MoS}_x/\text{Ti-Fe}_2\text{O}_3$, (c) 100- $\text{MoS}_x/\text{Ti-Fe}_2\text{O}_3$ and (d) 1000- $\text{MoS}_x/\text{Ti-Fe}_2\text{O}_3$. The thickness of the MoS_x layer was controlled by changing the concentration of the $(\text{NH}_4)_2\text{MoS}_4$ solution from 10 $\mu\text{wt}\%$ to 1000 $\mu\text{wt}\%$.

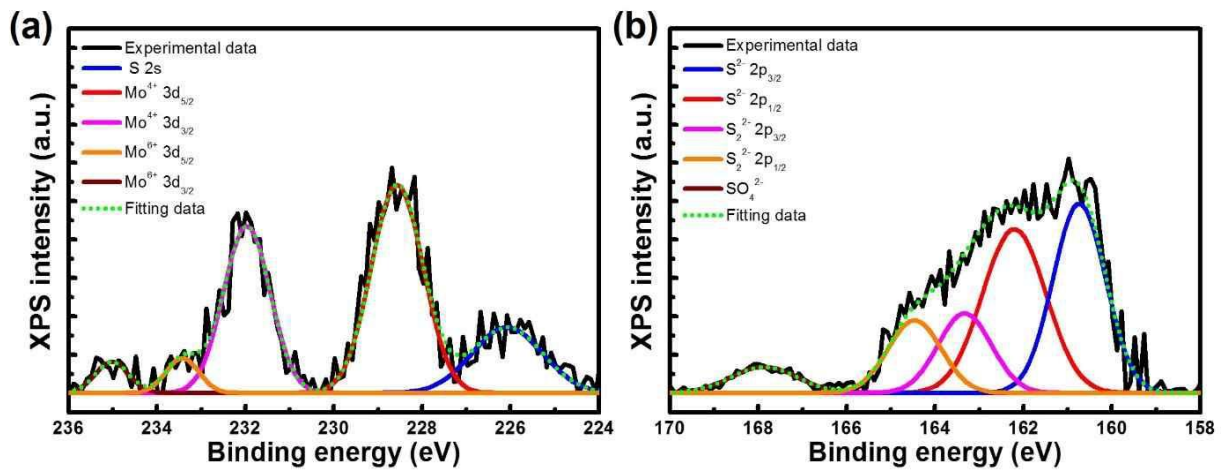


Figure 3. X-Ray photoelectron spectroscopy scans for (a) Mo and (b) S binding energies of amorphous MoS_x.

To investigate the composition of MoS_x more clearly, X-ray photoelectron spectroscopy (XPS) analysis and energy dispersive X-ray spectrometer (EDX) were performed. The XPS peaks at 226.1 eV, 228.6 eV and 231.9 eV in Figure 3(a) correspond to S 2s, Mo⁴⁺ 3d_{5/2}, and Mo⁴⁺ 3d_{3/2}, respectively.²⁶ The small Mo⁶⁺ peaks at the 233.4 eV and 235.0 eV represent the presence of a trace amount of MoO₃ at the surface of MoS_x/Ti-Fe₂O₃ as described in other studies.²⁷⁻²⁸ The S 2p spectrum of MoS_x was split into two S doublets (S²⁻ and S₂²⁻), and the SO₄²⁻ peaks are shown in Figure 3(b). The XPS peaks at 160.7 eV and 162.2 eV are attributed to S²⁻, and 163.3 eV and 164.5 eV are attributed to S₂²⁻. The SO₄²⁻ peak at a higher binding energy indicates a side product of MoO₃ during the MoS_x formation on the hematite substrate.²⁷ However, MoO₃ does not affect the PEC performance since it is already etched away in the pre-treatment NaOH solution and does not remain in the final product.⁴⁵

The EDX mapping data of MoS_x/Ti-Fe₂O₃ as seen in Figure S4 confirm the uniform distribution of Fe, O, S and Mo on the hematite nanorod. It should be noted that the uniformly-coated MoS_x layer can protect Fe₂O₃ from reductions by generated oxygen gas which occur at the surface of the MoS_x layer and help the facile hole transfer driven by the electrostatic field at the p-n junction of MoS_x and Ti-Fe₂O₃. The optical band gap and valence band maximum (VBM) was obtained to specify the creation of the p-n junction of MoS_x/Ti-Fe₂O₃, as shown in the inset of Figure 4(a) and Figure S5, respectively. To confirm the electrical property of the MoS_x film, a Mott-Schottky plot was obtained at an AC frequency of 10kHz in the dark condition with 0.5M NaSO₄ electrolyte. The MoS_x film showed a negative slope in the Mott-Schottky plot, indicating p-type behavior, as shown in Figure S6.^{34, 35} The slightly increased absorbance of MoS_x/Ti-Fe₂O₃ over that of Ti-Fe₂O₃ was detected in the range of 430-550 nm. This can be attributed to the absorption of MoS_x in this range as shown in Figure S7. The Tauc plot in the inset of Figure 4(a) provides the optical band gap of MoS_x and Ti-Fe₂O₃ with 2.07 eV and 2.1 eV, respectively, which is in agreement with the previous reports.^{24, 46} Since the VBM is 0.78 eV for MoS_x and 1.65 eV for Ti-Fe₂O₃, as obtained in Figure S5, the band positions of MoS_x/Ti-Fe₂O₃ can be drawn as shown in Figure 4(b). The electron-hole transfer mechanism behind the p-n junction of MoS_x and Ti-Fe₂O₃ is as follows: When MoS_x and Ti-Fe₂O₃ were in contact, band bending occurred to get an equilibrium of Fermi level, which created the p-n junction. Upon light excitation, electrons were excited from the valence band (VB) to the conduction band (CB) of Ti-doped Fe₂O₃ and MoS_x.

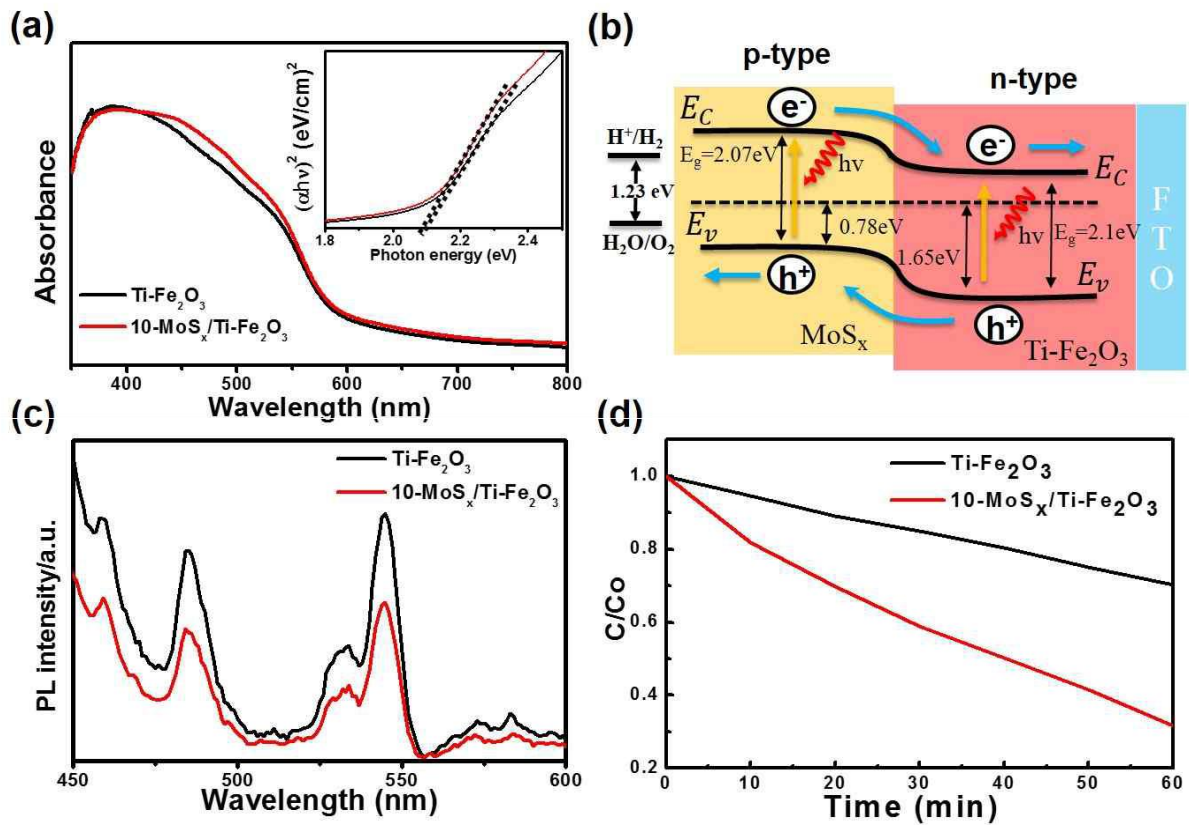


Figure 4. (a) UV/Vis absorbance of Ti-Fe₂O₃ and 10-MoS_x/Ti-Fe₂O₃. The inset in the Tauc plot $(\alpha h\nu)^2$ as a function of photon energy presents the optical bandgap (E_g) of 2.1 eV and 2.07 eV for Ti-Fe₂O₃ and MoS_x/Ti-Fe₂O₃, respectively. (b) Schematic illustration of band energies and charge transfer process at the p-n junction of MoS_x/Ti-Fe₂O₃. (c) The PL spectra of Ti-Fe₂O₃ and 10-MoS_x/Ti-Fe₂O₃. (d) The photodegradation of methylene blue by Ti-Fe₂O₃ and 10-MoS_x/Ti-Fe₂O₃ at 1.5V_{RHE}.

The electron from CB of MoS_x was then transferred to CB of Ti-Fe₂O₃ due to the energy level difference as shown in Figure 4b. The holes from VB of Ti-Fe₂O₃ were transferred to VB of MoS_x driven by the electrostatic field and reacted with OH⁻ to create O₂ gas, whereas electrons that had arrived at the Pt counter electrode through FTO glass generated the H₂ gas. Therefore, the internal electrostatic field in the space charge region of the p-n junction region can promote the extraction of the photo-induced carriers, which leads to increased O₂ and H₂ generation in the PEC cell by providing effectively separated pathways of electrons and holes. The charge trapping and recombination of photoinduced electron-hole pairs in the semiconductor were measured by the photoluminescence (PL) spectrum. The PL intensity of 10-MoS_x/Ti-Fe₂O₃ was much weaker than that of Ti-Fe₂O₃ in the range from 450 nm to 600 nm under excitation at 400 nm as shown in Figure 4(c). This result indicates the fast electron-hole transfer between Ti-Fe₂O₃ and MoS_x, which can be attributed to the presence of the p-n junction in the MoS_x/Ti-Fe₂O₃. The photodegradation of methylene blue (MB) provides more direct evidence of the degree of electron-hole recombination in the semiconductor, because MB reacts with the holes accumulated at the surface of the semiconductor under illumination.⁴⁷ Each photoanode (Ti-Fe₂O₃ and 10-MoS_x/Ti-Fe₂O₃) was immersed in 100 ml of MB solution (50mg/ml in water) and shined by an AM 1.5 solar spectrum at 1.5 V_{RHE}. After the given exposure period, the absorbance change of MB was tracked by a UV-Visible spectrophotometer to compare the photocatalytic activity of the photoanodes. As shown in Figure 4(d), the concentration of MB (C/C₀) for 10-MoS_x/Ti-Fe₂O₃ was lower than that of Ti-Fe₂O₃, implying an enhanced hole transfer process to the MB solution due to the suppressed recombination of excitons in the 10-MoS_x/Ti-Fe₂O₃ heterojunction.

Figure 5 (a) displays the photocurrent-potential curves of Ti-Fe₂O₃, 10-MoS_x/Ti-Fe₂O₃, 100-MoS_x/Ti-Fe₂O₃ and 1000-MoS_x/Ti-Fe₂O₃ under one-sun (100 mW cm⁻²) illumination with the Ag/AgCl reference electrode, platinum counter electrode and 1 M NaOH (PH 13.6) solution of the electrolyte. 10-MoS_x/Ti-Fe₂O₃ showed respectively 150% and 240% higher photocurrent density (3.03 mA cm⁻²) than Ti-Fe₂O₃ (2.00 mA cm⁻²) and pristine α-Fe₂O₃ (Figure S8) at RHE 1.50 V. It should be noted that the thickness of the MoS_x sheets did affect the PEC performance. As the thickness of MoS_x increased from 1 nm to 18.5 nm, the photocurrent density decreased from 3.03 mA cm⁻² to 0.5 mA cm⁻² at RHE 1.50 V as shown in Figure 5(a). This significant decrease in photocurrent with the increase in MoS_x layer thickness can be attributed to the trade-off between the positive role of MoS_x for the creation of the p-n junction and the low

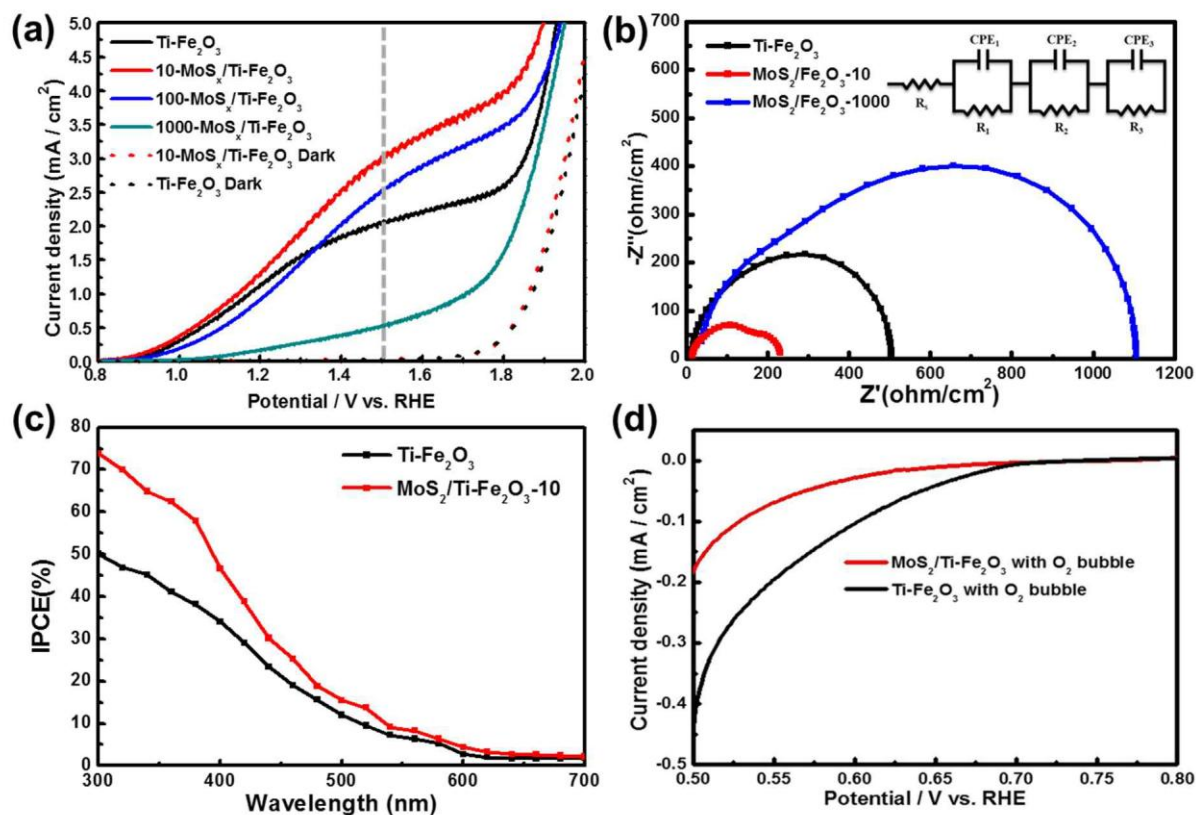


Figure 5. (a) I-V curve of Ti-Fe₂O₃, 10-MoS_x/Ti-Fe₂O₃, 100-MoS_x/Ti-Fe₂O₃ and 1000-MoS_x/Ti-Fe₂O₃, respectively. (b) Nyquist plots measured under illumination of Ti-Fe₂O₃, 10-MoS_x/Ti-Fe₂O₃, 100-MoS_x/Ti-Fe₂O₃ and 1000-MoS_x/Ti-Fe₂O₃ measured at 1.50 V vs. RHE. The inset is an equivalent circuit model for fitting the experimental data. (c) IPCE curve of Ti-Fe₂O₃ and 10-MoS_x/Ti-Fe₂O₃. (d) Dark current of Ti-Fe₂O₃ and MoS_x/Ti-Fe₂O₃ by the O₂ reduction reaction with O₂ bubbling in 1M NaOH.

electrical conductivity of the amorphous MoS_x layer where the holes are trapped.

To elucidate the thickness effect of MoS_x and the charge transfer process at the electrolyte/MoS_x/Ti-Fe₂O₃, electrochemical impedance spectroscopy (EIS) was measured as shown in Figure 5(b). The EIS was measured at a frequency range from 100 kHz to 0.1 Hz at 1.50 V_{RHE} in a 1 M NaOH electrolyte under A.M. 1.5 illumination. The Nyquist plots of photoanodes were interpreted by the circuit shown in the inset of Figure 5(b) which is composed of a 2RC or 3RC circuit and summarized in Table S1. The equivalent circuit consists of a sheet resistance of Ti-Fe₂O₃/FTO, R_s, a space charge capacitance of the bulk hematite, C₁, a capacitance of interface between MoS_x/Ti-Fe₂O₃, C₂, a space charge capacitance of interface between electrolyte/MoS_x or electrolyte/Ti-Fe₂O₃, C₃, the resistance of the inside of bulk Ti-Fe₂O₃, R₁, the charge transfer resistance between MoS_x/Ti-Fe₂O₃, R₂, and the charge transfer resistance between the electrolyte/MoS_x or electrolyte/Ti-Fe₂O₃, R₃.^{48,49}

The R_s, the left onset point in the Nyquist plot, commonly displays the sheet resistance in the PEC system. As can be seen in Figure 5(b), the presence of the additional MoS_x layer did not change the sheet resistance of MoS_x/Ti-Fe₂O₃ from that of Ti-Fe₂O₃. The R₁ refers to the recombination resistance inside bulk Fe₂O₃. 10-MoS_x/Ti-Fe₂O₃ had the smallest R₁ and highest C₁ value compared with other photoanodes. The low R₁ value in 10-MoS_x/Ti-Fe₂O₃ can be attributed to the reduced recombination and easy extraction of holes from Ti-Fe₂O₃ through the thin (~1 nm) MoS_x layer in the p-n heterojunction. However, 1000-MoS_x/Ti-Fe₂O₃ exhibited the highest R₁ and lowest C₁ which indicates the thick MoS_x layer disturbed hole-extraction from Ti-Fe₂O₃ and increased the recombination in the Ti-Fe₂O₃. The resistance between MoS_x/Ti-Fe₂O₃ (R₂) also increased with an increase in the thickness of the MoS_x layers as shown Table S1. It is clear that even at a high potential (1.50 V_{REH}), the hole extraction through thick MoS_x layers was difficult due to high resistance through the amorphous thick (~18.5 nm) MoS_x layer.

Water oxidation that occurs by the reaction between water and holes from the photoanode in water splitting generally showed the largest charge transfer resistance (R₃), and a double layer capacitance (C₃) can be observed at the interface of the electrolyte/photoanode. The R₃ value of the 10-MoS_x/Ti-Fe₂O₃ sample was 4.45 times lower than that of Ti-Fe₂O₃, which can be attributed to the superior photocatalytic property and easy hole extraction through MoS_x and reduced recombination. On the other hand, 1000-Ti-Fe₂O₃ with the 18.5 nm thick MoS_x layer had a high R₃ value and a low C₃ value, which demonstrates the poor water oxidation behaviors due to the inefficient hole extraction through the amorphous thick MoS_x layer.

Figure 5(c) shows the incident photon-to-current efficiency (IPCE) of 10-MoS_x/Ti-Fe₂O₃ and Ti-Fe₂O₃ according to the incident light wavelength. The IPCE data were measured at an applied potential of 1.50 V (vs. RHE) in an 1 M NaOH solution. The IPCE value of the 10-MoS_x/Ti-Fe₂O₃ at 380 nm was 58.15%, about 20% greater than Ti-Fe₂O₃, and showed overall higher values in the overall wavelength ranges, which agrees with the previous data.

It is known that a back reaction, a reduction of created oxygen gases at the hematite/O₂ interface, degrades the PEC performance by capturing the photo-excited electrons. Dapeng et al. reported an efficient way to reduce the surface corrosion caused by the back reaction.²⁹ Even the very thin TiO₂ layer on the Ti-doped α -Fe₂O₃ prevented direct contact of O₂ with α -Fe₂O₃ surface, which in turn hindered the reduction of the O₂ with excited electrons in α -Fe₂O₃. As shown in Figure 5 (d), the dark current of pristine Ti-Fe₂O₃ and MoS_x/Ti-Fe₂O₃ were measured in the O₂-saturated 1 M NaOH solution under oxygen gas bubbling in the range of 0.50 V_{RHE} and 0.80 V_{RHE}. The high dark current density was observed for Ti-Fe₂O₃ due to the oxygen reduction reaction, whereas the dark current of MoS_x/Ti-Fe₂O₃ was greatly reduced. Therefore, the MoS_x thin layers efficiently protected the surface of Ti-Fe₂O₃ from the back reaction and contributed to the enhanced PEC performance of Ti-Fe₂O₃. Preventing photo-corrosion and instability of the photoanode in the electrolyte solution is a critical issue for securing the durability of the PEC cells. The cobalt-phosphate (Co-Pi) has been widely used to enhance the PCE performance and stability of Fe₂O₃, because a thin layer of Co-Pi reduces the chance of direct contact between the surface of the final electrode and the electrolyte, exhibiting superior oxygen evolution performance.³⁰ In order to address the instability of MoS_x and Fe₂O₃ in the electrolyte solution, Co-Pi passivation layers were deposited by using photo-assisted electrodeposition, as reported elsewhere on the surface of MoS_x/Ti-Fe₂O₃.³¹ As shown in the Figure 6(a), Co-Pi/10-MoS_x/Ti-Fe₂O₃ was 3.23 mA/cm² at 1.50 V_{RHE} and the cathodic shift of onset potential (0.85 V_{RHE}), which indicates enhanced PEC performance compared with that of MoS_x/Ti-Fe₂O₃ and Ti-Fe₂O₃. To observe the stability of the photoanode over time, the chronoamperometric I-t curve of Co-Pi/10-MoS_x/Ti-Fe₂O₃ was measured at RHE 1.23V with a chopped illumination of A.M 1.5 under 30 s exposure on/off cycles up to 900 s in 1 M NaOH solution. The enhanced stability comes from the effective separation between the alkaline-weak-MoS_x³² and NaOH electrolyte due to a thin Co-Pi layer on the MoS_x.

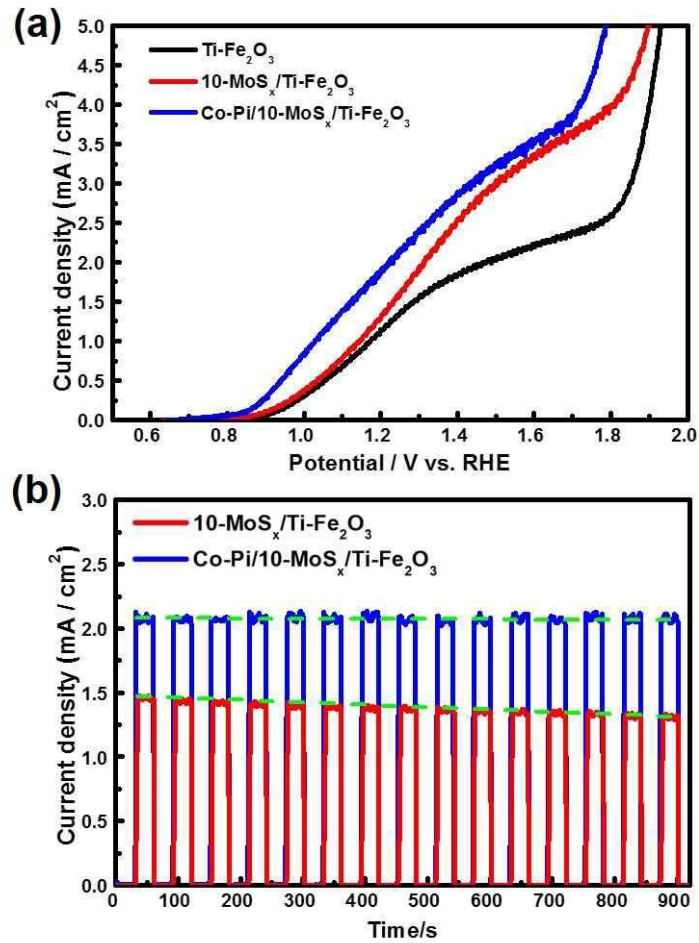


Figure 6. (a) I-V curve of Ti-Fe₂O₃, 10-MoS_x/Ti-Fe₂O₃, Co-Pi/10-MoS_x/Ti-Fe₂O₃, respectively. (b) I-t curve of Co-Pi/10-MoS_x/Ti-Fe₂O₃.

4. Conclusion

In conclusion, we demonstrated the positive effect of the creation of the p-n junction of MoS_x/Ti-Fe₂O₃ in PEC performance fabricated via a simple hydrothermal growth and drop-casting method due to facile electron-hole transfer driven by an electrostatic field. The optimized Ti-Fe₂O₃ with thin MoS_x layer (~1 nm) showed a photocurrent density of 3.03 mA/cm² at RHE 1.50 V, which is 150% and 240% higher than that of Ti-Fe₂O₃ and α -Fe₂O₃, respectively. The instability of the MoS_x layer in an alkaline solution was addressed by depositing a thin Co-Pi layer on the MoS_x. All the data, including XPS, TEM, IPCE, PL, EIS and chronoamperometric I-t curve clearly confirmed the enhanced performance of MoS_x/Ti-Fe₂O₃ by the creation of a p-n junction with a facile electron-hole transport pathway.

5. References

1. Fujishima, A.; Honda, K., ELECTROCHEMICAL PHOTOLYSIS OF WATER AT A SEMICONDUCTOR ELECTRODE. *Nature* 1972, 238 (5358), 37-+.
2. Khan, S. U. M.; Al-Shahry, M.; Ingler, W. B., Efficient Photochemical Water Splitting by a Chemically Modified n-TiO₂. *Science* 2002, 297 (5590), 2243-2245.
3. Park, J. H.; Kim, S.; Bard, A. J., Novel Carbon-Doped TiO₂ Nanotube Arrays with High Aspect Ratios for Efficient Solar Water Splitting. *Nano Lett.* 2005, 6 (1), 24-28.
4. Ahn, H. J.; Kim, M. J.; Kim, K.; Kwak, M. J.; Jang, J. H., Optimization of Quantum Dot-Sensitized Photoelectrode for Realization of Visible Light Hydrogen Generation. *Small* 2014, 10 (12), 2325-2330.
5. Li, Z.; Luo, W.; Zhang, M.; Feng, J.; Zou, Z., Photoelectrochemical cells for solar hydrogen production: current state of promising photoelectrodes, methods to improve their properties, and outlook. *Energy Environ. Sci.* 2013, 6 (2), 347-370.
6. Luo, J.; Ma, L.; He, T.; Ng, C. F.; Wang, S.; Sun, H.; Fan, H. J., TiO₂/(CdS, CdSe, CdSeS) Nanorod Heterostructures and Photoelectrochemical Properties. *J. Phys. Chem. C* 2012, 116 (22), 11956-11963.
7. Cesar, I.; Kay, A.; Gonzalez Martinez, J. A.; Grätzel, M., Translucent Thin Film Fe₂O₃ Photoanodes for Efficient Water Splitting by Sunlight: Nanostructure-Directing Effect of Si-Doping. *J. Am. Chem. Soc.* 2006, 128 (14), 4582-4583.
8. Ng, Y. H.; Iwase, A.; Kudo, A.; Amal, R., Reducing Graphene Oxide on a Visible-Light BiVO₄ Photocatalyst for an Enhanced Photoelectrochemical Water Splitting. *J. Phys. Chem. Lett.* 2010, 1 (17), 2607-2612.
9. Su, J.; Guo, L.; Bao, N.; Grimes, C. A., Nanostructured WO₃/BiVO₄ Heterojunction Films for Efficient Photoelectrochemical Water Splitting. *Nano Lett.* 2011, 11 (5), 1928-1933.
10. Gao, R.; Hu, L.; Chen, M.; Wu, L., Controllable Fabrication and Photoelectrochemical Property of Multilayer Tantalum Nitride Hollow Sphere-Nanofilms. *Small* 2014, 10 (15), 3038-3044.
11. Ahn, H.-J.; Kwak, M.-J.; Lee, J.-S.; Yoon, K.-Y.; Jang, J.-H., Nanoporous hematite structures to overcome short diffusion lengths in water splitting. *J. Mater. Chem. A* 2014, 2 (47), 19999-20003.
12. Sivula, K.; Le Formal, F.; Grätzel, M., Solar Water Splitting: Progress Using Hematite (α -Fe₂O₃) Photoelectrodes. *ChemSusChem*. 2011, 4 (4), 432-449.
13. Hu, Y.-S.; Kleiman-Shwarscstein, A.; Forman, A. J.; Hazen, D.; Park, J.-N.; McFarland, E. W., Pt-Doped α -Fe₂O₃ Thin Films Active for Photoelectrochemical Water Splitting. *Chem. Mater.* 2008, 20 (12), 3803-3805.
14. Lindgren, T.; Wang, H.; Beermann, N.; Vayssieres, L.; Hagfeldt, A.; Lindquist, S.-E., Aqueous

- photoelectrochemistry of hematite nanorod array. *Sol. Energy Mater. Sol. Cells* 2002, 71 (2), 231-243.
16. Glasscock, J. A.; Barnes, P. R. F.; Plumb, I. C.; Savvides, N., Enhancement of Photoelectrochemical Hydrogen Production from Hematite Thin Films by the Introduction of Ti and Si. *J. Phys. Chem. C* 2007, 111 (44), 16477-16488.
 17. Barroso, M.; Pendlebury, S. R.; Cowan, A. J.; Durrant, J. R., Charge carrier trapping, recombination and transfer in hematite (α -Fe₂O₃) water splitting photoanodes. *Chem. Sci.* 2013, 4 (7), 2724-2734.
 18. Lukowski, M. A.; Jin, S., Improved Synthesis and Electrical Properties of Si-Doped α -Fe₂O₃ Nanowires. *J. Phys. Chem. C* 2011, 115 (25), 12388-12395.
 19. Hu, Y.-S.; Kleiman-Shwarsstein, A.; Stucky, G. D.; McFarland, E. W., Improved photoelectrochemical performance of Ti-doped α -Fe₂O₃ thin films by surface modification with fluoride. *Chem. Commun.* 2009, (19), 2652-2654.
 20. Lee, K. K.; Deng, S.; Fan, H. M.; Mhaisalkar, S.; Tan, H. R.; Tok, E. S.; Loh, K. P.; Chin, W. S.; Sow, C. H., α -Fe₂O₃ nanotubes-reduced graphene oxide composites as synergistic electrochemical capacitor materials. *Nanoscale* 2012, 4 (9), 2958-2961.
 21. Xie, H.; Li, Y.; Jin, S.; Han, J.; Zhao, X., Facile Fabrication of 3D-Ordered Macroporous Nanocrystalline Iron Oxide Films with Highly Efficient Visible Light Induced Photocatalytic Activity. *J. Phys. Chem. C* 2010, 114 (21), 9706-9712.
 22. Qin, D.-D.; Tao, C.-L.; In, S.-i.; Yang, Z.-Y.; Mallouk, T. E.; Bao, N.; Grimes, C. A., Facile Solvothermal Method for Fabricating Arrays of Vertically Oriented α -Fe₂O₃ Nanowires and Their Application in Photoelectrochemical Water Oxidation. *Energy Fuels* 2011, 25 (11), 5257-5263.
 23. Zhong, D. K.; Gamelin, D. R., Photoelectrochemical Water Oxidation by Cobalt Catalyst ("Co-Pi")/ α -Fe₂O₃ Composite Photoanodes: Oxygen Evolution and Resolution of a Kinetic Bottleneck. *J. Am. Chem. Soc.* 2010, 132 (12), 4202-4207.
 24. Kim, J. Y.; Magesh, G.; Youn, D. H.; Jang, J.-W.; Kubota, J.; Domen, K.; Lee, J. S., Single-crystalline, wormlike hematite photoanodes for efficient solar water splitting. *Sci. Rep.* 2013, 3, 2681.
 25. Lin, Y.; Xu, Y.; Mayer, M. T.; Simpson, Z. I.; McMahon, G.; Zhou, S.; Wang, D., Growth of p-Type Hematite by Atomic Layer Deposition and Its Utilization for Improved Solar Water Splitting. *J. Am. Chem. Soc.* 2012, 134 (12), 5508-5511.
 26. Hou, Y.; Zuo, F.; Dagg, A.; Feng, P., Visible Light-Driven α -Fe₂O₃ Nanorod/Graphene/BiV_{1-x}MoxO₄ Core/Shell Heterojunction Array for Efficient Photoelectrochemical Water Splitting. *Nano Lett.* 2012, 12 (12), 6464-6473.
 27. Li, J.; Meng, F.; Suri, S.; Ding, W.; Huang, F.; Wu, N., Photoelectrochemical performance enhanced

- by a nickel oxide-hematite p-n junction photoanode. *Chem. Commun.* 2012, 48 (66), 8213-8215.
28. Yu, Y.-X.; Ouyang, W.-X.; Liao, Z.-T.; Du, B.-B.; Zhang, W.-D., Construction of ZnO/ZnS/CdS/CuInS₂ Core-Shell Nanowire Arrays via Ion Exchange: p-n Junction Photoanode with Enhanced Photoelectrochemical Activity under Visible Light. *ACS Appl. Mater. Interfaces* 2014, 6 (11), 8467-8474.
 29. Splendiani, A.; Sun, L.; Zhang, Y.; Li, T.; Kim, J.; Chim, C.-Y.; Galli, G.; Wang, F., Emerging Photoluminescence in Monolayer MoS₂. *Nano Lett.* 2010, 10 (4), 1271-1275.
 30. Yin, Z.; Li, H.; Li, H.; Jiang, L.; Shi, Y.; Sun, Y.; Lu, G.; Zhang, Q.; Chen, X.; Zhang, H., Single-Layer MoS₂ Phototransistors. *ACS Nano* 2011, 6 (1), 74-80.
 31. He, Q.; Zeng, Z.; Yin, Z.; Li, H.; Wu, S.; Huang, X.; Zhang, H., Fabrication of Flexible MoS₂ Thin-Film Transistor Arrays for Practical Gas-Sensing Applications. *Small* 2012, 8 (19), 2994-2999.
 32. Nguyen, M.; Tran, P. D.; Pramana, S. S.; Lee, R. L.; Batabyal, S. K.; Mathews, N.; Wong, L. H.; Graetzel, M., In situ photo-assisted deposition of MoS₂ electrocatalyst onto zinc cadmium sulphide nanoparticle surfaces to construct an efficient photocatalyst for hydrogen generation. *Nanoscale* 2013, 5 (4), 1479-1482.
 33. Fontana, M.; Deppe, T.; Boyd, A. K.; Rinzan, M.; Liu, A. Y.; Paranjape, M.; Barbara, P., Electron-hole transport and photovoltaic effect in gated MoS₂ Schottky junctions. *Sci. Rep.* 2013, 3, 1634.
 34. Liu, Y.; Yu, Y.-X.; Zhang, W.-D., MoS₂/CdS Heterojunction with High Photoelectrochemical Activity for H₂ Evolution under Visible Light: The Role of MoS₂. *J. Phys. Chem. C* 2013, 117 (25), 12949-12957.
 35. Meng, F.; Li, J.; Cushing, S. K.; Zhi, M.; Wu, N., Solar Hydrogen Generation by Nanoscale p-n Junction of p-type Molybdenum Disulfide/n-type Nitrogen-Doped Reduced Graphene Oxide. *J. Am. Chem. Soc.* 2013, 135 (28), 10286-10289.
 36. Liu, K.-K.; Zhang, W.; Lee, Y.-H.; Lin, Y.-C.; Chang, M.-T.; Su, C.-Y.; Chang, C.-S.; Li, H.; Shi, Y.; Zhang, H.; Lai, C.-S.; Li, L.-J., Growth of Large-Area and Highly Crystalline MoS₂ Thin Layers on Insulating Substrates. *Nano Lett.* 2012, 12 (3), 1538-1544.
 37. Salmeron, M.; Somorjai, G. A.; Wold, A.; Chianelli, R.; Liang, K. S., The adsorption and binding of thiophene, butene and H₂S on the basal plane of MoS₂ single crystals. *Chem. Phys. Lett.* 1982, 90 (2), 105-107.
 38. Ahmed, S. M.; Gerischer, H., Influence of crystal surface orientation on redox reactions at semiconducting MoS₂. *Electrochim. Acta* 1979, 24 (6), 705-711.
 39. Chang, Y.-H.; Wu, F.-Y.; Chen, T.-Y.; Hsu, C.-L.; Chen, C.-H.; Wiryo, F.; Wei, K.-H.; Chiang, C.-Y.; Li, L.-J., Three-Dimensional Molybdenum Sulfide Sponges for Electrocatalytic Water Splitting. *Small* 2014, 10 (5), 895-900.
 40. Hinnemann, B.; Moses, P. G.; Bonde, J.; Jørgensen, K. P.; Nielsen, J. H.; Horch, S.; Chorkendorff,

- I.; Nørskov, J. K., Biomimetic Hydrogen Evolution: MoS₂ Nanoparticles as Catalyst for Hydrogen Evolution. *J. Am. Chem. Soc.* 2005, 127 (15), 5308-5309.
41. Jaramillo, T. F.; Jørgensen, K. P.; Bonde, J.; Nielsen, J. H.; Horch, S.; Chorkendorff, I., Identification of Active Edge Sites for Electrochemical H₂ Evolution from MoS₂ Nanocatalysts. *Science* 2007, 317 (5834), 100-102.
 42. Tang, M. L.; Grauer, D. C.; Lassalle-Kaiser, B.; Yachandra, V. K.; Amirav, L.; Long, J. R.; Yano, J.; Alivisatos, A. P., Structural and Electronic Study of an Amorphous MoS₃ Hydrogen-Generation Catalyst on a Quantum-Controlled Photosensitizer. *Angew. Chem. Int. Ed.* 2011, 50 (43), 10203-10207.
 43. Smith, A. J.; Chang, Y.-H.; Raidongia, K.; Chen, T.-Y.; Li, L.-J.; Huang, J., Molybdenum Sulfide Supported on Crumpled Graphene Balls for Electrocatalytic Hydrogen Production. *Adv. Energy Mater.* 2014, 4 (14).
 44. Lin, Y.-C.; Zhang, W.; Huang, J.-K.; Liu, K.-K.; Lee, Y.-H.; Liang, C.-T.; Chu, C.-W.; Li, L.-J., Wafer-scale MoS₂ thin layers prepared by MoO₃ sulfurization. *Nanoscale* 2012, 4 (20), 6637-6641.
 45. Zeng, H. C., Chemical Etching of Molybdenum Trioxide: A New Tailor-Made Synthesis of MoO₃ Catalysts. *Inorg. Chem.* 1998, 37 (8), 1967-1973.
 46. Bhattacharya, R. N.; Lee, C. Y.; Pollak, F. H.; Schleich, D. M., Optical study of amorphous MoS₃: Determination of the fundamental energy gap. *J. Non-Cryst. Solids* 1987, 91 (2), 235-242.
 47. Houas, A.; Lachheb, H.; Ksibi, M.; Elaloui, E.; Guillard, C.; Herrmann, J.-M., Photocatalytic degradation pathway of methylene blue in water. *Appl. Catal. B: Environ* 2001, 31 (2), 145-157.
 48. Young Kim, J.; Jang, J.-W.; Hyun Youn, D.; Yul Kim, J.; Sun Kim, E.; Sung Lee, J., Graphene-carbon nanotube composite as an effective conducting scaffold to enhance the photoelectrochemical water oxidation activity of a hematite film. *RSC Advances* 2012, 2 (25), 9415-9422.
 49. Zandi, O.; Klahr, B. M.; Hamann, T. W., Highly photoactive Ti-doped α-Fe₂O₃ thin film electrodes: resurrection of the dead layer. *Energy Environ. Sci.* 2013, 6 (2), 634-642.
 50. Cao, D.; Luo, W.; Feng, J.; Zhao, X.; Li, Z.; Zou, Z., Cathodic shift of onset potential for water oxidation on a Ti⁴⁺ doped Fe₂O₃ photoanode by suppressing the back reaction. *Energy Environ. Sci.* 2014, 7 (2), 752-759.
 51. Zhong, D. K.; Cornuz, M.; Sivula, K.; Gratzel, M.; Gamelin, D. R., Photo-assisted electrodeposition of cobalt-phosphate (Co-Pi) catalyst on hematite photoanodes for solar water oxidation. *Energy Environ. Sci.* 2011, 4 (5), 1759-1764.
 52. Sun, P.; Zhang, W.; Hu, X.; Yuan, L.; Huang, Y., Synthesis of hierarchical MoS₂ and its electrochemical performance as an anode material for lithium-ion batteries. *J. Mater. Chem. A* 2014, 2 (10), 3498-3504.

Chapter 6. Optimization of Quantum Dot-Sensitized Photoelectrode for Realization of visible Light Hydrogen Generation

1. Introduction

Photoelectrochemical (PEC) cells which can convert solar energy to the chemical energy such oxygen gas and hydrogen gas have received great attention.¹⁻⁷ A Titanium dioxide (TiO_2) has been considered as a very good photoanode in PEC cells due to its superior catalytic properties, facile electron-transfer feature, high chemical resistance and safe against toxicity.⁸⁻¹¹ Whereas, usage of the TiO_2 as a photoanode in PEC cell is limited by low photo-catalytic property due to the large bandgap of 3.2 eV, which can not absorb the visible light region.

Cadmium selenide Quantum-dots (CdSe QDs) have been applied as a high performance PEC materials with proper bandgap for the visible light and relevant energy level align for the water oxidation and reduction potential.¹²⁻¹⁶ Even though CdSe quantum dot decorated TiO_2 PEC photoanodes have been reported many times, those are relate to the studies about veil the properties of the CdSe quantum dot it means that less attention has been focused to maximizing the performance of CdSe QD/ TiO_2 system. P25, a commercially available TiO_2 materials with 75% anatase phase and 25% rutile phase, have been widely used a photovoltaic systems such as DSSCs, Organic solar cell and PEC cells.¹⁷⁻¹⁸

The novelty of the P25 is that it supply high surface area for active sites due to the high surface energy from notable feature of nanoparticle the a few tens of nanometer dimensions. However, the drawback of nano-scale P25 nanoparticles is not only low photoreaction by large band over visible light but also large reflectance at the interface of air and TiO_2 having a high refractive index. When dimensions of nanostructures are similar to the wavelength of irradiated light, the absorbance properties of the nanostructures can be improve in the range of visible light through light harvesting, which increase the possibility of absorbance by CdSe quantum dots.¹⁹⁻²¹ Thus, proper dimensional change of a P25 photoanode should maximize the power conversion performance of CdSe QD PEC cell.

In this chapter, we suggested an efficient strategy to enhancing generation of hydrogen gas using visible light illumination through an superior QDs-sensitized photoanode with enhanced light-harvesting ability. The light-harvesting P25 (lh-P25) working electrode, composed of light trapping layer and anti-reflectance layer, is fabricated using a 12- μm height of P25 TiO_2 film with nanocrystalline particles (25nm) and a 150 nm height two dimensional patterned TiO_2 layer on top of the film and a 350nm height of TiO_2 nanowire at the bottom. The arrangement of the light-harvesting layer at both the top and the bottom of the mesoporous TiO_2 layer allows for absorbed light to be captured, thereby achieving maximum intensity within a wide solar spectrum range.

Moreover, CdSe QDs/lh-P25 can extend the capability of photocatalytic property of P25 to visible range by adding the lower bandgap of CdSe QDs than that of P25. The photocurrent density of CdSe QDs/lh-

P25 is approximately 18.7 mA/cm^2 , which is 35% higher than that of the CdSe QDs/P25 at $0.5 \text{ V}_{\text{Ag/AgCl}}$ under 1 sun irradiation. Furthermore, a remarkably high photocurrent of 16.4 mA/cm^2 was measured with the UV filter ($\lambda > 420 \text{ nm}$) illumination by CdSe QDs/lh-P25, indicating the reliability of synthesis of hydrogen gas exclusively by visible light. The notably enhanced efficiency of CdSe QDs/lh-P25 decorated by the increased light trapping structures composed of light scattering layer and anti-reflector layer is an effective design to maximize P25 photoanode in PEC system.

2. Experimental Procedure

2.1 Chemicals used

Titanium isopropoxide, hydrochloric acid (37 wt%), P25-TiO₂ (ENB Korea, 20 nm), Cadmium acetate dihydrate (reagent grade, 98%) and Selenium (powder, 99.99%). All chemicals were purchased from Sigma-Aldrich, and all chemicals were used without further purification.

2.2 Characterization

The structures were examined by SEM (NOVA NANOSEM 230 FESEM, 15kV), TEM (JEM- 2100, 200kV). The powder diffraction data were obtained using a Rigaku Co. High Power XRay Diffractometer D/MAZX 2500V/PC from 20° to 80° . The diffuse reflectivity and UV-visible extinction spectra were measured using a Cary 5000 UV/Vis/NIR and Cary-100 UV-vis spectrophotometer (Varian), respectively. IPCE measurements were also conducted using an EQE system (Model QEX7) by PV Measurements Inc. (Boulder, Colorado). The surface area was collected by using a Belsorpmax (Bel Japan).

2.3 Fabrication of p-TiO₂ NWs and p-PDMS

The FTO glass was cleaned using acetone and IPA in the bath of sonicator for 10min and nitrogen blowing. A height of 300nm Su-8 film was coated on the prepared FTO glass and annealed at 100°C for 40min to remove the PEGDA solvent. The Su-8 coated samples were double exposed for $6 \times 6 \text{ s}$ by rotating the sample 90° . A post-exposure bake and hard-bake procedures were conducted for 10min at 75°C and 95°C , respectively, before developing the Su-8 photoresist by propylene glycol monomethyl ether acetate. The patterned SU8 film on FTO glass was placed in a Teflon reactor vertically with a solution of 50 mL of water, 50 mL of HCl, and 5mL of titanium isopropoxide and then heated at 180°C for 65 min to grow TiO₂ NWs.^[1] The TiO₂ NWs/SU8 sample was annealed in a furnace at 500°C for 30 min to remove the organic template and increase the

crystallinity of the TiO₂ NWS. In the case of p-PDMS, PDMS precursors were poured on 300 nm thick patterned SU8 on a SiO₂ wafer and placed in a vacuum chamber to remove air bubbles from the PDMS. The PDMS/SU8 sample was heated at 80°C for 1h for curing and the patterned PDMS was separated from the SU8 template.

2.4 Fabrication of the lh-P25 electrode

P25 paste (ENB Korea, 20 nm) was coated on the top of p-TiO₂ NWs and annealed at 500°C for 30min to produce a 12µm thick layer. In order to fabricate top patterned P25, a soft lithography method was applied. After the P25 paste was imprinted by p-PDMS on 12µm thick P25/p-TiO₂ NWs, the sample was heated at 55°C for 50min to remove the residual solvent used for the P25 paste. The sample was placed in a furnace at 500°C for 30min to obtain 12µm thick p-P25/TiO₂ NWs (lh P-25).

2.5 Fabrication of CdSe/lh-P25

The CdSe layer was deposited on the surface of lh-P25 using a successive ionic layer adsorption and reaction (SILAR) process. To deposit CdSe onto lh-P25 and P25, the sample was immersed into a 50 mM Cd(Ac)₂ · 2H₂O ethanol solution for 1min, washed with absolute ethanol, immersed into Na₂SeSO₃ solution for 1min, and cleaned using D.I. water. The Na₂SeSO₃ solution was synthesized by dissolving 0.01 mol Se powder in a 0.1M Na₂SO₃ solution at 90°C for 9 hours. These procedures were repeated 15 times to obtain the best performance and the samples were drawn out from a glove box filled with nitrogen gas.

2.6 Calculation of effective refractive index of antireflection (AR) layer

The volume ratio of TiO₂ : air = 0.55 : 0.45 from the SEM image. On the basis of the effective medium theory, the effective refractive index n_{AR} can be calculated as 1.93 by the following equation

$$n_{AR} = [0.55 \times (n_{TiO_2})^q + 0.45 \times (n_{air})^q]^{1/q}, q=2/3.$$

Here, n_{TiO_2} is 2.488 for anatase and n_{air} is 1.

2.7 Photoelectrochemical (PEC) Measurement

The performance of PEC was measured for P25, lh-P25 samples using Pt counter electrode and Ag/AgCl reference electrode, respectively, in a poly-sulfide electrolyte of 0.24M Na₂S and 0.35M Na₂SO₃ solution with the pH 12. The power of the solar simulator was measured to be 100 mW/cm². The electrochemical data were measured using a Princeton Applied research VersaSTAT3 potentiostat. Linear sweep voltammograms were obtained by increasing the voltage from -0.6 V to 1.1 V for only TiO₂ samples and -0.9 V to 1.0 V for CdSe QDs/TiO₂ samples with a scan rate of 0.02 V/s under

irradiation of AM 1.5. current-time measurements were taken at $0.5V_{Ag/AgCl}$ during the solar source was switched on and off cycles every 10 seconds, manually using the shutter. The PEC performances of structures only in the visible range were acquired by the solar simulator coupled with a UV cutoff filter ($\lambda > 420$ nm).

2.8 Efficiency calculations

The chronoamperometric I-t studies on CdSe/lh-P25 as a function of applied over potential at 100 mW/cm² was measured, from which the photocurrent values have been taken for the efficiency measurements. The efficiency of the device was calculated using the following equation

$$\eta \% = \frac{J_p \times (E_{rev}^0 - |E_{app}|)}{I_o} \times 100\%$$

$$|E_{app}| = |E_{meas} - E_{oc}|$$

where J_p is the measured photocurrent in mA/cm², E_{REV}^0 is constant value as 1.23 V for the Ag/AgCl reference electrode, $|E_{app}|$ is the term related to the applied potential calculated through upper equation and I_o is the intensity of incident light in mW cm⁻². E_{meas} is the potential at which photocurrent was measured under AM 1.5. E_{oc} is the potential at which photocurrent measured under open circuit potential (OCP)

3. Result and Discussion

The illustration of the fabrication procedures of lh-P25 is depicted in Figure 1. a. First, a 500nm height of Su-8 polymer template (I) was synthesis through IL and the 500nm height of TiO₂ NWs (II) pattern was grown in the air holes of SU-8.²²⁻²³ The growth of pattern TiO₂ NWs on the SU-8/FTO substrate increase the optical property and provide a strong bonding between FTO and TiO₂ NWs, which help easily transfer electrons from the TiO₂ to the current collector. Second, P25 NPs were coated as film morphology with a thickness of 11.5 μ m (III) after removal of the Su-8 template by heating.

The thickness of the P25 layer was optimized to attain the highest efficiency based on previous experiments.^{18,21} Third, the top surface of the 11.5- μ m thick mesoporous P25 nanostructure was patterned by imprinting a 150-nm thick mesoporous TiO₂ square pattern on the top, resulting in a total thickness of 12 μ m. A cross-sectional scanning electron microscopy (SEM) image of the lh-P25 photoanode (V) with a configuration of the photon-trapping bottom layer, mesoporous P25 middle layer, and thin top AR layer is shown in the right panel (VI) of Figure 1 a. This illustrates the creation

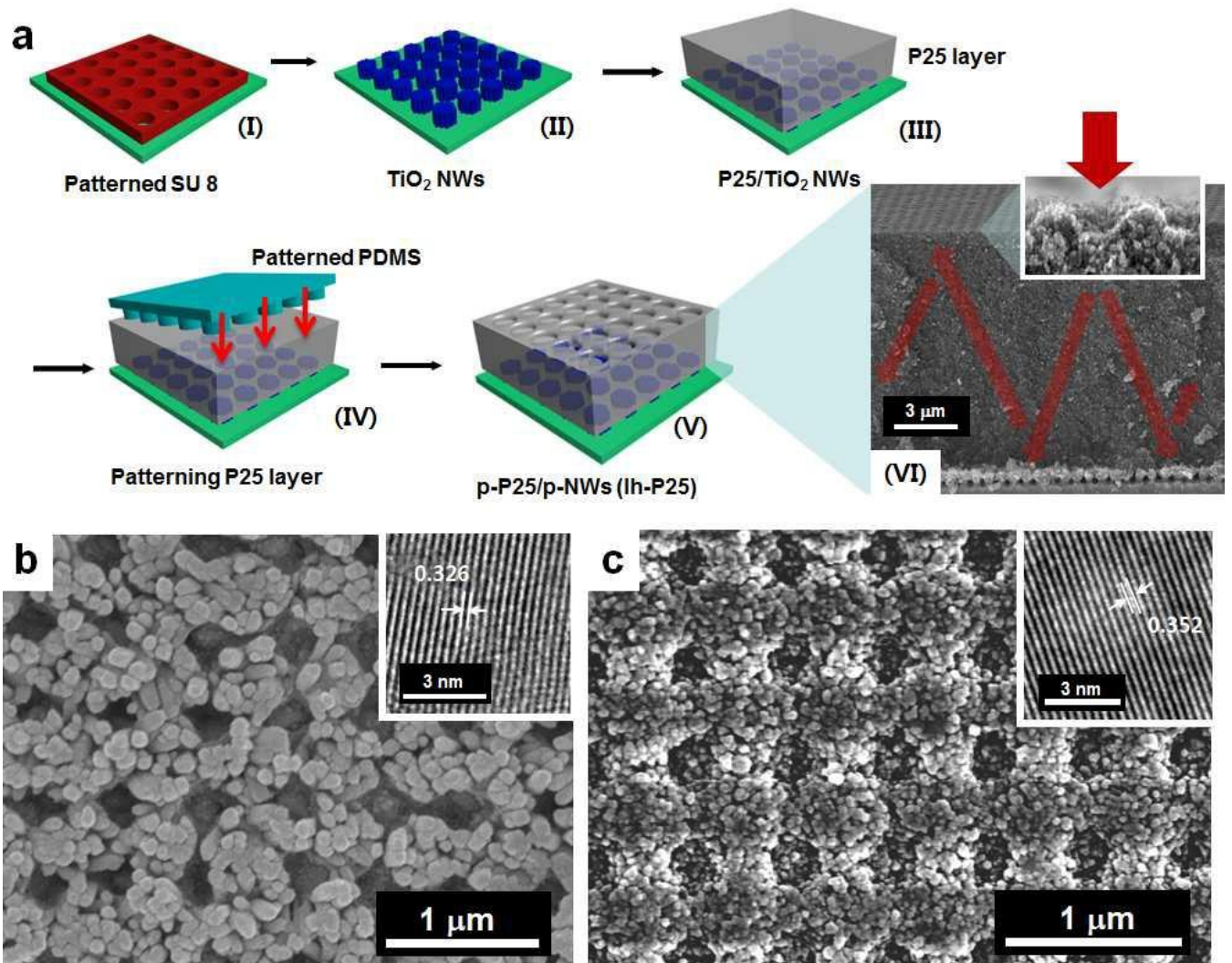


Figure 1. a) Scheme of the fabrication procedures of lh-P25. A SEM image of lh-P25. b) Top view SEM image of patterned TiO₂-NWs (the bottom layer of lh-P25). The inset shows a TEM image of the rutile phase TiO₂ NWs with the lattice constant of 0.326 nm. c) Top view SEM image of the patterned nanocrystalline TiO₂ layer for anti-reflection (the top layer of lh-P25). The inset shows a TEM image of the anatase phase TiO₂ nanoparticles with the lattice constant of 0.352 nm.

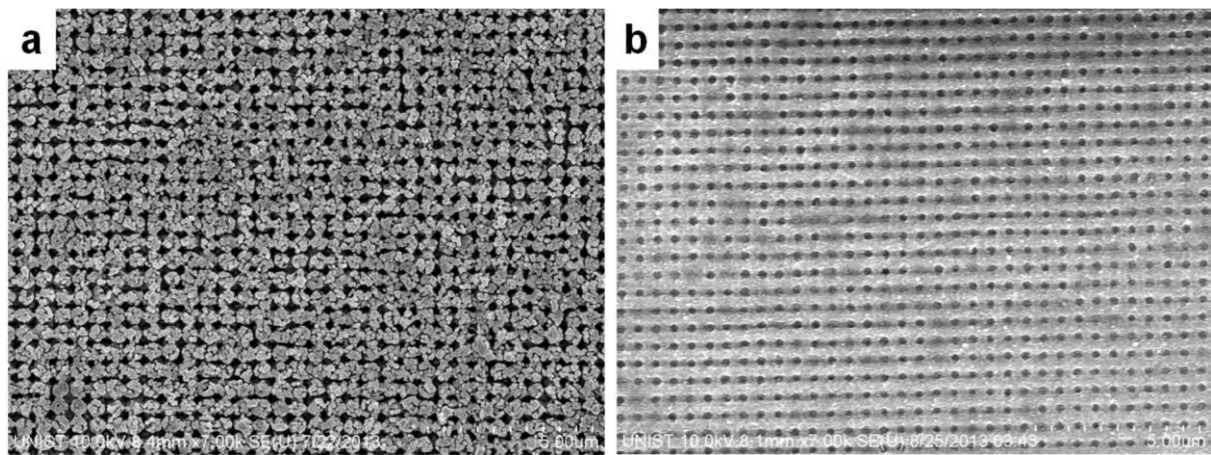
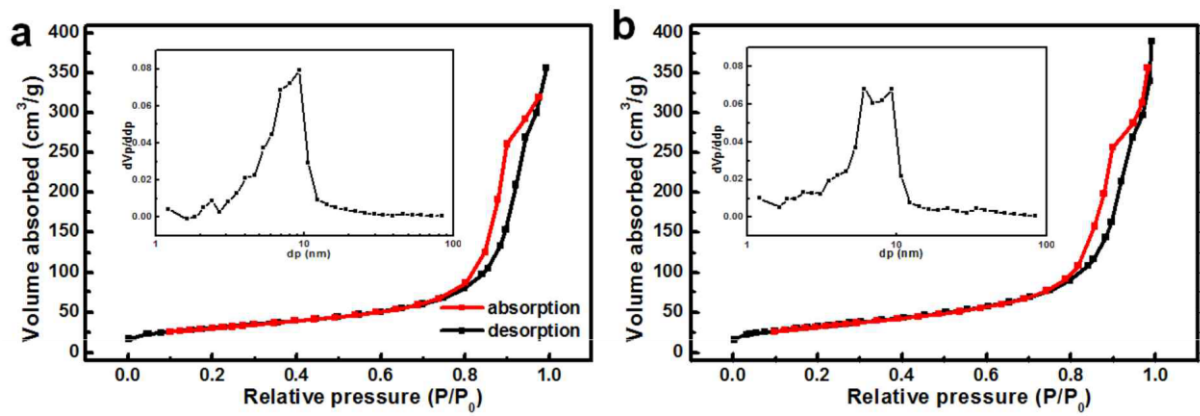


Figure 2. SEM image of bottom layer (a, p-TiO₂ NWs), top layer of antireflection layer (b, p-P25) of lh-P25.

of a highly improved light-harvesting mechanism at both ends. Once the light with substantially reduced reflection enters the lh-P25 electrode, it is scattered by the large scale TiO₂ NW pattern at the bottom, which permits multiple passes of greatly absorbed photons. Figure 1 b is an SEM image of the thin bottom layer of square TiO₂ NW patterns with a diameter of 500 nm. The dimensions of the square patterns were determined so as to efficiently trap light while a sufficient surface area was secured because of the smaller diameter of the NW bundles, as optimized in our previous studies.^{22,25} XRD studies in Figure S3 in the Supporting Information indicate the formation of nanocrystalline TiO₂ in the rutile form (JCPDS card 01-073-1765) with a lattice spacing of around 0.326 nm. Figure 1 c is an SEM image of top-patterned P25 achieved by stamping a P25 layer using poly(dimethylsiloxane) (PDMS) molds followed by final sintering. The dimensions of the topsurface pattern were fixed so as to maximize the AR effects, which were inspired by the features of a moth's eye. [5b , 7] The volume fraction of TiO₂ in the AR layer was measured to be 0.55 based on the captured SEM image, giving an effective refractive index of 1.93, as calculated in the Supporting Information. The surface area of the lh-P25 electrode obtained by Brunauer–Emmett–Teller (BET) measurements was 105 m² g⁻¹, which is comparable to that of a compact film of P25 (113 m² g⁻¹) as described in Figure S2 (Supporting Information), because of coupling of the light-harvesting layers in the form of hierarchical nanostructures. The light-harvesting effects achieved by incorporating large-scale, thin layers onto both sides of a P25 electrode can be quantified by the reflection spectra and diffuse reflection spectra. The reflection spectra were obtained by shining light on a 12-μm thick P25 film and 12-μm thick lh-P25 film from top to bottom. When light passed from air to the TiO₂ nanocrystalline layered control (bulk) film, we expected the majority of light to be reflected at the interface of air ($n = 1$) and TiO₂ ($n = 2.49$) because of the substantial difference in refractive index. Compared to the P25 film with 60% reflectance at a wavelength of 600 nm, the lh-P25 film exhibited a considerably lower reflectance value, indicating an increased amount of absorbed light in lh-P25. We attributed this to the modified refractive index of the patterned P25 layer ($n_{AR} = 1.93$) at the top of the lh-P25 electrode, which permitted a gradual change of the refractive index from 1 (in air) to 1.93 (in the patterned P25 layer) to 2.49 (in the plain P25 in the middle). Another type of light harvesting, the increased intensity of scattered light due to photon trapping in the 12-μm thick lh-P25 film under beam irradiation, was demonstrated by the diffuse reflectance spectra, as shown in **Figure 2 b**. The lh-P25 film with only a 500-nm thick patterned TiO₂ NW layer at the bottom showed a much higher diffuse reflection spectra in the visible spectrum of light (400–800 nm), indicating that the absorbed light was intensely scattered within the nanostructure film. The synergy of adding both of these light-harvesting layers onto the P25 film were evaluated by UV-vis spectroscopy measurements of a 12-μm thick P25 and lh-P25 film by illuminating light from top to bottom at normal incidence (Figure 2 c). A photograph of the lh-P25 film showing a distinct opalescent color because of the periodic patterns in the light-harvesting layers is shown next to



	lh-P25	P25
Average Pore size (nm)	20.6	20.7
Pore volume (cm³ g⁻¹)	0.54	0.58
Surface area (m² g⁻¹)	105.1	113.7

Figure 3. BET of lh-P25 (a) and P25 (b). The inset is pore-size distribution. The surface area are summarized in the table.

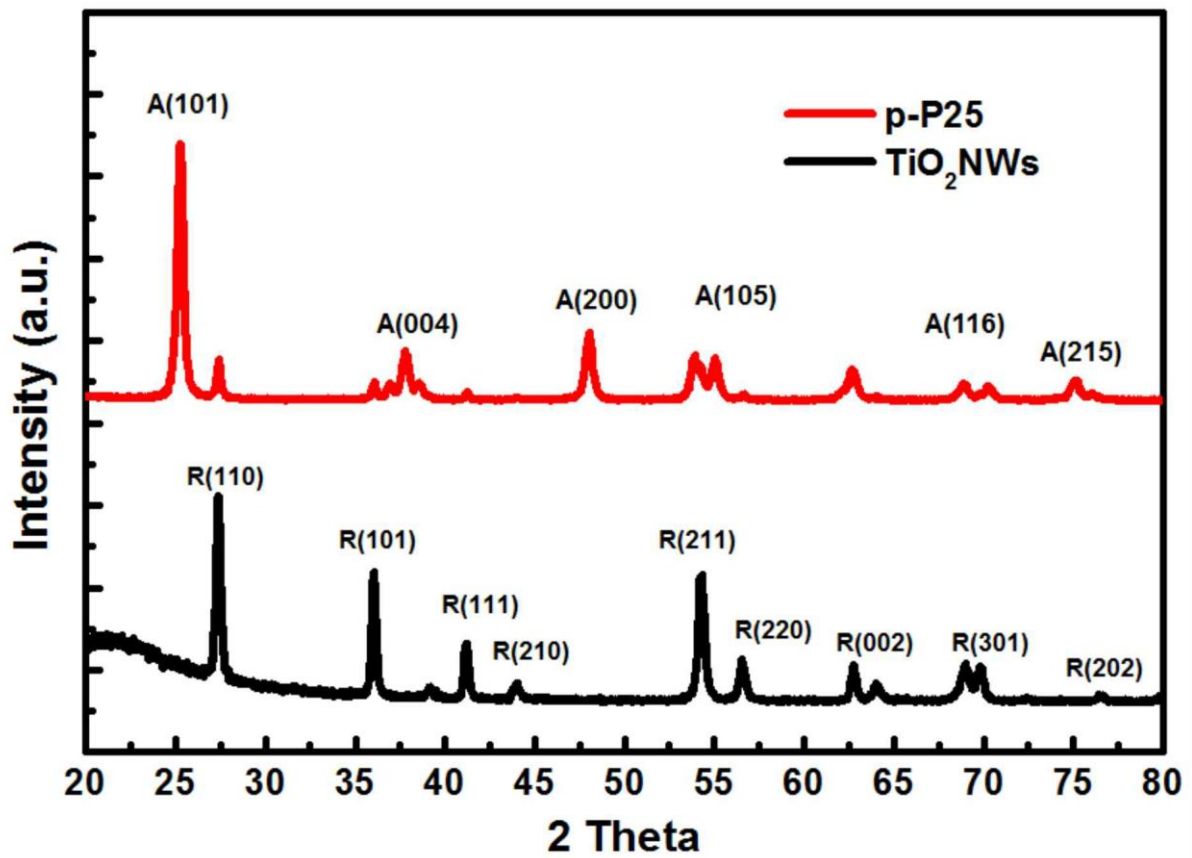


Figure 4. X-ray diffraction (XRD) patterns of as-prepared TiO_2 NWs and p-P25.

that of a P25 film in the inset of Figure 2 c. Pristine TiO₂ nanoparticles absorb light in the 300 to 350 nm range. Similar intensity values were obtained for an intense and broad absorption band ranging from 350 to 800 nm when the two-sided light-harvesting layer was implemented. We attributed this to the synergetic assembly of the AR and photon-trapping layers within the larger dimensions of the hierarchical nanostructures. (The controlled measurements of the optical properties from the separate AR and photontrapping layers are presented in Figure S4, Supporting Information.) Quantum dots (QDs) were further deposited onto a lh-P25 electrode to realize photoconversion devices able to operate under solely visible light via multiple excitations by single-photon absorption of the QDs. When CdSe QDs were incorporated onto the mesoporous TiO₂ structure via 15 cycles of successive ionic layer adsorption and reaction (SILAR), a greatly enhanced working capability of this lh-P25 electrode relative to that of pristine P25 was observed in the visible wavelength region, as presented in Figure 2 d. The inset in this Figure is the TEM image of a CdSe QD with a diameter of 4–5 nm and lattice spacing of 0.31 nm deposited on lh-P25. More TEM images of QDs with detailed features are shown in Figure S5 in the Supporting Information. It should be noted that the greatly increased absorption of CdSe/lh-P25 indicates more efficient sensitization of the QDs and is attributable to a higher and wider optical density of lh-P25 above the band edge of CdSe (ca. 630 nm). The hydrogen generating efficiency of the samples supported by light harvesting was investigated by photo-electrochemical measurements on a P25 control sample, lh-P25, CdSe/P25, and CdSe/ lh-P25 electrode. Ag/AgCl, a Pt mesh, and as-prepared samples were used as the reference electrode, counter electrode, and working electrode, respectively, in a 0.24 m Na₂S and 0.35 m Na₂SO₃ electrolyte solution. Here the sulfide in the electrolyte serves as a sacrificial agent for the reduction of the CdSe QDs, as commonly adapted in many QD-based studies.²⁶

Figure 3 a presents linear sweep voltammograms of the pristine P25 and lh-P25 samples, which provides the current densities of photoexcited electrons under AM 1.5 G simulated sunlight illumination (UV–vis, 100 mW cm⁻²). The photocurrent density of lh-P25 reached 1.45 mA/cm² at an applied bias of 0.5 V, which is approximately 40% greater than that of the optimized P25 control sample, indicating the strong potential of pristine lh-P25 in photoconversion systems. Figure 3 c compares the linear sweep voltammograms of CdSe/lh-P25 and CdSe/P25. When lh-P25 is augmented by CdSe QDs the electrons in the conduction band of TiO₂, which can either be transferred from the conduction band of CdSe or directly excited from the valence band of TiO₂, are drawn to the counter electrode, thus generating hydrogen, whereas the holes that have diffused to the surface of TiO₂ or CdSe are involved in the oxidizing of S²⁻ and SO₃²⁻, as illustrated in Figure 3 b. (An image capturing the generation of a large amount of H₂ gas is presented in Figure S7, Supporting Information). The photocurrent density of CdSe/lh-P25 increased by 13.4 times the amount before introduction of the CdSe and reached about 18.7 mA/cm². This is the highest recorded value in the world attained among similar QD-sensitized TiO₂ PEC devices and is 21.4% greater than that obtained from an optimized control sample, CdSe/P25,

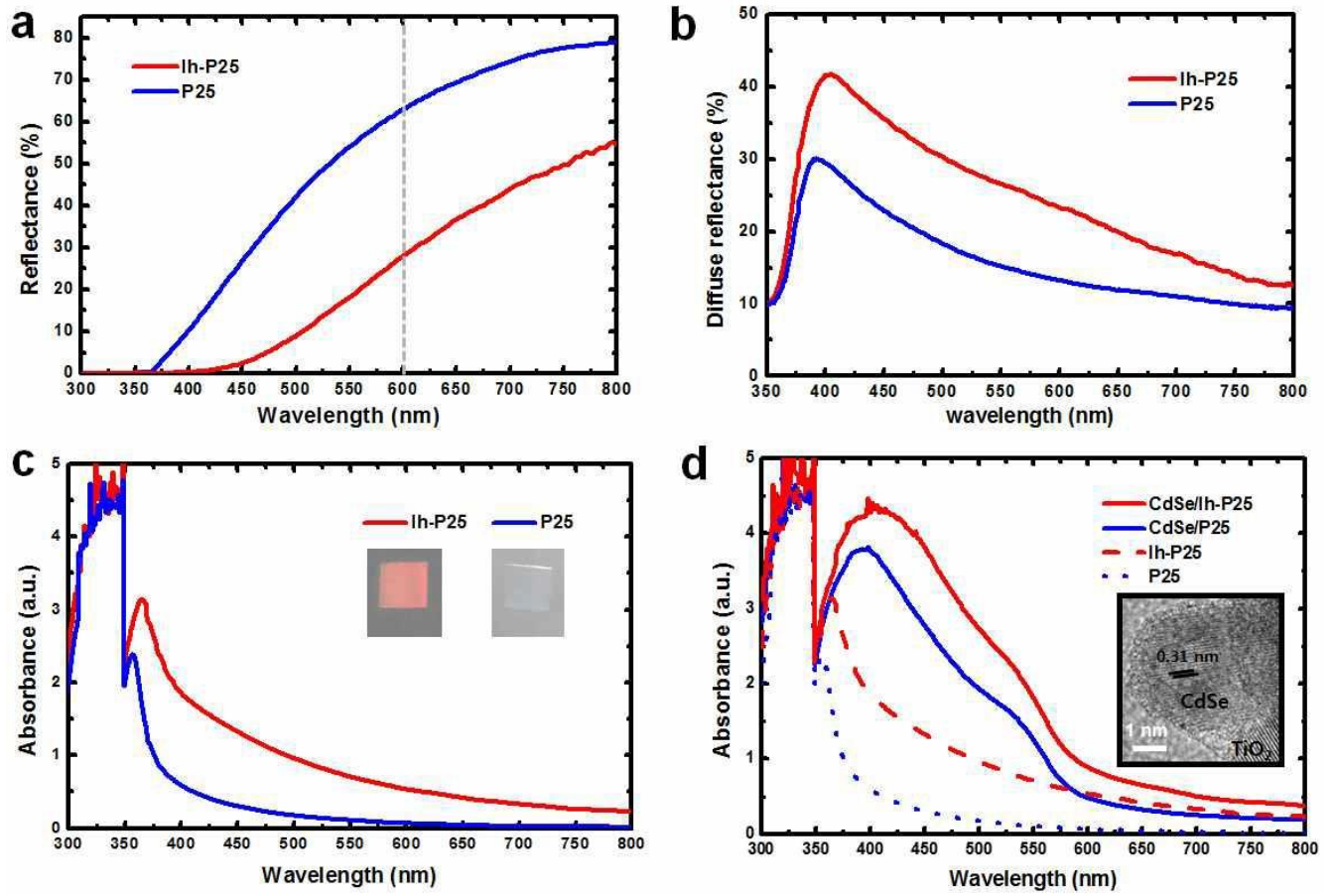


Figure 5. Optical features of P25 and lh-P25 (p-P25/p-NWs). (a) Reflectivity, (b) Diffuse reflectivity, and (c) UV-visible spectrum of P25 and lh-P25 under UV-visible light irradiation. (d) UV-visible absorbance spectrum of P25 and lh-P25 before and after the deposition of CdSe. The inset image shows the TEM image of CdSe QD with lattice spacing of 0.31nm decorated on TiO₂.

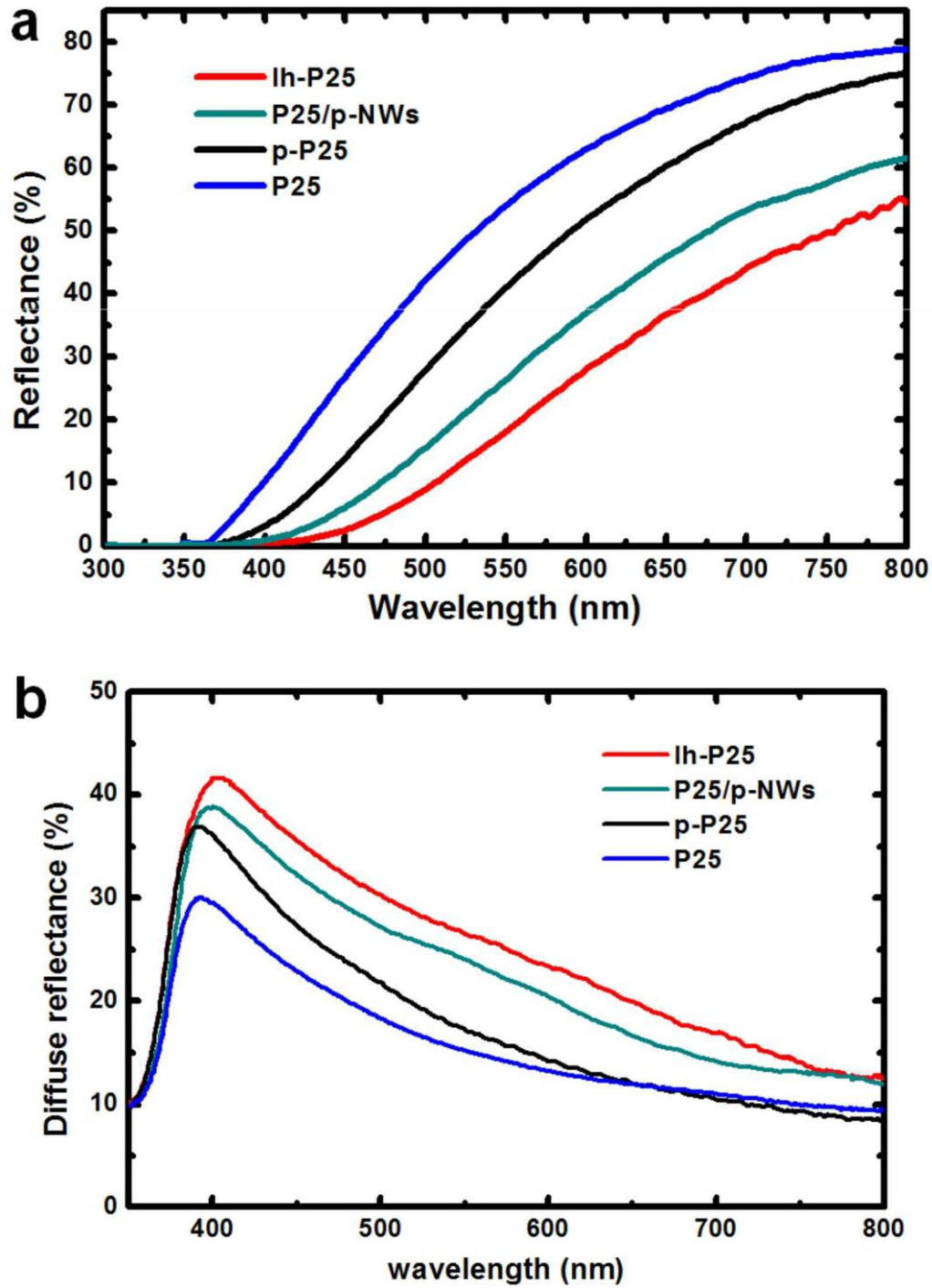


Figure 6. Optical features of P25 P25/p-NWs, p-P25, and lh-P25 (p-P25/p-NWs). (a) Reflectivity, (b) Diffuse reflector spectrum of the samples under UV-visible irradiation.

under the same illumination of 100 mW/cm^2 . More surprisingly, the photocurrent density of CdSe/lh-P25 created by only visible light illumination (red dotted line, AM 1.5 G, using a cutoff filter ($>420 \text{ nm}$)) reached 16.4 mA/cm^2 , which is also greater than that obtained under UV-vis irradiation in other comprehensive studies, including the CdSe/P25 in this study, all of which clearly indicates the realization of a CdSe/lh-P25 electrode capable of using only visible light (see Figure 3 c). This surprising result was achieved by the large enhancement in absorption of lh-P25 in the visible range via efficient light harvesting, provided by a wavelength overlap of the light harvesting from the TiO_2 electrode and the excitation of CdSe. The incident photon-to-current efficiency (IPCE) curves of CdSe/lh-P25 at a photocurrent of 18.7 mA/cm^2 exhibited much higher values than those of CdSe/P25 in the entire wavelength range, with a maximum IPCE value of 70.1% (48.1% for CdSe/P25) at 510 nm, as shown in Figure 3 d. Furthermore, the greatly enhanced and wide responses from 350 to 600 nm reflect the enhanced quantum efficiency of CdSe/lh-P25 in the visible region for hydrogen generation supported by light harvesting. **Figure 4** a shows the chronoamperometric $I-t$ curves of CdSe/lh-P25 measured at an applied potential of 0.5 V with chopped illumination of AM 1.5 G for UV-vis and visible light under 10 s exposure using on/off cycles. The sharp increase to the maximum and fast decay to zero of the photocurrent density for both cases during the on/off illumination cycles indicates the fast transport of photogenerated electrons from CdSe/lh-P25 to the FTO substrate. In order to gain a better insight into the fast electron transfer mechanism in lh-P25, the electrochemical impedance spectroscopy (EIS) measurements were performed at a frequency range of 100 kHz to 0.1 Hz and a bias of 0.6 V under AM 1.5 G light illumination with an amplitude of 10 mV. The Nyquist plots obtained by EIS measurements are shown in Figure 4 b with an equivalent circuit used for fitting the data as an inset. The high-frequency intercept on the real axis represents the sheet resistance (R_s) of the device, which indicates the tight bonding between the TiO_2 nanostructures and FTO substrate for both CdSe/P25 and CdSe/lh-P25. The Nyquist plots are further composed of two semicircles: a smaller one (R_1) at a high frequency range, in which the diameter represents the charge-transfer resistance at the interfaces of the electrolyte/ Pt counter electrode and a larger one (R_2) at an intermediate frequency region, which conveys the transport phenomena at the TiO_2 /QD/electrolyte interface. It can be clearly seen that CdSe/lh-P25 shows the better overall impedance curve with a lower value of R_1 and R_2 , as shown in Figure 4 b and **Table 1**. Importantly, the much smaller diameter of the second semicircle (R_2 : $13 \Omega \text{ cm}^2$ vs. $28.6 \Omega \text{ cm}^2$) for the CdSe/lh-P25 sample clearly indicates a lower interfacial charge-transfer resistance between the TiO_2 electrode and the electrolyte and thus a faster interfacial charge transfer to the electron donor/acceptor. Furthermore, the electron recombination kinetics were studied by monitoring the photovoltage decay upon terminating the illumination on the CdSe/P25 and CdSe/lh-P25 samples, which allows the photoelectron lifetime to be evaluated.

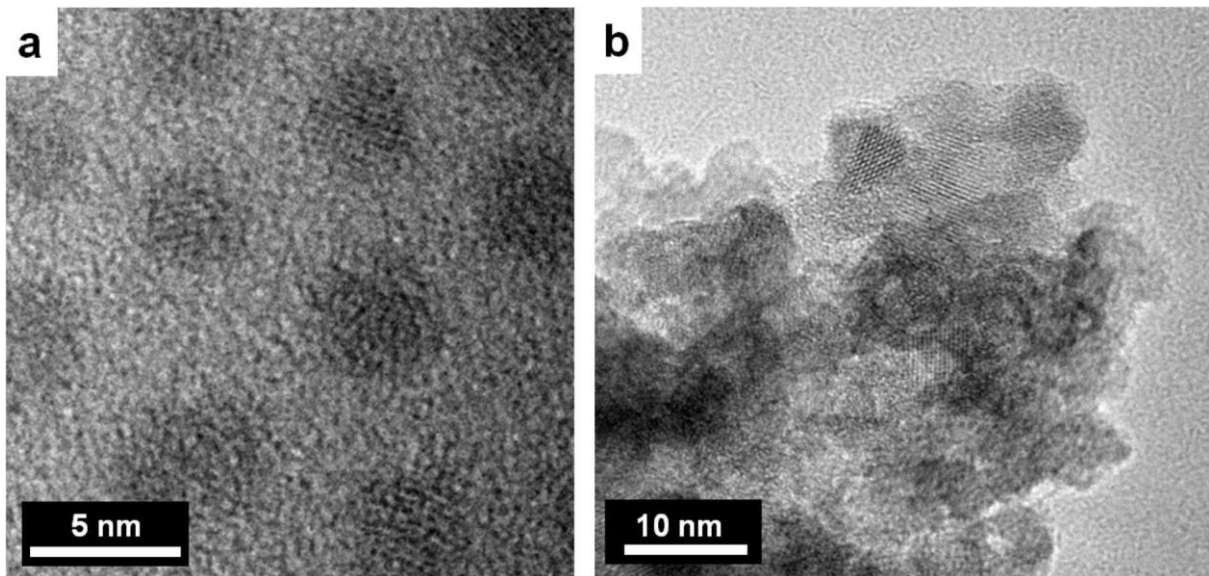


Figure 7. TEM images of (a) CdSe and (b) CdSe/lh-P25.

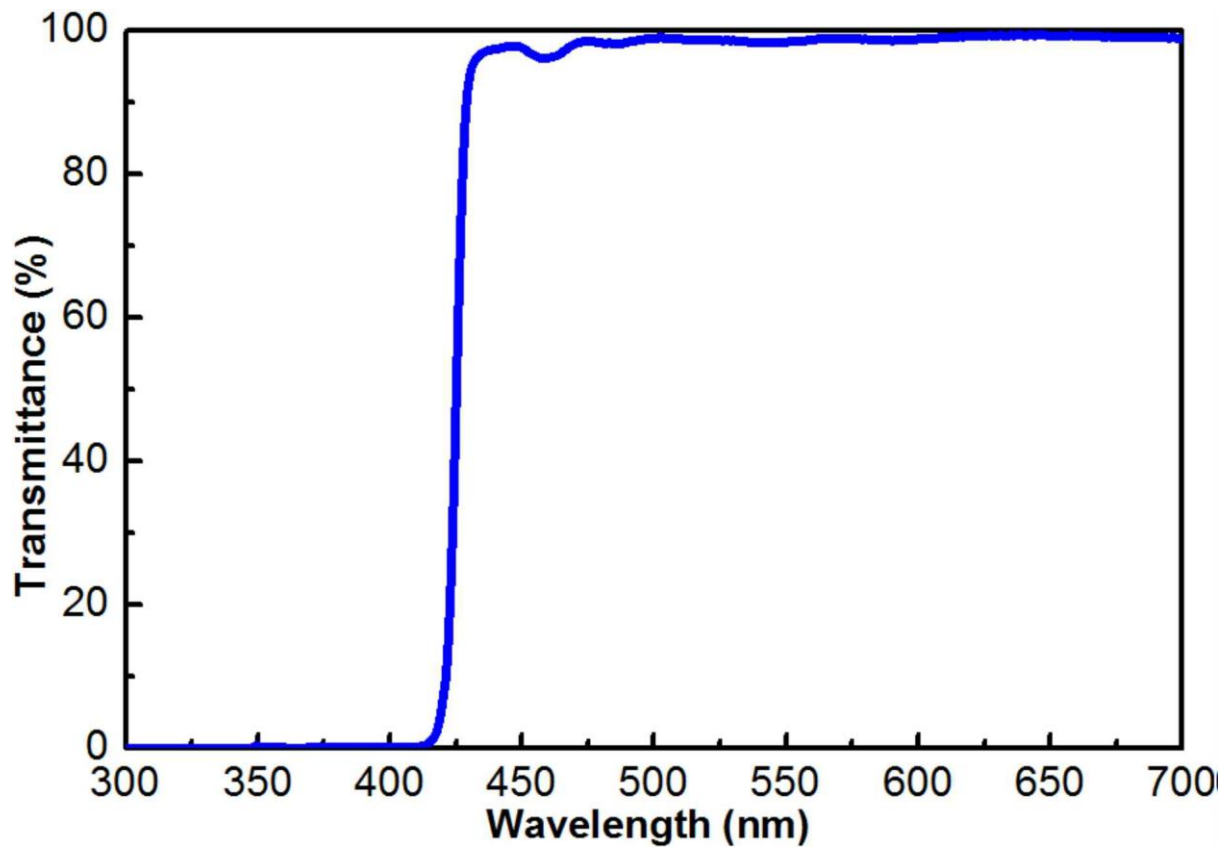


Figure 8. Transmittance spectra of the UV-cutoff filter

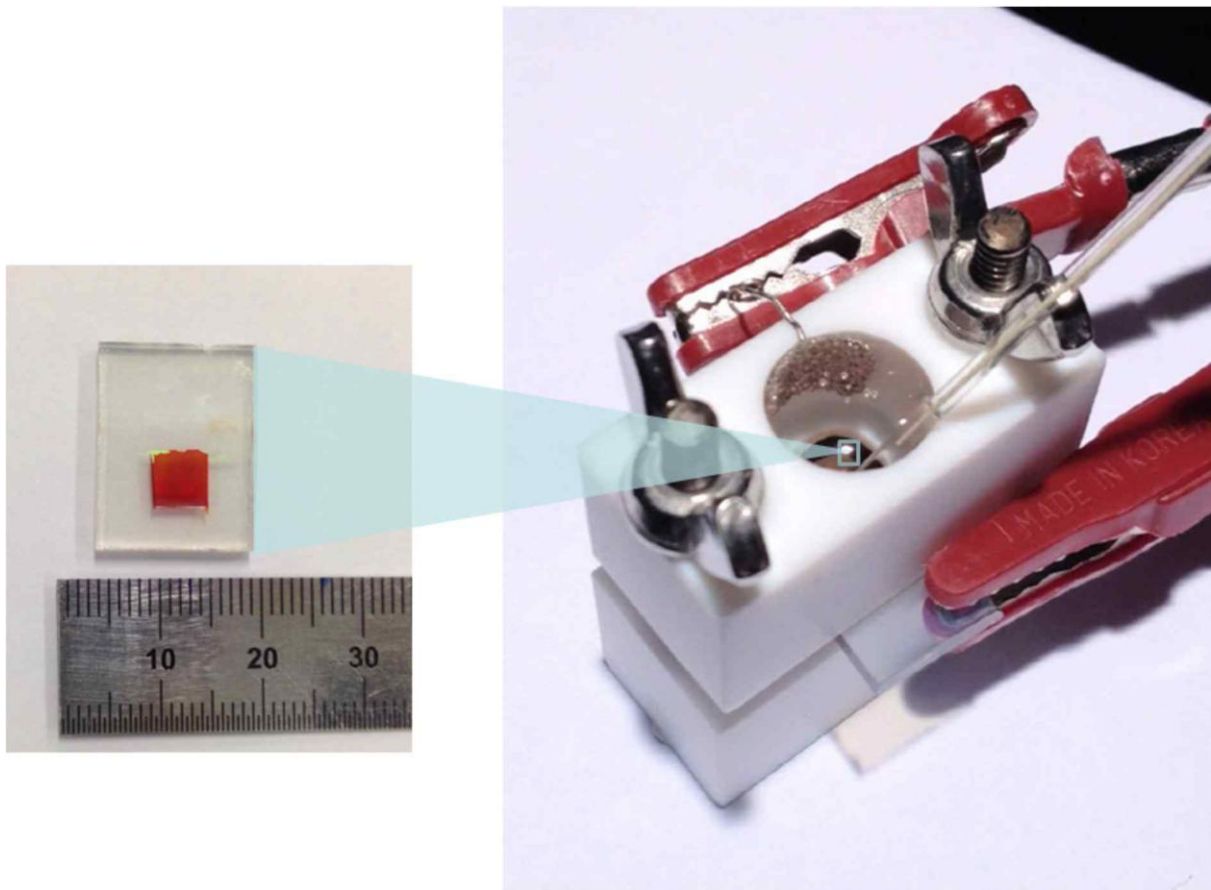


Figure 9. Experimental setup for PEC measurements.

Photoexcited electrons in the CdSe QDs are transferred to the conduction bands of TiO₂ and are stored within the TiO₂ nanostructures by initial illumination. Once the light is turned off, the electron density in the conduction band of TiO₂ decays mainly because of recombination of electrons and holes. Figure 4 c plots the V_{oc} decay as a function of time for CdSe/P25 and CdSe/lh-P25. It is clear that a much slower V_{oc} decay rate is found for the CdSe/lh-P25 electrode as compared to the CdSe/P25 electrode, suggesting slower recombination kinetics in CdSe/lh-P25. The average lifetime (τ_n) of photoexcited electrons before recombination can be calculated from the following equation

where k_B is the Boltzmann's constant, T is the temperature, e is the elementary charge, and V_{oc} is the open-circuit voltage at time t . Figure 4 d shows the calculated τ_n as a function of V_{oc} for CdSe/P25 and CdSe/lh-P25. CdSe/lh-P25 clearly shows a longer lifetime of the photoexcited electrons than CdSe/P25, which verifies the facile electron transport with a more effective separation of the photo-generated electron-hole pairs.

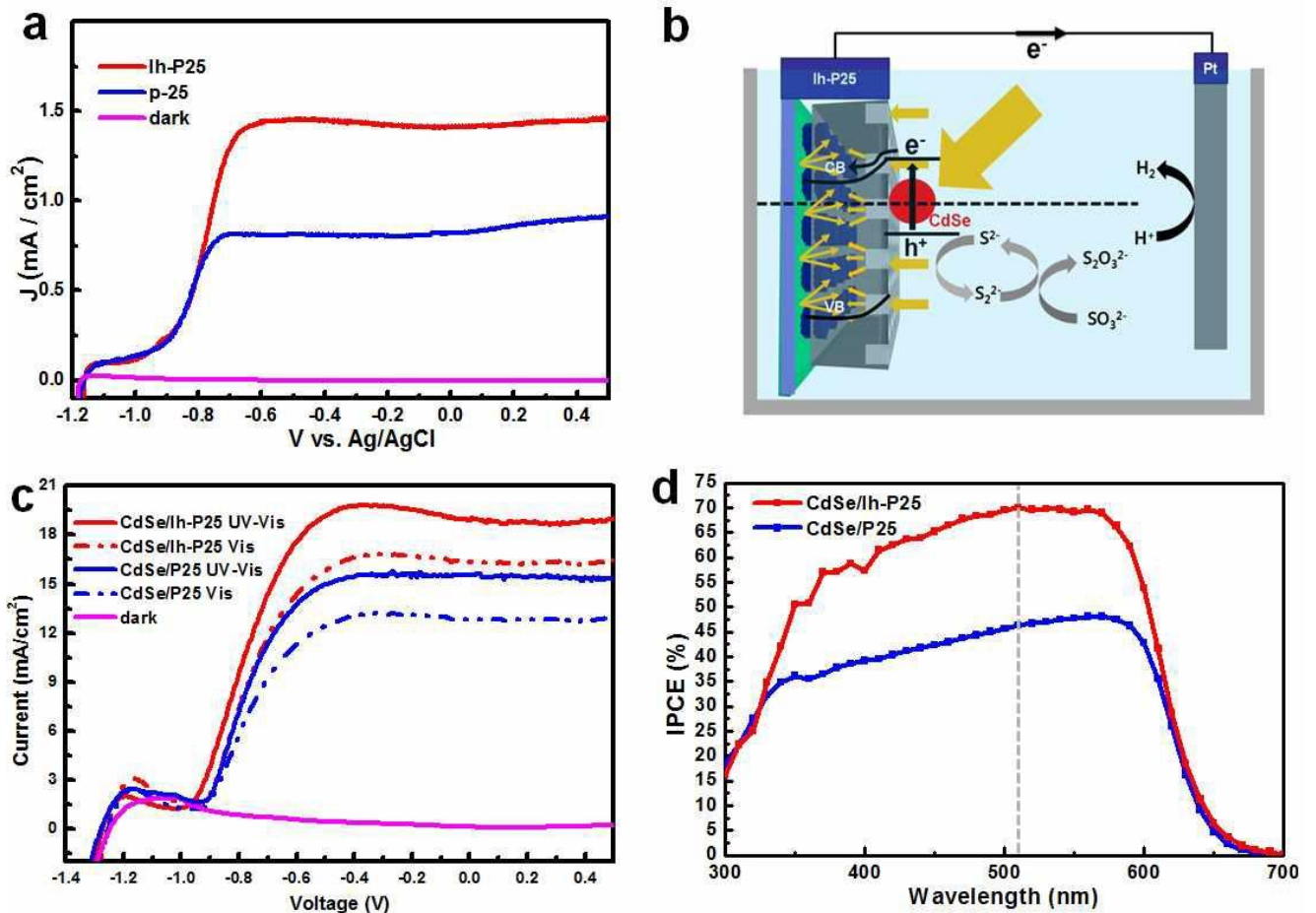


Figure 10. PEC performance of P25, lh-P25, CdSe/P25, and CdSe/lh-P25 under 1 sun irradiation (100 mW/cm^2). (a) J-V curve of P25 control and lh-P25 under UV-visible and dark conditions. (b) Schematic diagram showing hydrogen generating mechanism of CdSe/lh-P25. (c) J-V curve of CdSe/P25 and CdSe/lh-P25 under UV-visible, visible light irradiation, and dark conditions. (d) Measurement of the IPCE (incident photon-to-electron conversion efficiency).

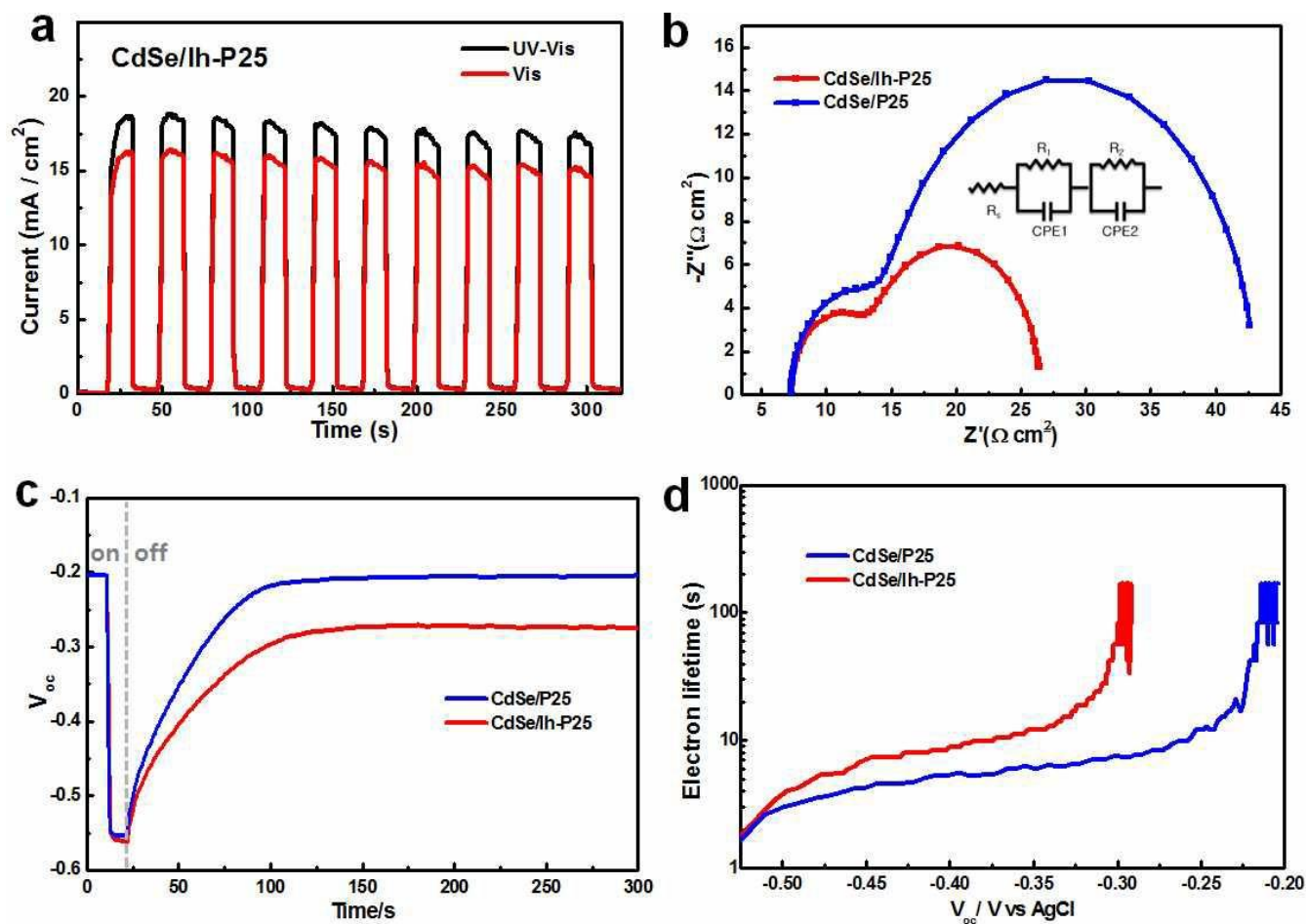


Figure 11. (a) The chronoamperometry curve of CdSe/lh-P25 at a bias of 0.5 V under UV-visible and visible light irradiation. (b) Nyquist plots of CdSe/P25 and CdSe/lh-P25. The inset shows an equivalent circuit used for fitting data. (c) V_{oc} vs. time profile of CdSe/P25 and CdSe/lh-P25. (d) The electron lifetime calculated from the V_{oc} decay.

Table 1. EIS responses of CdSe/P25 and CdSe/lh-P25.

	$R_s(\Omega/\text{cm}^2)$	$R_1(\Omega/\text{cm}^2)$	$R_2(\Omega/\text{cm}^2)$	$\text{CPE1}(\text{F}/\text{cm}^2)$	$\text{CPE2}(\text{F}/\text{cm}^2)$
CdSe/lh-P25	7.285	6.1	13.0	9.9×10^{-4}	9.3×10^{-3}
CdSe/P25	7.285	7.1	28.6	9.5×10^{-4}	6.3×10^{-3}

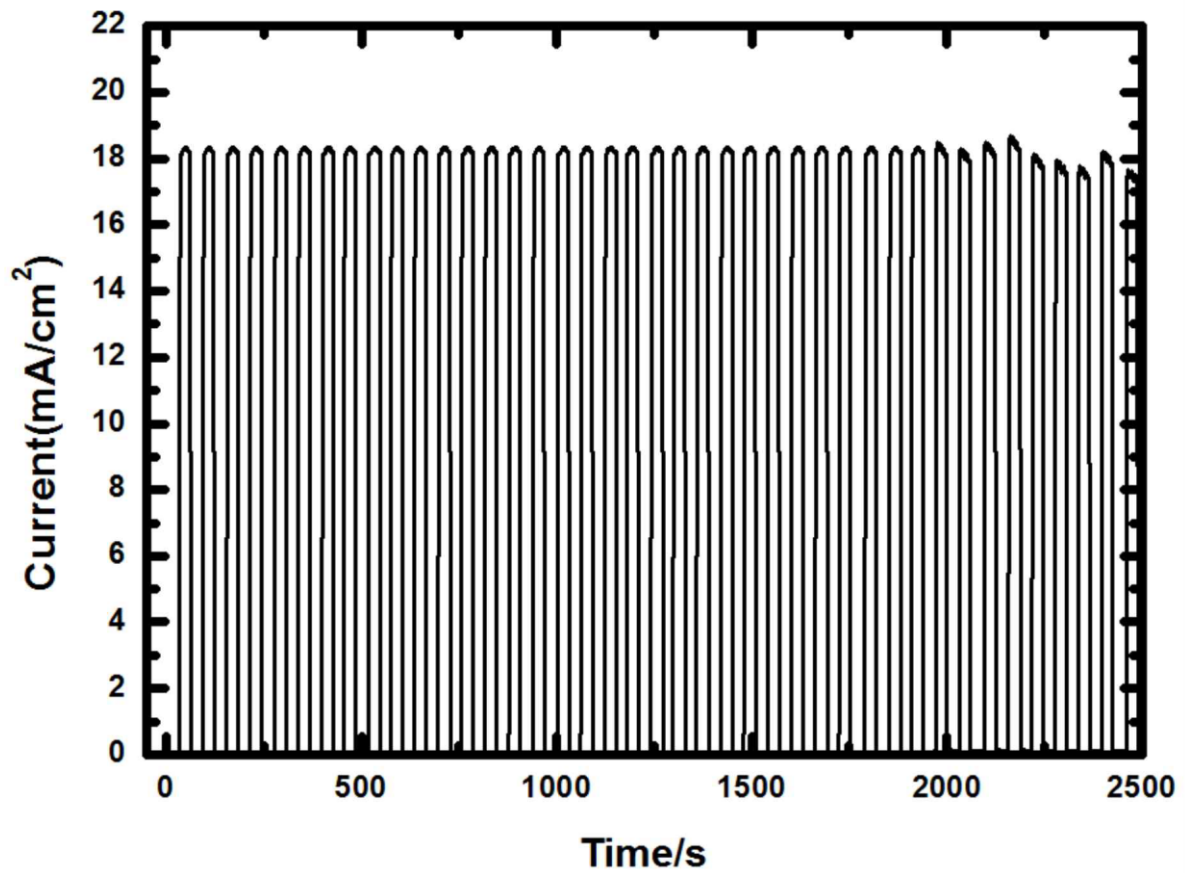


Figure 12. J-t curve of CdSe/lh-P25 under UV-visible illumination at a fixed bias of 0.5 V vs. Ag/AgCl, showing reasonable stability of the QD-sensitized PEC device.

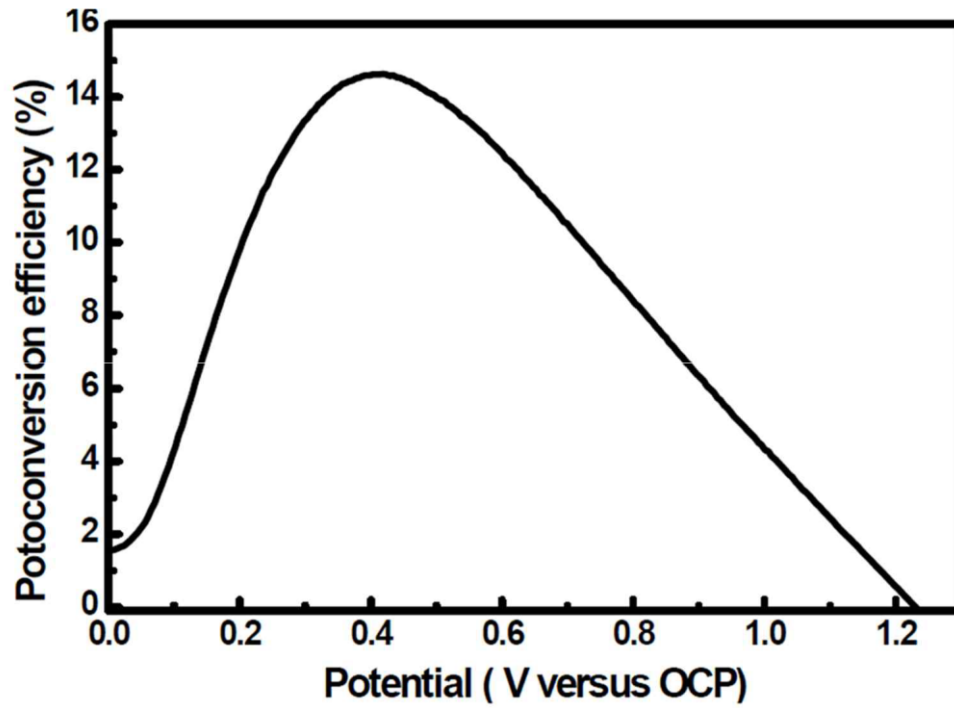


Figure 13. Photoconversion efficiency of the PEC cell with CdSe/Ih-P25 electrode as a function of applied potential.

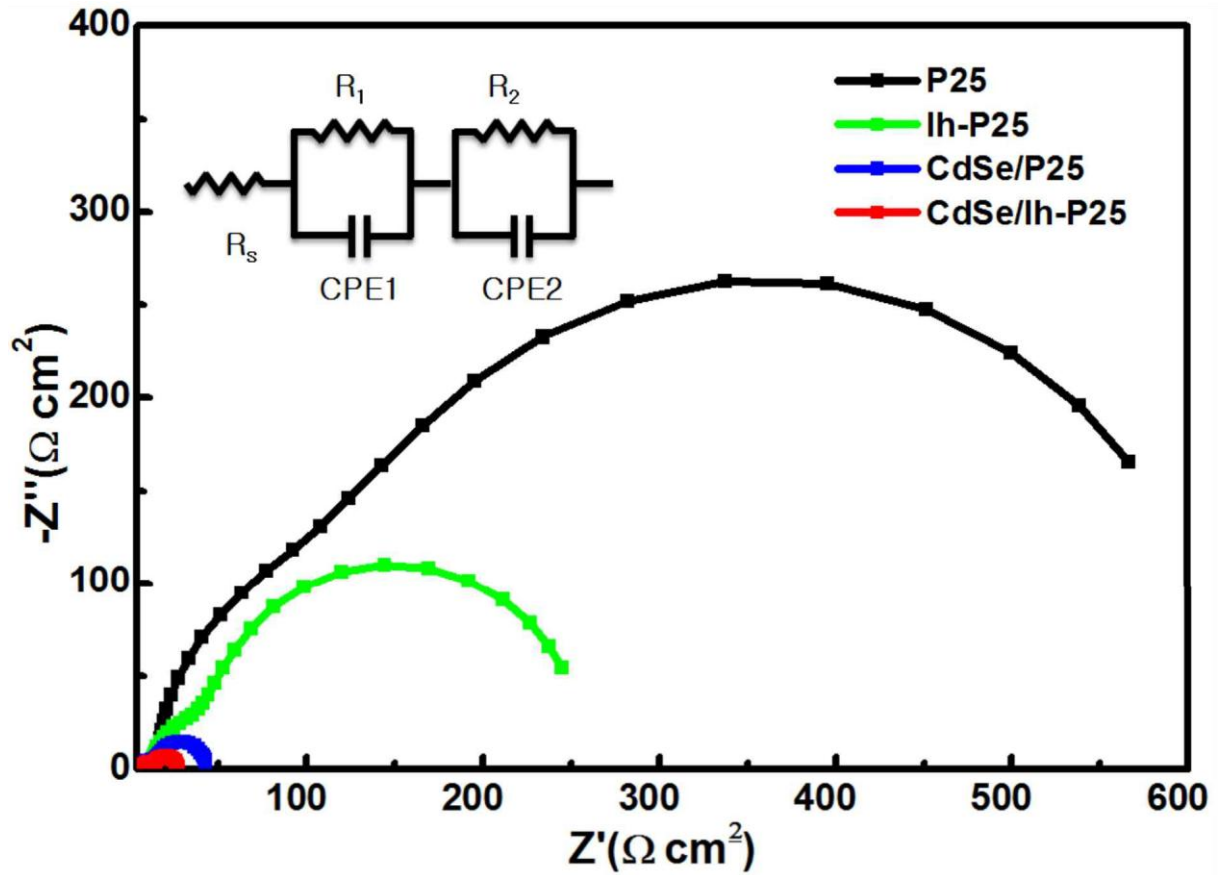


Figure 14. Nyquist plots of P25, lh-P25, CdSe/lh-P25, and CdSe/lh-P25. The inset shows an equivalent circuit used for fitting data.

4. Conclusion

In summary, we successfully optimized an electrode material for photoconversion devices to harvest light, supported by photon trapping and AR effects while retaining an adequate surface area by creating a hierarchical type two-sided layer. The observed optical properties verify the outstanding light-harvesting phenomena of lh-P25, which lead to remarkable benefits in the hydrogen generation reaction of a TiO₂ semiconductor in the UV–vis range. The photocurrent of CdSe/lh-P25 (18.7 mA cm⁻²) was 1.35 times greater than that of a CdSe/P25 photoelectrode. More importantly, the CdSe/ lh-P25 electrode had a current density of 16.4 mA cm⁻² under light-filtered conditions (visible light only), which is the highest reported value in the visible range thus far. The excellent performance of CdSe/lh-P25 for both UV–vis and visible light illumination suggests that systematic engineering of the light can provide an innovative means of designing photoactive materials with maximum photoconversion efficiency.

5. REFERENCES

1. Ahn, H.-J.; Kim, S.-I.; Yoon, J.-C.; Lee, J.-S.; Jang, J.-H., Power conversion efficiency enhancement based on the bio-inspired hierarchical antireflection layer in dye sensitized solar cells. *Nanoscale* 2012, 4 (15), 4464-4469.
2. Chen, H. M.; Chen, C. K.; Chang, Y.-C.; Tsai, C.-W.; Liu, R.-S.; Hu, S.-F.; Chang, W.-S.; Chen, K.-H., Quantum Dot Monolayer Sensitized ZnO Nanowire-Array Photoelectrodes: True Efficiency for Water Splitting. *Angew. Chem. Int. Ed.* 2010, 49 (34), 5966-5969.
3. Cheng, C.; Karuturi, S. K.; Liu, L.; Liu, J.; Li, H.; Su, L. T.; Tok, A. I. Y.; Fan, H. J., Quantum-Dot-Sensitized TiO₂ Inverse Opals for Photoelectrochemical Hydrogen Generation. *Small* 2012, 8 (1), 37-42.
4. Chuang, S.-Y.; Chen, H.-L.; Shieh, J.; Lin, C.-H.; Cheng, C.-C.; Liu, H.-W.; Yu, C.-C., Nanoscale of biomimetic moth eye structures exhibiting inverse polarization phenomena at the Brewster angle. *Nanoscale* 2010, 2 (5), 799-805.
5. Frame, F. A.; Carroll, E. C.; Larsen, D. S.; Sarahan, M.; Browning, N. D.; Osterloh, F. E., First demonstration of CdSe as a photocatalyst for hydrogen evolution from water under UV and visible light. *Chem. Commun.* 2008, (19), 2206-2208.
6. Hensel, J.; Wang, G.; Li, Y.; Zhang, J. Z., Synergistic Effect of CdSe Quantum Dot Sensitization and Nitrogen Doping of TiO₂ Nanostructures for Photoelectrochemical Solar Hydrogen Generation. *Nano Lett.* 2010, 10 (2), 478-483.
7. Holmes, M. A.; Townsend, T. K.; Osterloh, F. E., Quantum confinement controlled photocatalytic water splitting by suspended CdSe nanocrystals. *Chem. Commun.* 2012, 48 (3), 371-373.
8. Jang, J.-H.; Jhaveri, S. J.; Rasin, B.; Koh, C.; Ober, C. K.; Thomas, E. L., Three-dimensionally-patterned submicrometer-scale hydrogel/air networks that offer a new platform for biomedical applications. *Nano Lett.* 2008, 8 (5), 1456-1460.
9. Jang, J.-H.; Ullal, C. K.; Maldovan, M.; Gorishnyy, T.; Kooi, S.; Koh, C.; Thomas, E. L., 3D micro- and nanostructures via interference lithography. *Adv. Funct. Mater.* 2007, 17 (16), 3027-3041.
10. Karuturi, S. K.; Luo, J.; Cheng, C.; Liu, L.; Su, L. T.; Tok, A. I. Y.; Fan, H. J., A Novel Photoanode with Three-Dimensionally, Hierarchically Ordered Nanobushes for Highly Efficient Photoelectrochemical Cells. *Adv. Mater.* 2012, 24 (30), 4157-4162.
11. Khan, S. U. M.; Al-Shahry, M.; Ingler, W. B., Efficient photochemical water splitting by a chemically modified n-TiO₂. *Science* 2002, 297 (5590), 2243-2245.
12. Kim, K.; Kim, M.-J.; Kim, S.-I.; Jang, J.-H., Towards Visible Light Hydrogen Generation: Quantum Dot-Sensitization via Efficient Light Harvesting of Hybrid-TiO₂. *Scientific Reports* 2013, 3.
13. Kim, K.; Thiagarajan, P.; Ahn, H.-J.; Kim, S.-I.; Jang, J.-H., Optimization for visible light photocatalytic water splitting: gold-coated and surface-textured TiO₂ inverse opal nano-networks.

- Nanoscale 2013, 5 (14), 6254-6260.
14. Li, Y.; Yoo, K.; Lee, D.-K.; Kim, J. Y.; Kim, H.; Kim, B.; Ko, M. J., Photovoltaic properties of high efficiency plastic dye-sensitized solar cells employing interparticle binding agent "nanoglue". *Nanoscale* 2013, 5 (11), 4711-4719.
 15. Lin, Y.; Zhou, S.; Liu, X.; Sheehan, S.; Wang, D., TiO₂/TiSi₂ Heterostructures for High-Efficiency Photoelectrochemical H₂O Splitting. *J. Am. Chem. Soc.* 2009, 131 (8), 2772-+.
 16. Liu, L.; Wang, G.; Li, Y.; Li, Y.; Zhang, J. Z., CdSe quantum dot-sensitized Au/TiO₂ hybrid mesoporous films and their enhanced photoelectrochemical performance. *Nano Research* 2011, 4 (3), 249-258.
 17. Maeda, K.; Domen, K., New non-oxide photocatalysts designed for overall water splitting under visible light. *J. Phys. Chem. C* 2007, 111 (22), 7851-7861.
 18. Maeda, K.; Xiong, A.; Yoshinaga, T.; Ikeda, T.; Sakamoto, N.; Hisatomi, T.; Takashima, M.; Lu, D.; Kanehara, M.; Setoyama, T.; Teranishi, T.; Domen, K., Photocatalytic Overall Water Splitting Promoted by Two Different Cocatalysts for Hydrogen and Oxygen Evolution under Visible Light. *Angew. Chem. Int. Ed.* 2010, 49 (24), 4096-4099.
 19. Rodenas, P.; Song, T.; Sudhagar, P.; Marzari, G.; Han, H.; Badia-Bou, L.; Gimenez, S.; Fabregat-Santiago, F.; Mora-Sero, I.; Bisquert, J.; Paik, U.; Kang, Y. S., Quantum Dot Based Heterostructures for Unassisted Photoelectrochemical Hydrogen Generation. *Advanced Energy Materials* 2013, 3 (2), 176-182.
 20. Thiyagarajan, P.; Ahn, H.-J.; Lee, J.-S.; Yoon, J.-C.; Jang, J.-H., Hierarchical Metal/Semiconductor Nanostructure for Efficient Water Splitting. *Small* 2013, 9 (13), 2341-2347.
 21. Wang, G.; Wang, H.; Ling, Y.; Tang, Y.; Yang, X.; Fitzmorris, R. C.; Wang, C.; Zhang, J. Z.; Li, Y., Hydrogen-Treated TiO₂ Nanowire Arrays for Photoelectrochemical Water Splitting. *Nano Lett.* 2011, 11 (7), 3026-3033.
 22. Wang, G.; Yang, X.; Qian, F.; Zhang, J. Z.; Li, Y., Double-Sided CdS and CdSe Quantum Dot Co-Sensitized ZnO Nanowire Arrays for Photoelectrochemical Hydrogen Generation. *Nano Lett.* 2010, 10 (3), 1088-1092.
 23. Wolcott, A.; Smith, W. A.; Kuykendall, T. R.; Zhao, Y.; Zhang, J. Z., Photoelectrochemical Water Splitting Using Dense and Aligned TiO₂ Nanorod Arrays. *Small* 2009, 5 (1), 104-111.
 24. Zhang, M.; Lin, Y.; Mullen, T. J.; Lin, W.-f.; Sun, L.-D.; Yan, C.-H.; Patten, T. E.; Wang, D.; Liu, G.-y., Improving Hematite's Solar Water Splitting Efficiency by Incorporating Rare-Earth Upconversion Nanomaterials. *Journal of Physical Chemistry Letters* 2012, 3 (21), 3188-3192.
 25. Zhong, M.; Li, Y.; Yamada, I.; Delaunay, J.-J., ZnO-ZnGa₂O₄ core-shell nanowire array for stable photoelectrochemical water splitting. *Nanoscale* 2012, 4 (5), 1509-1514.

Acknowledgement

2010년 초 추운 겨울에, UNIST 방문해서 장지현 교수님을 뵙던 기억이 생생합니다. 벌써 졸업이네요. 시간은 너무나 빨리 흐릅니다. 지난 5년 6개월 간의 시간은 제 인생에 큰 획을 그었고, 인간으로써 저 자신의 성숙에 많은 의미가 있었던 시간이었습니다. 박사 학위 이외에도, 제가 보지 못하고, 생각 하지도 못했었던 많은 기회와 경험을 NCL 에서 하였습니다. 거인의 어깨에서 넓은 세상을 보라 (If I have seen further it is by standing on the shoulders of Giants). 아이작 뉴턴의 말입니다. 저에게 가너리지만 든든한 어깨를 빌려 주시고 넓은 세상을 보여주신 장지현 교수님께 감사의 말씀을 전합니다. 교수님 덕분에 저 스스로도 많이 성장 했고, 과학적 지식 외에도 인생을 살아가는 방법 또한 많이 배웠 습니다. 불철주야 아들 걱정애 잠 못 이루시고, 어떠한 어려움이 닥쳐도 남자의 자존심 으로 이겨내신 초인적인 아버지께 또한 감사와 존경을 드립니다. 아버지의 희생은 어떠한 수식어로도 묘사하기 힘듭니다. 많이 사랑 합니다. 제가 공부를 할 수 있게, 어렸을 때 불우한 환경으로부터 저를 지켜 준 형. 평소에 많이 표현을 못하지만, 역시 사랑합니 다. 저의 유일한 선배이자, 동료라고 부를 수 있는 이정수 교수님 (형). 형 덕분에 많은 연구를 진행 할 수 있었고, 서로 자극이 되어 논문도 많이 낼 수 있었습니다. 앞으로도 잘 해봅시다. 학위 과정 중에 많이 고마웠습니다. 또한 친구 같이 내가 이상한 불평 불 만 많이 하여도, 잘 참아준 NCL 홍일점 김선이. 내가 표현은 안 하지만 많이 감사하고 있다. 앞으로 남은 학위 잘 마치고 좋은 엄마, 아내, 연구자가 되길 바란다. 그리고 나의 수족처럼 나를 도와준 윤기용. 너한테는 지난 2년간 많은 신세를 지었다. 나의 부사수라 부를 수 있을 만큼 잘 따라 주고, 도와줘서 고맙다. 부디 박사 과정에 진학 해도 지금처 럼 열심히 하길 빈다. 많은 인생의 고민과, 과학적 사실에 대한 토론을 나이에 맞지 않 게 잘해주고 열심히 일해준 똑똑한 광명준. 앞으로도 꾸준히 연락 하면서, 많은 이야기 를 나누고 싶다. 내가 엄청 많이 욕을 해도, 꾸준히 옆에서 실험하는 강경남. 앞으로 너

는 많이 배우지 않으면 힘들 것 같다. 하지만, 지금처럼 발전해 나가다 보면 좋은 일 있을 거라 생각 한다. 다른 NCL 멤버들도 학위 과정 중에 열심히 하여 좋은 결과, 좋은 논문 쓰고 좋은 사람이 되었으면 합니다. 내가 힘들 때나 기쁠 때, 슬플 때 거의 반평생 넘게 함께 해준, 친구들 정말 고맙다. 창우는 지금은 별로 일이 안 풀리지만, 앞으로 잘 될 것이니 포기 말고 열심히 살기를 바란다. 우영이는 이제 결혼 했으니, 예쁜 자식을 놓고 유진씨랑 행복하게 잘 살자. 평소에 너의 그 넉넉함과 꼼꼼함, 친절함 성격에 많이 의지 하고 있다. 성진이는 좋은 여자 만나서, 결혼 하고 행복했으면 좋겠다. 형이 좋아하는 거 알지. 너의 똑똑함과 센스에 간간히 놀라고 있다. 장점 잘 살려서 잘 살았으면 좋겠다. 향호는 앞으로 좋은 연기가 되고, 바라는 바 잘 되길 빈다. 내가 힘겨운 일이 있을 때, 잘 들어주고 좋은 조언 해줘서 고맙다. 예술과 인생에 대해서 논 할 수 있는 친구가 있다는 건 참 좋은 일이다. 재태는 내가 학위 과정 중에 외롭지 않게, 힘든 일이 있었을 때 잘 들어주고 잘 이해줘서 정말 고마워 한다. 너는 뭐든 잘할 성격이니 술 만 조금 줄이면 좋겠다. 호제는 요새 자주 보지는 못하지만 다점이 잘 키우고 혜지랑 행복하게 잘 살아라. 브라질에 있는 홍립이, 일 하느라 술 먹으라 일하라 힘든 종훈이, 학교에서 애들 가르치는 오현이, 애 키우고 열심히 일하는 가장 우용이, 이제 막 결혼해서 행복한 현영이, 우리 우담 회원들 행복하고 건강하게 잘 지내자. 마지막으로 UNIST 에서 만난 소중한 인연들, 상하, 재환, 용식, 수용아, 연란이 평생 함께 보고 싶다. 연락 자주 하자~. 또한 함께 506 호 오피스를 썼던, 신호, 형민이 형, 가은이, 동우, 승민이 형, 아영이, 은용이 형, 필재, 유리, 병만이 형. 앞으로 좋은 일, 행복한 일만 가득 하길 기원합니다. 이외에도 저를 아시는 모든 분들께 감사의 말씀 드립니다. 다들 행복 하십시오. 우리는 그렇게 살려고 태어난 거니까요.

2015년 7월, 애증의 오피스

에서 안효진

드림

■ Publication list

1. Ahn, H.-J.; Kwak, M.-J.; Lee, J.-S.; Yoon, K.-Y.; Jang, J.-H., “Nanoporous hematite structures to overcome short diffusion lengths in water splitting.”, *J. Mater. Chem. A*, 2014, 2 (47), 19999-20003

2. Ahn, H.-J.; Kim, M.-J.; Kim, K.; Kwak, M.-J.; Jang, J.-H., “Optimization of Quantum Dot-Sensitized Photoelectrode for Realization of Visible Light Hydrogen Generation.”, *Small*, 2014, 10 (12), 2325-2330

- Selected as a Back Cover Paper.



3. Ahn, H.-J.; Kim, I.-H.; Yoon, J.-C.; Kim, S.-I.; Jang, J.-H., “p-Doped three-dimensional graphene nano-networks superior to platinum as a counter electrode for dye-sensitized solar cells.”, *Chem. Comm.*, 2014, 50 (19), 2412-2415

- Selected as a Back Cover Paper.



4. Thiyagarajan, P.*; Ahn, H.-J.* ; Lee, J.-S.; Yoon, J.-C.; Jang, J.-H., “Hierarchical Metal/Semiconductor Nanostructure for Efficient Water Splitting”, *Small*, 2013, 9 (13), 2341-2347.

- Selected as an Inside Cover Paper

- *These authors contributed equally to this work.



5. Ahn, H.-J.; Thiyagarajan, P.; Jia, L.; Kim, S.-I.; Yoon, J.-C.; Thomas, E. L.; Jang, J.-H., “An optimal substrate design for SERS: dual-scale diamond-shaped gold nano-structures fabricated via interference lithography.”, *Nanoscale*, 2013, 5 (5), 1836-1842

6. Ahn, H.-J.; Kim, S.-I.; Yoon, J.-C.; Lee, J.-S.; Jang, J.-H., “Power conversion efficiency enhancement based on the bio-inspired hierarchical antireflection layer in dye sensitized solar cells.”, *Nanoscale*, 2012, 4 (15), 4464-4469

7. Ki-Yong Yoon.; Ahn, H.-J.; Myung-Jun Kwak.; Thiyagarajan, P.; Jang, J.-h., “Graphene Quantum Dot-Protected Cadmium Selenide Quantum Dot- Sensitized Photoanode for Efficient Photoelectrochemical Cells with Enhanced Stability and Performance”, *Adv. Opt. Mater.*, 2015, DOI: 10.1002/adom.201500066

8. Hwang, S.-H.; Ahn, H.-J.; Yoon, J.-C.; Jang, J.-H.; Park, Y.-B., “Transparent graphene films with a tunable piezoresistive response.”, *J. Mater. Chem. C*, 2013, 1 (43), 7208-7214

9. Lee, J.-S.; Ahn, H.-J.; Yoon, J.-C.; Jang, J.-H., “Three-dimensional nano-foam of few-layer graphene grown by CVD for DSSC.”, *Phys. Chem. Chem. Phys.* 2012, 14 (22), 7938-7943

- Selected as a Cover Paper.



10. Kim, K.; Thiyagarajan, P.; Ahn, H.-J.; Kim, S.-I.; Jang, J.-H., “Optimization for visible light photocatalytic water splitting: gold-coated and surface-textured TiO₂ inverse opal nano-networks.”, *Nanoscale*, 2013, 5 (14), 6254-6260

11. Kim, S.-I.; Lee, J.-S.; **Ahn, H.-J.**; Song, H.-K.; Jang, J.-H., “Facile Route to an Efficient NiO Supercapacitor with a Three-Dimensional Nanonetwork Morphology.”, *ACS Appl. Mater. Interfaces*, 2013, 5 (5), 1596-1603

■ **Patents**

1. “A structural Approach to the Highly Efficient Water Splitting in the Visible Range” Korea Patent No. 10-1376835.
2. “Power Conversion Efficiency Enhancement Based on the Bio-inspired Hierarchical Antireflection Layer in Dye Sensitized Solar Cell” Korea Patent No. 10-1338785.